AlbaEXP_PROJ_DOC_01.dotx

EXPERIMENTS DIVISION

º	*Project*	*Created*	*Printed*	*Pages*	*Revision*
001		2019-08-09		84	1.1
	XAIRA_ES_CDR_20191129_v1-web				

XAIRA End Station:
Conceptual Design Report

Prepared by	*Checked by*	*Approved by*
Damià Garriga Nahikari González	Judith Juanhuix	

Distribution list

XAIRA board, Alfresco, team managers, ES CDR Panel Members

Co-funded by:

Document Change log

Author	Change Description	Date	Version
D Garriga	First version	06/11/2019	1.0
D Garriga	Corrections as requested by CDR panel	28/11/2019	1.1

This Concept Design Report (CDR) describes the most relevant features of the XAIRA End Station, the basic concepts guiding its design, the features of the instruments, and how the crucial technical challenges are going to be solved.

Disclaimer: References on brands and commercially available equipment appearing along the text are solely used as an example to highlight the feasibility of the project. They do not imply the absence of alternative solutions from other companies.

Contents

1 Scientific case for XAIRA

The scientific case for XAIRA includes three aims:

1) **Microcrystallography applications**, by providing a highly stable full beam with a size of 3×1 μm^2 FWHM (h×v) and a flux of >$3 \cdot 10^{12}$ ph/s (at 250 mA in storage ring) at 1 Å wavelength (12.4 keV). The beam size at sample should be adjustable to the users' needs, with larger sizes possible at least up to 10 × 10 μm^2 and smaller sizes down to 1×1 μm^2.

2) **Native phasing experiments** at long wavelengths, by extending the low energy limit down to 4 keV. This builds on the fact that the anomalous signal of naturally-occurring metals in proteins is enhanced in the case of small crystals [1].

3) **Serial crystallography techniques**, by offering a higher flux over $3 \cdot 10^{13}$ ph/s at the expense of energy bandwidth and at a limited energy range, around 10 keV.

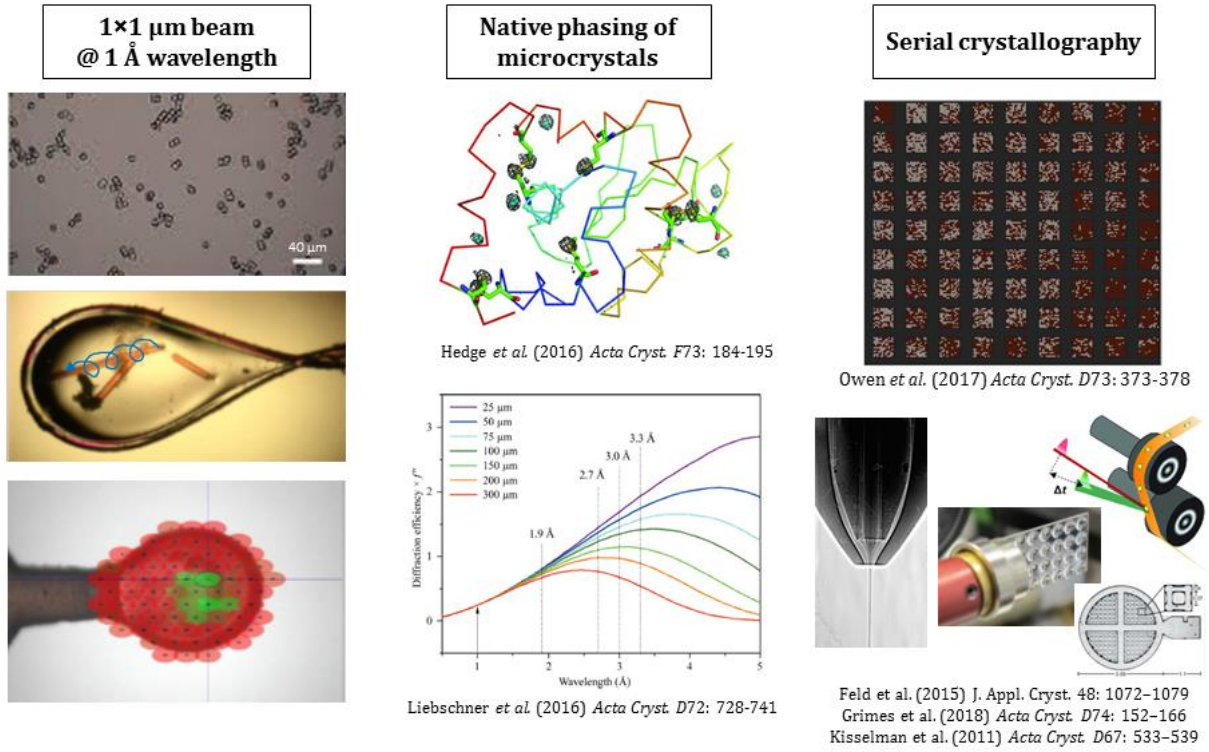

Figure 1. Scientific cases to be covered by XAIRA beamline. Graphical summary of microcrystallography experiments (left column); native phasing (middle); and serial crystallography (right).

2 XAIRA End Station objectives

We aim to design an End Station (ES) for XAIRA beamline for macromolecule crystallography with the following features:

- The instrument operates at photon energies in the range 4.0 – 14 keV, achieving data collection at least at 1Å resolution with 12.4 keV photon energy. The range 3.0 - 4.0 keV may also be achieved, provided the overall performance and operation of the beamline is not compromised.

- The instrument is compatible with beam sizes ranging for 1 × 1 μm^2 to, approximately, 10 × 10 μm^2.

- The instrument allows experiments to be performed either in air or in helium atmosphere.

- The instrument allows to measure samples at both at room temperature or cryogenic conditions, for both air and helium atmospheres.

- The instrument allows for "traditional" data collection on large crystals by combined translations and rotations to collect diffraction data from a same crystal at different positions and in different orientations (including helical scans).

- The instrument allows for ≥500 Hz serial scanning data collection on samples consisting of a large number of small crystals (< 5 μm) positioned in regular or irregular pattern on a chip or array.

- The instrument is equipped with an automated sample changer, with sample exchange time shorter than 20 s and dewar capacity for ≥400 samples.

- The instrument is modular to allow upgrades and changes in the sample environment setup, in particular leaving significant free space around sample position to allow non-fixed target/time-resolved SSX experiments and the implementation of X-ray emission spectroscopy.

3 X-ray beam parameters

The values of beam parameters at and around sample position are taken into account for the instrument design. The XAIRA beamline project objectives specify a full beam size at sample of 3×1 μm^2, and photon energies for operation including at least the range 4.0 – 14.0 keV.

The XAIRA beamline can be operated in monochromatic mode, by using a Si(111) crystal channel cut monochromator ($\Delta E/E$ ~$2 \cdot 10^{-4}$ within the whole energy range), or in pink-beam mode, when using the Mo/B_4C multilayer monochromator (for the ~6-13 keV range) for an energy bandpass of ~1% that includes the flux of an entire undulator harmonic.

At sample position, it is predicted that the X-ray beam will be focused down to 3 × 1 μm^2 (H × V) FWHM in the whole 4-14 keV energy range. Further modifications of beam size will also be possible through diverse strategies, covering the range between 1 × 1 μm^2 to 15 × 10 μm^2 (see section 5.9).

The operation of the dual-mode monochromator induces a beam excursion along the vertical direction; that is, an offset between the position of the beam at 4 keV and at 14 keV. This maximum offset is of 1100 µm between the monochromator and the VFM mirror, and downstream the mirror it is reduced gradually by the focusing effect until reaching ~60 µm at sample position.

Photon flux at sample position remains over $3 \cdot 10^{12}$ ph/s in the useful energy range (with 250 mA in storage ring), possibly reaching 10^{13} ph/s when using the multilayer monochromator. XAIRA undulator is designed so that, at minimum gap (4.8 mm), the 3rd harmonic falls at 4 keV and the 9th harmonic at 12 keV, to maximize flux at these energies.

Summary of beam parameters at sample position:

Beam size at 12.661 keV (FWHM, H × V)			μm^2	3.1 × 0.7
Beam divergence at 12.661 keV (FWHM, H × V)			mrad	2.6-3×~0.6
Total flux at 12.661@250 mA, Si (111)			ph/s	$3.5 \cdot 10^{12}$
Total flux at sample, whole energy range @250 mA, Si(111)			ph/s	$3\text{-}20 \cdot 10^{12}$
Energy resolution	Si (111)	(4-14 keV)		$2 \cdot 10^{-4}$
	Multilayer Mo/B_4C	(> 6-13 keV)		$1 \cdot 10^{-2}$

4 Foreseen sizes for sample and sample supports

XAIRA is a microfocus beamline, specially designed to obtain diffraction data from **microcrystals**, that is, crystals with sizes in the range of 0.5 × 0.5 × 0.5 μm^3 to 20 × 20 ×20 μm^3. The small beam will also be useful to characterise "**standard**" **crystals** with sides up to ~500 μm, especially in the case of twinned or mosaic crystals. Micron-sized beams are especially useful to analyse other crystal shapes such as **needles and plates**, in which one or two sides of the crystal can be <10 μm while the other(s) can be much larger (typically 100 - 600 μm).

Compared to larger crystals, which traditionally are always mounted on nylon loops to present them to the X-ray beam, a myriad of sample supports and delivery strategies have been developed to present microcrystals to the beam (as reviewed in [2] and summarised in Figure 2).

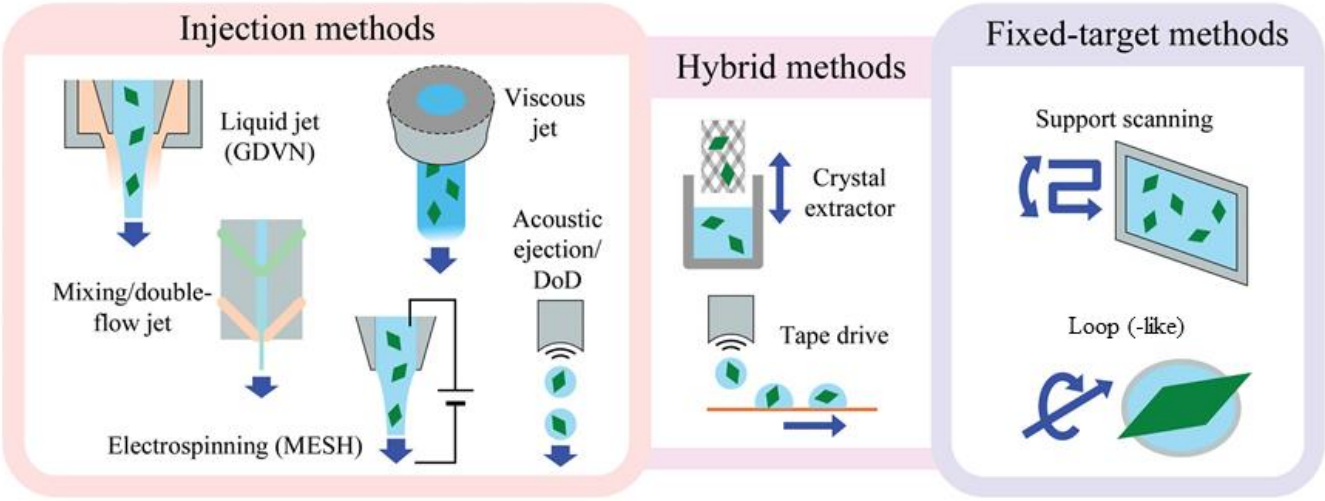

Figure 2. Sample delivery methods for microcrystal MX experiments. Adapted from Martiel et al 2019, *Acta Cryst. D* 75: 160–177.

XAIRA End Station is designed to be compatible with fixed-target methods, both for "pin-based" sample holders (where the sample support is mounted on a standard magnetic base compatible with goniometer heads from most MX beamlines) and for larger chips dedicated to SX. This allows catering for the most extended and well-stablished data collection strategies, including those based in sample oscillation, as well as raster scans.

Although other sample delivery methods are not included in the current design, the ES has to be flexible enough to allow for their future implementation. To this end, sample environment elements can be retracted or easily unmounted as to leave some room for installation of other potential instruments (e.g. jet injectors, conveyor belts, …).

Regarding "pin-based" supports, several types of sample holders can be expected, including:

- **Loops**; typically circling an area with diameters between 20 μm and 1.5 mm.
- **Capillaries**; typically with outer diameters from 0.1 mm to 1 mm and useful lengths (i.e. regions loaded with sample) of 2-3 mm.
- **Meshes**; with most common diameters of 400 to 700 μm and mesh openings of 10 to 50 μm.

- **Microchips**; of various formats, typically limited to active areas of 2 × 2 mm² to 5 × 5 mm².

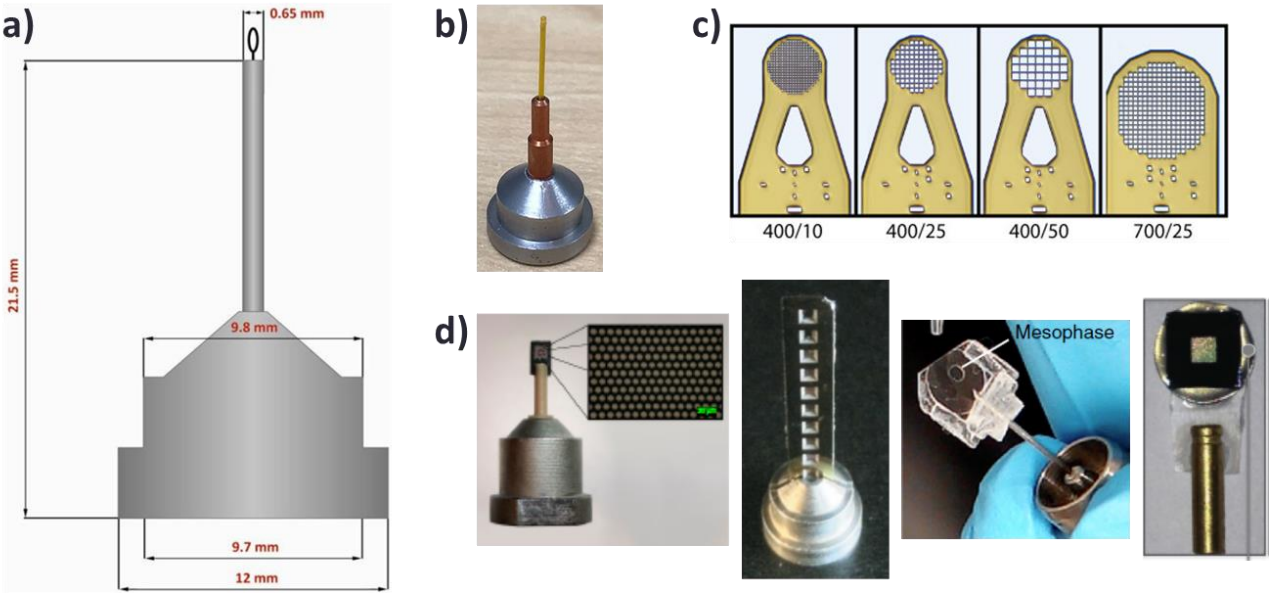

Figure 3. Expected sample supports mounted on goniometer-compatible bases. a) Scheme of a standard SSRL-style pin base with a nylon loop mounted on a stainless steel tube (from Hampton Research catalogue); **b)** Polyimide tubing capillary inserted into a standard base; **c)** Various commercial designs of kapton mesh for harvesting of microcrystals (from MiTeGen catalogue); **d)** Examples of pin-based supports for SSX: roadrunner chip; photoresist chip; IMISX glass slide sandwich; Si_3N_4 wafer sandwich.

In the last decade, larger chip formats have been designed for fixed-target serial crystallography (SX) at X-FELs and synchrotrons. These are increasingly used in microcrystallography beamlines, in particular for room temperature data collection, but require adapted stages (such as the one described in [3]) as the chips are too large to be held on goniometer-compatible bases.

Table 1 shows a non-exhaustive list of chips for fixed target SX reported in the literature in the recent years, to illustrate the kind of chips that might be used in XAIRA:

Table 1. Examples of chips developed in the last 5 years as fixed-target supports for serial crystallography

Chip	Patterned?	Pin-based?	Commercially available?	Area to scan	Reference
Roadrunner I	Yes	Yes	Yes (suna-precision)	1.5 × 1.5 mm^2	Roedig et al. 2015 [4]
Mylar multicrystal holder	No	Yes	No	1.5 × 1.5 mm^2	Barnes et al. 2019 [5]
Si_3N_4 wafer sandwich	No	Yes	Commercial parts	2.5 × 2.5 mm^2	Coquelle et al. 2015[6]
IMISX chip (for LCP bolus)	No	Yes	Yes (MiTeGen)	5 × 5 mm^2	Huang et al. 2015 [7]
Polycarbonate high density sample mounting grid	No	Yes	No	2.5 × 12 mm^2	Cohen et al. 2014 [8]
Microfluidic trap array	Yes	Yes	No	5 × 15 mm^2	Lyubimov et al. 2015 [9]
Photoresist stripe-based chip	Yes	Yes	No	5 × 30 mm^2	Murray et al. 2015 [10]
Monocrystalline quartz chip	Yes	Yes	No	20 mm ∅	Ren et al. 2018 [11]
Tapered holes array	Yes	No	No	20 × 20 mm^2	Mueller et al. 2015 [12]
Nylon mesh	Yes	No	Commercial parts	20 × 20 mm^2	Lee et al. 2019 [13]
Low-Z plastic wafers	Yes	No	No	25 × 12 mm^2	Feld et al. 2015 [14]
Bottomless apertures array	Yes	No	No	28 × 28 mm^2	Oghbaey et al. 2016 [15]
Sheet-on-sheet approach	No	No	No	30 × 30 mm^2	Doak et al. 2018 [16]
Roadrunner II	Yes	No	No	32 × 12 mm^2	Lieske et al. 2019 [17]
ChipX3	No	No	No	40 x 20 mm^2	Wijn et al. 2019 [18]

5 Key operational processes and systems

The concepts judged to be most relevant from the perspective of both the users of XAIRA beamline and the productivity of the beamline are summarized in this section. The ES is designed to be dedicated fully to protein crystallography. However, experiments related to other scientific areas can be performed, provided that technical aspects such as sample mounting, sample environment and diffraction data collection geometry are compatible with the XAIRA ES capabilities.

5.1 Efficiency, automation and user friendliness

XAIRA beamline is designed to maximise its productivity and ensure an efficient use of the beamtime. To this aim, the beamline will feature key systems such as an automated sample changer, a highly performing on-axis sample visualisation system to assist centring procedures and a fast detector, along with a high flux (especially with the use of the multilayer monochromator) and automated fast data quality assessment pipelines.

On the other hand, to minimise downtime during operation, the beamline will be equipped with cutting edge mechanics with innovative approaches (e.g. nanobender, dual monochromator) that improve its stability and reliability. A large sample storage dewar and the implementation of fast protocols for beam alignment will also contribute to minimise staff intervention and waste of beamtime.

From the user point of view, the beamline usage will be kept as similar as possible to that of XALOC, both in terms of procedures (sample loading/unloading, sample alignment, data collection GUIs…) and of software (data quality assessment, processing pipelines, data management, …).

5.2 Envisaged data collection modes and required sample motions

XAIRA beamline is designed to be compatible with most data collection strategies used in macromolecular crystallography experiments, including some of the newly developed ones for SSX.

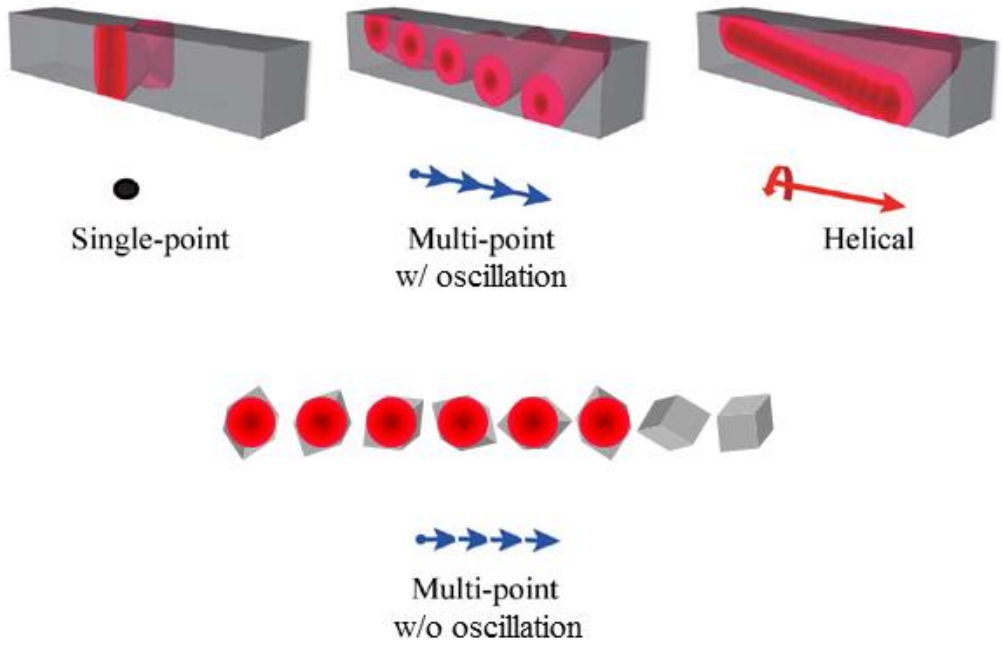

Figure 4. Data collection strategies with a microfocus beam. Schematic drawing of data-collection strategies from a single crystal (top row) or multiple crystals (bottom row) using a microbeam. Adapted from Yamamoto et al. (2017), *IUCrJ*. 4:529–539.

The table below summarises the data collection modes that are envisaged at XAIRA, together with their requirements in terms of sample and beam operation.

	Sample oscillation	**Sample translation**	**Energy requirements**
Characterise crystal (fast, attenuated)	yes	-	-
Grid scan (sample mapping)	-	yes (gonio stages)	-
Oscillation data collection	yes	-	-
Helical data collection	yes	yes	-
Native phasing / SAD phasing	yes	-	yes

Multiwavelength Anomalous Diffraction (MAD phasing)	yes	-	yes
Multiple partial data sets from pre-localised μxtals (Mesh & Collect)	yes	yes	-
Multiple partial data sets from non-mapped samples (SS-ROX)	yes	yes	-
Multiple single frames from fast rastering on chip/grid/loop (Fixed-target SSX)	-	yes (SSX stages)	-
Elemental fluorescence analysis	-	-	yes
Energy scan (fluorescence)	-	-	yes

Table 2. Envisaged experiments to be performed at XAIRA beamline.

5.3 Sample visualization and localisation

One of the challenges faced by microcrystallography beamlines is the establishment of strategies to effectively visualise and characterise the samples, which, by definition, can have sizes in the micron range. Defining the crystal(s) position in the sample holder support (*sample mapping*) is particularly relevant to ensure a proper alignment of the sample to the beam (which will also have a size in the micrometre range).

To this end, a combination of an optical visualisation system and X-ray-based raster scans will be used in XAIRA. A third complementary strategy, based on phase contrast imaging of the sample, is also considered as an upgrade.

For serial crystallography experiments, the use of patterned chips in which crystals occupy predefined positions is also foreseen. In this scenario, the requirements on sample visualisation would be more relaxed, provided the chip position is fiducialised and the positions potentially occupied by the crystals can be aligned to the beam with sufficient precision.

On-axis visualisation system

The proposed OAV is based on an on-axis microscope located upstream of the sample, allowing to visualize it in the same direction as the incoming X-ray beam. The resolution at the highest magnification and the field of view at lowest magnification are specified to be better than 1.0 μm and at least 2.0 × 2.0 mm, respectively. A large working distance for the microscope objective and a high frame readout rate for the camera are also desirable.

Diffraction raster scans

These are based on rastering of the sample with the micron-sized X-ray beam while recording a diffraction signal from each area, a technique available in most of the current MX beamlines.

Automation of these exploratory scans opens the door to automatise the full data collection process, from sample mounting to data analysis.

The beam size defines the raster-scan resolution, which can be of 1.0 μm for XAIRA, but at the same time a small beam size limits the speed at which a given area can be scanned (scanning a 2 × 2 mm^2 area with a 1 × 1 μm^2 beam @ 500 Hz would take over 130 minutes). Thus, this technique will mainly be used to scan smaller areas (even if using a larger beam).

Phase contrast imaging

Phase-contrast X-ray imaging is used in some MX beamlines (e.g. P14 beamline at PETRA III, I04 beamline at Diamond Light Source) for full-field visualization of the crystals on a sample holder. Spatial resolutions obtained are as low as 0.6 μm. Phase-contrast imaging is especially useful when the bolus is opaque to light and the sample can't be located using the OAV system [19]–[21].

An additional advantage of X-ray imaging technique is that it involves almost negligible radiation doses on the sample (~100 Gy), especially when compared to X-ray raster scans (in the order of ~1 MGy).

The phase contrast instrumentation requires additional elements in the optics system, since the beam needs to be defocused at the sample position to illuminate the whole area of interest (around 1 × 1 mm^2). Ideally this additional optics should be placed in the beam path without having to adjust the optical elements required for the experiments. Two methods fulfilling this condition are described in section 9.1.

Note that this method is <u>not proposed</u> to be implemented during construction phase of the project. However, the beamline design should envisage its implementation.

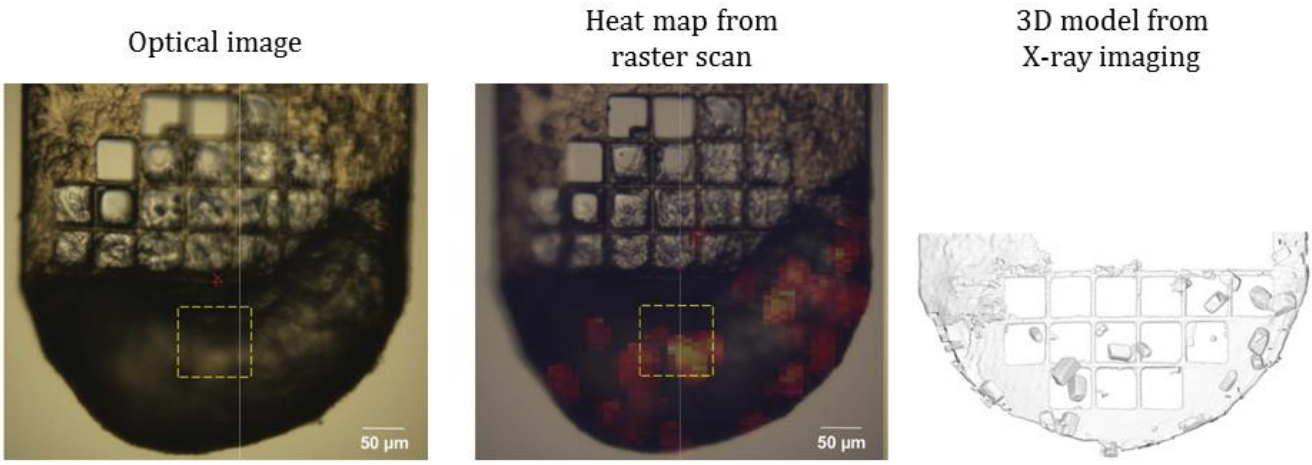

Figure 5. Different strategies for visualization of microcrystals. Crystals embedded in an LCP matrix and mounted on a MiteGen mesh, as characterized by optical imaging (left), raster scanning (centre) and X-ray imaging (right). Adapted from Polikarpov et al. (2019), *Acta Cryst D*75: 947–958

5.4 Atmosphere around beam path

The presence of air at the beam path along the sample environment, i.e. between the end of the vacuum sectors and the detector, affects the quality of the collected data in two ways: reduces the incoming flux to the sample and increases the background noise on the detector.

Absorption

The absorption of the beam due to interaction with air significantly reduces the photon flux on the sample, especially in the 3-6 keV energy range (Figure 6 and Table 3). This affects both the incident beam and the diffracted photons, thus reducing the intensity of the signal that will be recorded by the detector. This effect will be especially critical when data is collected for native phasing experiments.

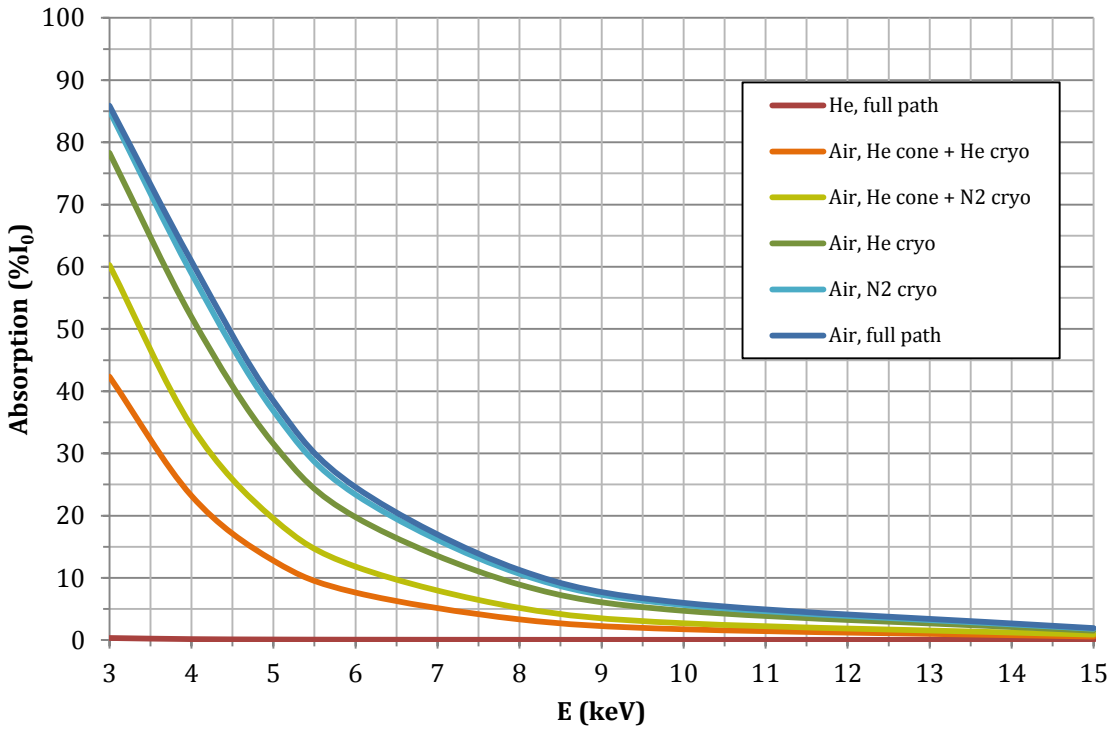

Figure 6. Absorption at different beam energies, for a direct beam reaching travelling from the diamond window to the surface of the detector (at its centre), considering several scenarios with different defined atmospheres along the beam path. Calculations considered vacuum-to-sample distance of 30 mm, sample-to-detector distance of 70 mm, helium cone depth of 50 mm and cryostream flow width of 22 mm. For Helium cone calculations, the Kapton film thickness of the XALOC cone was considered (2 mm).

	uncontrolled	cryo only		He cone		He chamber
Energy	I/Io Air only	I/Io Air + N_2 cryo	I/Io Air + He cryo	I/Io cone + N_2 cryo	I/Io cone + He cryo	I/Io He only
(keV)	%	%	%	%	%	%
3	14.1	14.9	21.7	33.9	49.2	99.7
4	39.1	41.1	48.1	61.3	71.8	99.8
5	61.6	63.2	68.5	77.8	84.3	99.9
6	75.4	76.6	80.2	86.5	90.5	99.9
8	88.7	89.3	91.1	94.0	95.9	100.0
10	94.0	94.4	95.3	96.9	97.8	100.0
15	98.1	98.2	98.5	99.0	99.3	100.0

Table 3. Transmission of the incoming beam with the different beamline configurations. Numbers indicate percentage of the incoming beam I_0 transmitted from the vacuum window to the detector plane.

Scattering

The quality of the collected data is also limited by background noise, mostly originated by X-ray scattering from extraneous items, such as the crystal mount and the atmosphere in the path of the beam. The scattered photons add to the total count in each pixel, thereby increasing the error but not the signal [22],[23]. The optimization of the crystal mount is independent of the conceptual design of the end-station and is out of the scope of this report. Here we focus therefore on the optimization of the composition of the atmosphere in the path of the beam.

The background on the detector due to X-rays interacting with atmosphere mainly arises from the path between the collimator and the beamstop, where the scattered photons from the full beam cannot be shadowed nor stopped by the end-station elements. Out of the different interactions the X-ray beam can have, the main contributors to the background noise are the Compton (inelastic) scattering and the Thompson (elastic) scattering, the relative influence depending on the photon energy and the element and density of the atmosphere. The probability of X-rays interacting with a single atom is quantified by the cross section value. Figure 7 shows the cross section data for air and He in the working energy range.

Photoelectron absorption, which results in the reduction of flux, is largely dominating in air, especially at low energies. As shown above, the use of a He atmosphere solves this issue, which can have a serious impact especially at low energies.

The inelastic scattering cross section of He and air are very similar in the whole energy range, whereas the elastic cross section of air is ~4 times higher than that of He. In this respect, air and He interact similarly with matter. However, the final amount of X-rays elastically and inelastically scattered which contribute to the diffuse scattering will also depend on the *density* of the atmosphere. And in normal pressure and temperature conditions (NTP, 20ºC and 1 atm), He is ~7.20 times less dense than air, so therefore produces less scattering. This

effect has been quantified for Compton scattered photons contributing to noise at different shells of the detector for air and He atmosphere (Figure 8).

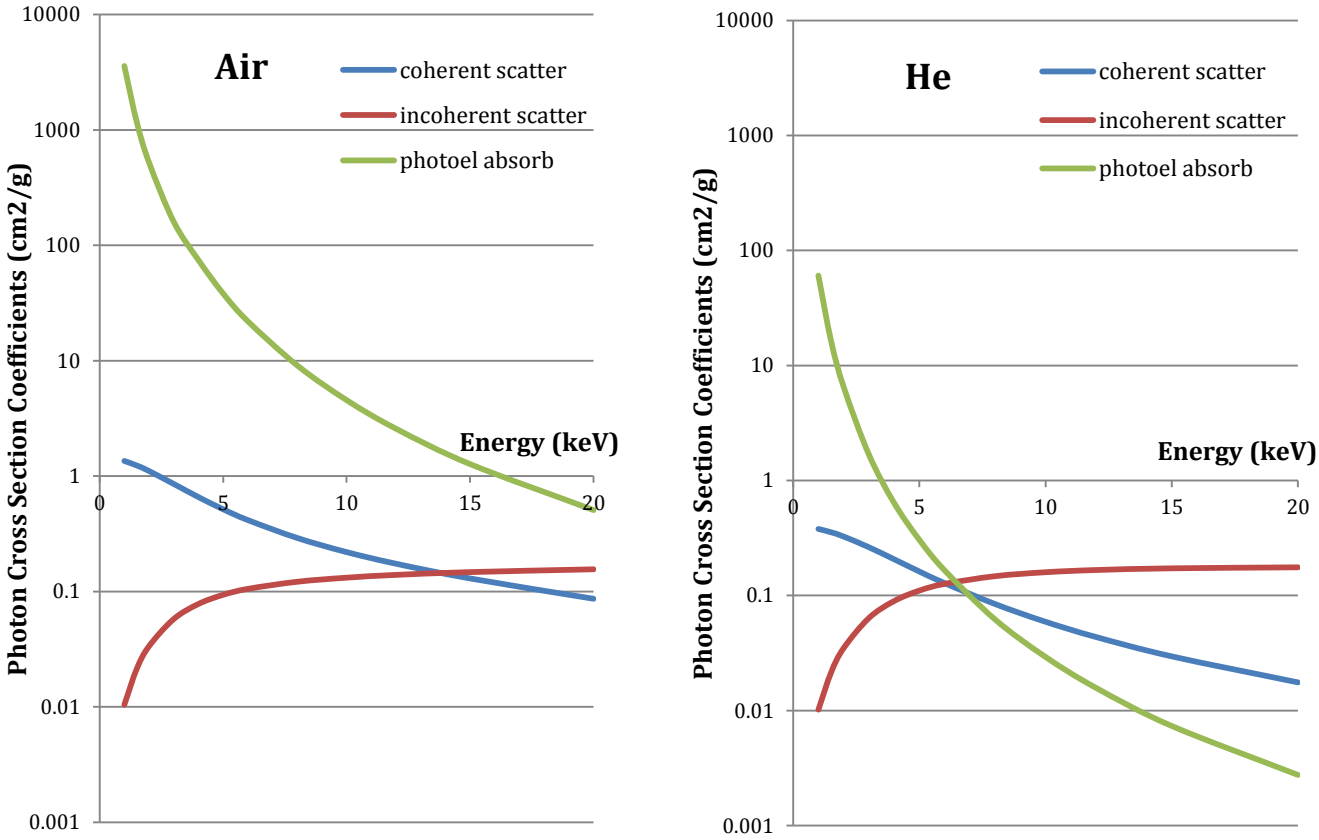

Figure 7. Photon cross-sections of the different interaction channels for helium (left) and air (right) at the XAIRA energy range. Cross-sections quantify the probability of interaction between X-rays and matter for a given interaction. Calculated from NIST X-COM database.

The reduction of background by using He atmosphere has been experimentally proved even at standard photon energies for MX: Spring-8 BL32XU beamline reports that the use of their helium chamber reduces background noise from air scattering by a factor of 10 at 12.4 keV [24]. Similar results have been reported at Photon Factory BL1A beamline [25].

Another report quantified the reduction of air scattering at the different resolution shells to produce a 6-fold to 2-fold signal-to-noise improvement, from lower to higher resolution shells respectively, *just with the use of a Helium-gas cryostream*, without any further action on the environment of the rest of the beam path [23](Figure 9).

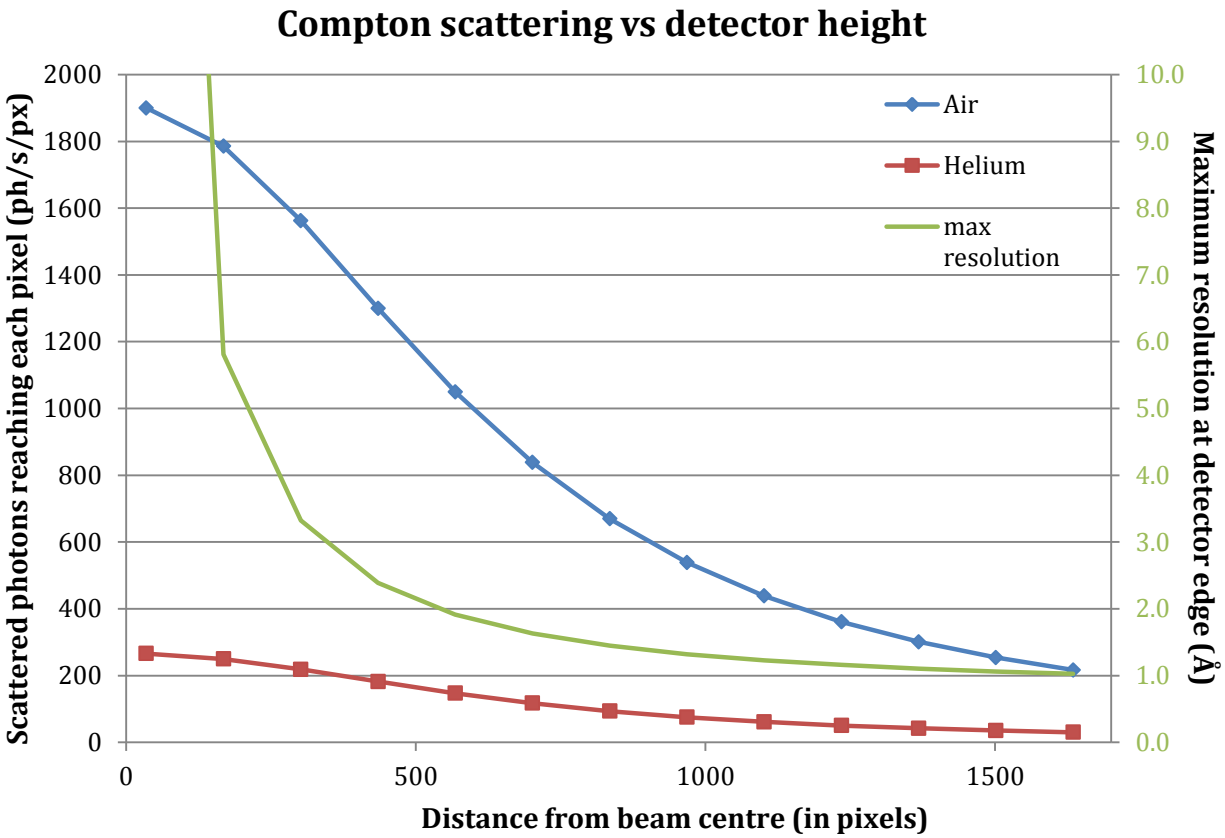

Figure 8. Compton (inelastic) scattering from a 12 keV X-ray beam interacting with air (blue line) or with helium gas (red line). For these calculations, the XAIRA ES geometry was considered: the beampath exposed to environment (collimator-to-beamstop distance) of 40 mm, sample-to-detector distance of 70 mm, detector half-height of 115 mm and a flux of 10^{13} ph/s.

The reduction of background produced by the environment atmosphere is especially relevant in microfocus beamlines, which are typically collecting data from microcrystals. These are usually mounted in small holders, whose contribution in the background noise is smaller than standard mounts. In addition, due to the weaker signals of diffraction experiments with microcrystals, the reduction of the diffuse background scattering has a significant impact on the final data quality [26]. Also, the minimisation of background reduces the dose required for the pursued signal-to-noise ratio and, thus, effectively contributes to mitigation of radiation damage effects.

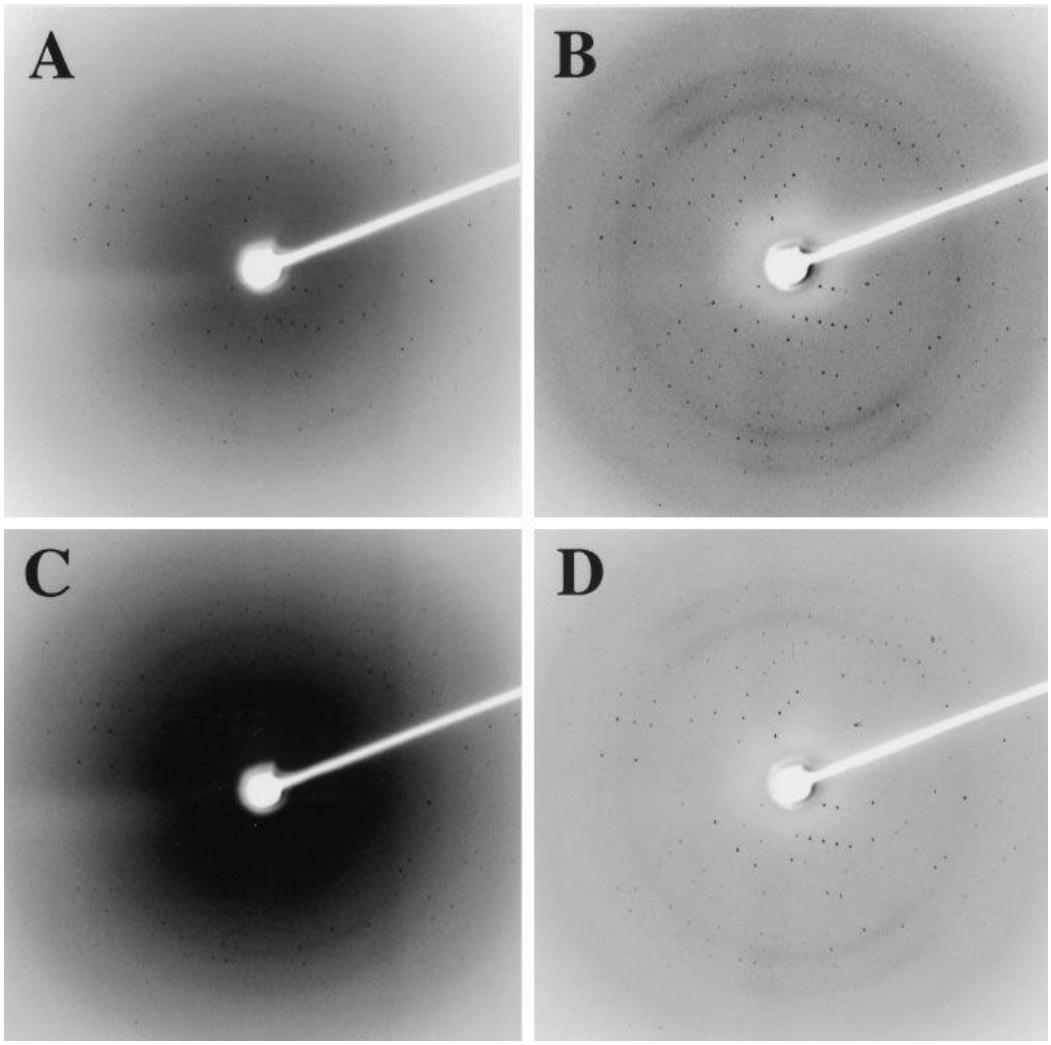

Figure 9. Reduction in background scattering achieved by using cold helium gas cryostream rather than cold nitrogen gas to maintain a frozen protein crystal at a temperature of 170 K. Diffraction patterns were recorded under otherwise identical conditions of x-ray beam intensity and exposure time, on an R-axis IV protein diffraction camera with a focused, 300 μm x-ray spot at 11 keV. The best possible representations of the two diffraction patterns are shown for N2 (A) and for He (B). A more accurate representation of the improvement provided by He is given by showing the images with identical gray scale and threshold values, in (C) for N2 and in (D) for He. From Glaeser et al. (2000), *Biophys. J.* 78(6): 3178–3185.

The Helium chamber

To achieve the minimum background and maximum counts on the detector, the whole beamline would be set in vacuum. This would not only allow the collection of data with the lowest background, but also has some additional advantages in sample visualisation, as it allows the use of electron microscope technology for sample imaging, as recently implemented in VMXm at Diamond [27]. On the other hand, however, other operations such as sample mounting and, in particular, maintenance of sample cryocooling conditions during data collection, become highly complicated. Due to such technical constraints, together with resource restrictions, this option is not considered for XAIRA.

Thus signal preservation strategy in XAIRA will be based in the establishment of a helium atmosphere at the beam path in the End Station. There are two general solutions for this: the use of a helium cone -leaving some parts of the beam path in air-, or the installation of a

helium chamber -having only a helium atmosphere between the vacuum section and the detector.

The use of a 50 mm-deep helium cone between the sample and the detector (the largest possible depth for the closest sample-to-detector distance in the current beamline design) improves the transmission of a 4 keV beam from ~40% up to a 61% of the incoming beam (Figure 6). In terms of background noise, although the helium cone also provides a general improvement of the signal/noise ratio, such improvement is going to be moderate due to two factors:

- the presence of the two window films (likely kapton), used to contain the helium gas inside the cone, will also scatter some of the diffracted photons and contribute to the background
- the main source of the background is the interaction of the direct beam with the air in the beam path between the collimator and the beamstop. The cone does not prevent this noise since it is placed *after* the beamstop.

In general, the figures obtained with the helium cone can be improved by reducing the air sections crossed by the beam path: complementing the helium cone with the use of a helium cryostream, transmission at 4 keV increases to 72%; circulating helium gas through the collimator further improves it to nearly ~80%. These solutions, however, involve the release of helium gas directly to the hutch atmosphere, with no chance to recover it, thus increasing safety concerns and running costs.

On the other hand, the use of a helium chamber, which prevents the beam from interacting with air along the entire non-vacuum section of the beam path, maintains the transmission of the beam at nearly 100% for all the energy range of the beamline (50% more transmission at 4 keV than with the helium cone). In terms of signal-to-noise preservation, helium chamber drastically reduces the background noise due to Compton scattering, Thompson scattering and photoelectric absorption (Figure 8 and Figure 9). A helium chamber not only prevents flux loss at low energies, but will also increase data quality *at all energies*.

Thus, the ES will be enclosed in a helium chamber to maintain a controlled environment around the sample. Data collection can be performed in helium, by circulating helium gas through the enclosure, or in air, in which case the experimental chamber can be opened to air atmosphere. In both environments, samples can be measured either at room temperature or under cryogenic conditions, by blowing a cryo-jet of either cold nitrogen gas or cold helium gas onto the sample, depending on whether the measurement is performed in air or helium.

The time required to change from the air to the helium atmosphere setup is expected to be of the order of 1 hour or lower, whereas the change from helium to air atmosphere should be done in the order of minutes.

He recycling and operational costs

A helium chamber involves the use of large volumes of helium, which inevitably increases the running costs. Preliminary calculations suggest a continuous usage of <15 L/min of helium gas, which would take up a significant portion of the beamline running budget. Thus, the chamber design should include the possibility to recycle the helium gas, directing it to the helium liquefaction, located next to the XAIRA EH.

Detailed operational costs associated with the use of helium are described in section 12.

5.5 Sample mounting/unmounting

Given space restrictions around sample position and the presence of the Helium chamber enclosure, sample mounting/unmounting operation will be preferably performed by an automated sample changer system, similar to the one used in many MX beamlines, including XALOC.

In XAIRA, samples will be mounted on a vertical spindle goniometer, thus the robot gripper will need to access the diffractometer from above the sample, and though the Helium chamber enclosure. Thus, for operation in helium atmosphere, the gripper will need to enter the chamber through a dedicated gate valve. To minimise nitrogen gas release within the Helium chamber, dry mounting is foreseen for cryogenic pins.

Unmounting of a sample and mounting of the following one should not take longer than 20 s, if a double-gripper is used, or ~40 s if a single gripper is used.

The liquid nitrogen dewar for sample storage should have a capacity for 25-30 Unipucks (accounting for 400-500 pins). Such sample capacity is expected to cover at least 20-24 hours of operation. It is not foreseen to have SPINE-style pucks (holding samples stored in liquid nitrogen-filled vials) in the sample storage dewar, since introduction of nitrogen-filled vials into the Helium chamber would severely contaminate the Helium atmosphere. Users storing their samples in vials can transfer their pins to Unipuck plates by using the ALBA-developed PuckOs system.

A room temperature hotel with space for at least one puck is also considered; this will be used for both room temperature samples and some beam monitoring tools mounted on pin bases.

5.6 Cryostream configuration

The cryostream laminar flow used to maintain the sample at cryogenic temperatures will exert a drag force on the sample support, which can affect the sample positional stability. To minimise the negative impact such force can exert on data quality, several tests were performed to determine the optimal configuration for the cryostream.

Optical vibrations measurement

Sample vibrations induced by an impinging gas stream on a sample were measured with a video-microscope with a high speed camera (1 kHz frame rate). Computational analysis of the acquired images allowed evaluation of relative displacements of the images with a resolution of about ~20 nm. With this system, the vibrations induced by a cryostream flow on a vertically mounted MicroMesh 700/25 support were assessed for three cryostream configurations: vertical (cryostream flow aligned with sample pin and spindle axis); horizontal (cryostream flow parallel to the floor and normal to the pin); and at 45º (where cryostream axis is positioned at 45º from both the spindle axis and the floor plane). Further details can be found at https://confluence.cells.es/x/FIDNDw.

These measurements, summarised in Figure 10, show that amplitudes of the oscillations induced by the cryostream flow are much smaller than what was anticipated, staying below the 20 nm even in the worst scenarios the oscillations. These values fall far below the error

threshold expected from the other components of the sample positioning system (i.e. less than 100 nm for sphere of confusion of the goniometer), so cryostream-induced vibrations will not be considered as a restriction for the End Station design.

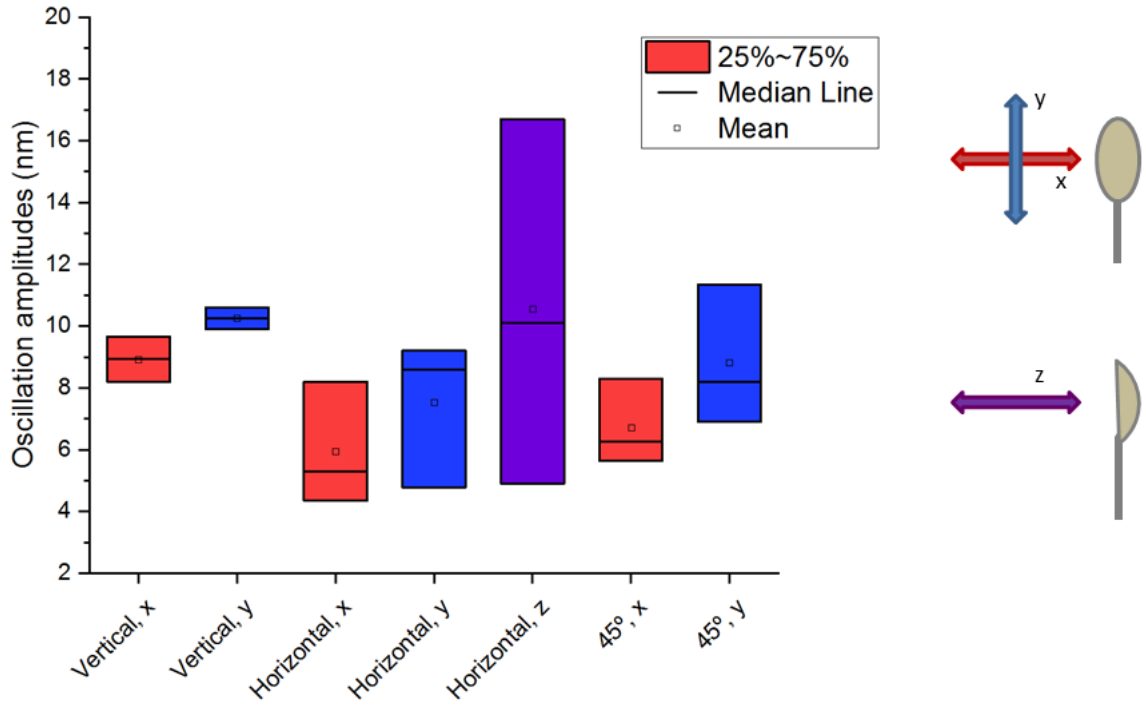

Figure 10. Oscillation amplitude variability between different sample holder orientations for each cryostream configuration. Each dimension of the movement is depicted in a different colour (x, transversal with respect to the beam axis, in red; y, vertical, in blue; z, longitudinal, in purple). Labels in the x axis refer to the cryostream configuration. Box plot shows the Q1, median and Q3 values; borders define the maximum and minimum values for each category.

Computational fluid dynamics on cryostream flow

The temperature profiles and flow velocity profiles were calculated for 4 different cryostream configurations (see Figure 11). The most favourable scenario in terms of thermal stability of the pin and minimisation of impact on the positioning system elements would be the horizontal cryostream configuration.

Further details can be found in the FEA and CDF analysis of the sample environment for the assessed cryostream configurations: https://confluence.cells.es/x/2IDNDw

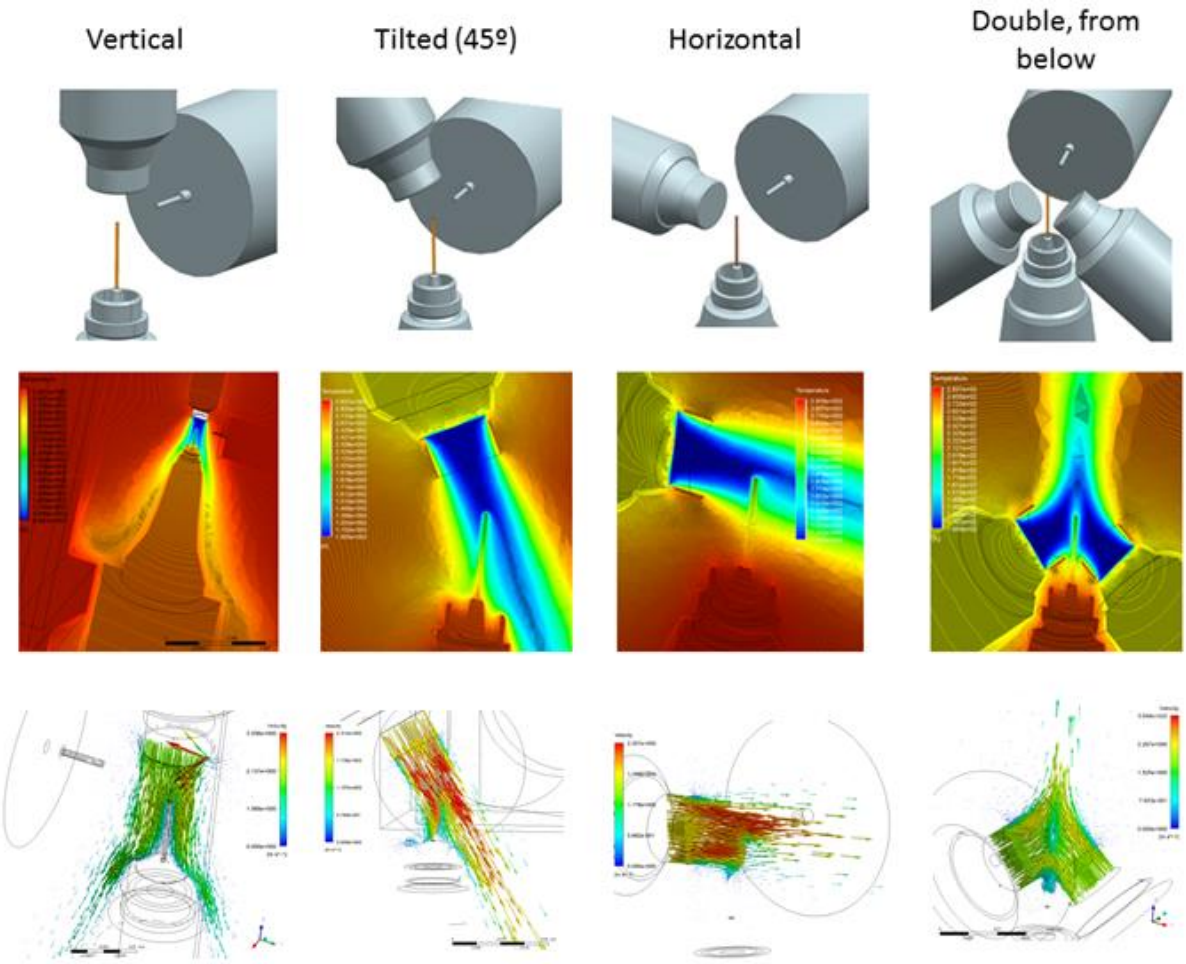

Figure 11. Temperature and velocity distribution around the sample for each considered configuration. *Top row:* scheme of the proposed configuration; *Middle row:* Predicted temperature distribution. Scale ranges from 100 ºK (dark blue) to 293.7 ºK (dark red); *Bottom row:* Predicted fluid velocity. Scale ranges from 0 m/s (dark blue) to 3.2 m/s (dark red).

Optimal cryostream configuration

Given the above results, and to minimise any temperature gradients induced by the cryostream on the goniometer head stages and/or other elements of the sample positioning system, which could led to drifts in the position of the sample upon sample rotation or mount/unmount operations, the preferred cryostream configuration for XAIRA ES will be horizontal (parallel to the ground) or slightly tilted (<15º) with respect to the sample rotation axis.

The cryostream nozzle is to be positioned very close to the sample (~6 mm). The final configuration should also be optimised to avoid shadowing of the cryostream nozzle on the diffraction cone projected from the sample to the detector.

The (nearly) horizontal configuration can also be beneficial as it may allow the sample changer gripper to access the sample position without need for further cryostream movements. This would be desirable, since it would simplify the mechanical set up of the cryostream and its dependencies for triggering the sample changer robot actuation.

5.7 Detector and detector positioning for diffraction data collection

To collect diffraction data for the experiments envisaged for XAIRA, the beamline will be equipped with a highly-performing hybrid photon counting detector.

Detector required capabilities

The detector envisaged for XAIRA is a pixel-array photon-counting detector able to reduce the detector image background by discriminating (not counting) the different sources of noise and to collect at very high frame rates in shutterless mode.

The detector should comply with the following requirements:

- High Detective Quantum Efficiency (DQE), so that the largest possible fraction of incoming photons is detected, and irradiation dose of samples can be kept to the minimum. Required value: near 100% in central energy range of the beamline (7-13keV), highest possible in the rest of the energy range.

- Large active area for wide angular coverage, to ensure high resolution data being efficiently collected without having to approach the detector too close to the sample. Required value: minimum area of 230 × 230 mm^2 (so to reach at least 1.0 Å resolution at detector edge with a beam at the Se absorption K-edge (0.979 Å), at the minimum sample-to-detector distance of 70 mm).

- Small pixel size, for background minimisation and for accurate peak position determination, especially at small sample-to-detector distances. Required value: <100 × 100 μm^2.

- Small point spread function, to grant a high spatial resolution. This is especially relevant when collecting at short sample-to-detector distances and to resolve large unit cells. Required value: <100 μm.

- High count rate, to ensure accurate measurement of the strongest reflections. Required value: ≥10^7 photons/s/pixel.

- Noise-free detection, with virtually no readout noise or dark current, to ensure accurate measurement of weak reflections and to maximise data quality (i.e. signal-to-noise ratio $I/\sigma_{(I)}$). Required value: average detector background of <0.1 counts/hour/pixel (excluding cosmic rays).

- High dynamic range, so that weak and strong reflections can be measured simultaneously. Required value: >16 bit, assuming one bit or less lost by noise.

- Uniform active area, so that response is homogeneous along all detector area and intensity differences can be measured accurately. Given that in crystallography experiments each Bragg peak may be concentrated on a few pixels, uniformity of the detector is critical for the correct assignment of symmetric reflections and is critical for collection of usable anomalous signal.

- High frame rate to allow for continuous data collection. Required value: ≥500 Hz when operating at full detector area mode, for a minimum of 10k continuously acquired frames.

- Small dead time between frames, required to avoid read-out gap noise, which can have a large negative impact on data obtained with shutterless data collection due to loss of entire reflections (J. Holton 2017, ccp4b mailing list). Dead time between frames should be

negligible with respect to acquisition times. Required value: <10 µs (that is, 0.5% of the minimum exposure time (considered 2 ms, for a 500 Hz frame rate), so as to accept a maximum 1% overall uncertainty when considering both dead times for the start and the end of the frame collection).

- Adjustable energy discriminating thresholds. Ideally 2 independent thresholds, to simultaneously filter high energies (to mitigate harmonic contamination) and low energies (to remove background and avoid double counting of single photons in adjacent pixels).

- Several available triggering modes. The detector should accept both internal and external signals as trigger; and allow triggers for each image (multi-trigger) as well as for a series with multiple images (start trigger). All should involve negligible jitter times, in the order of sub-µs.

- Room temperature operation of all components, so no additional cooling systems are required, is valuable.

- Compact housing, to facilitate the integration in the crowded sample environment of the beamline.

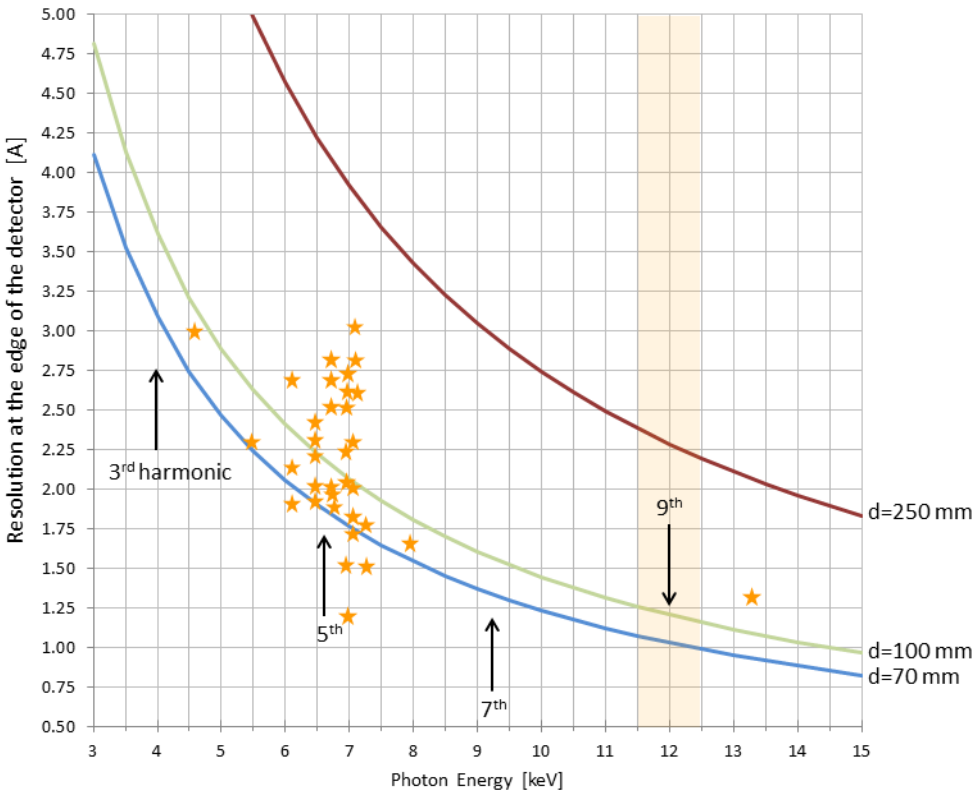

Figure 12. High resolution recordable at 115 mm from the beam centre, as function of the beam energy, for a detector set at 70 mm (blue), 100 mm (green) or 450 mm (red) from the sample. Values for the currently reported structures solved by native-SAD phasing are represented as golden stars. Shaded region highlights the most commonly used energy range (around 12keV).

Detector positioning for data collection

The detector active surface will be positioned normal to the beam axis, to record the diffraction cone arising from the sample being illuminated by the X-ray beam. To allow data collection at different resolutions, the detector will be mounted on a longitudinal stage, in order to change the crystal-to-detector distance.

The distance between sample and detector active area is a critical parameter to access the high resolution data. To allow for a successful use of diffraction data for native-SAD phasing at low energies (yellow stars in Figure 12, based on reported data), the closest sample-to-detector distance for XAIRA beamline will be set to 70 mm. For a detector with an active area of 230 × 230 mm^2, this results in highest achievable resolutions of about 3 Å, 1 Å and 0.9 Å at 4 keV, 12 keV and 14 keV, respectively.

For those applications requiring sub-Å resolutions (e.g. chemical crystallography), an alternative setup will be used to extend the high resolution limit of the recorded diffraction. In this configuration, the detector will be moved sideways so that the sensitive area centre is not aligned with the beam and one side of the detector is exposed to higher Bragg angles. A compromise needs to be sought between maximising the achievable resolution (Figure 13, left axis) and minimising the percentage of the diffraction signal that falls out of the detector sensitive area (Figure 13, black line), which impacts in dataset completeness and multiplicity. The proposed offset (100 mm) yields a maximum attainable resolution at edge of 1.05 Å at 10 keV and 0.75 Å at 14 keV, with ~60% of the diffraction data falling out of the detector sensitive area. A larger excursion of the detector (~250 mm) to allow removing the instrument from the beam path is advisable.

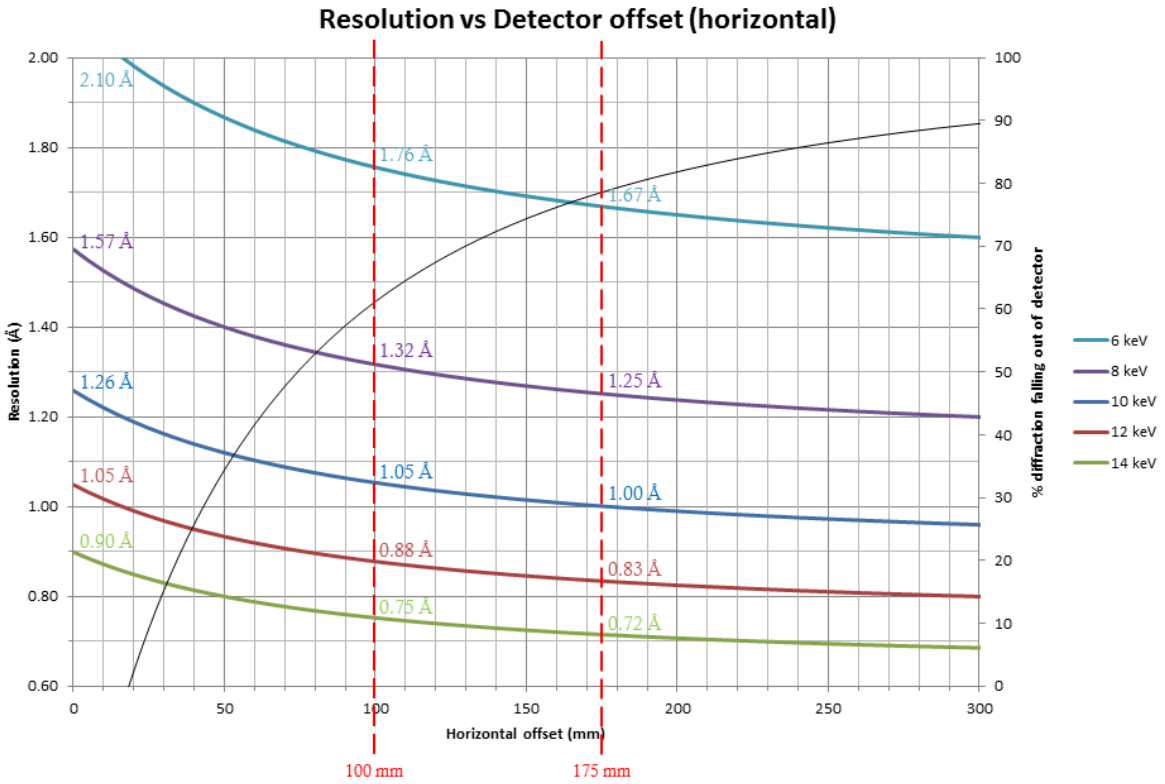

Figure 13. Maximum resolution achievable at detector edge as function of a vertical offset of the detector. The resolution at the edge of a detector with an active area of 230 × 230 mm^2, for offsets of 100 mm and 175 mm and is indicated for each energy. The black line represents the approximate percentage of diffraction data (up to the edge resolution) that would fall out of the detector sensitive area.

5.8 Beam alignment strategy

A detailed study was done to determine how all the possible degrees of freedom of all the optical elements of the beamline (namely the three mirrors and two beam-positioning monitors) affect the size and position of the x-ray beam at the sample plane. This error budget was calculated by ray-tracing, evaluating the response of the beam after introduction of random errors around the nominal position for each positioning degree of freedom of each of the optical elements.

The considered errors in the positioning of the relevant optical elements of ±10 µm and ±10 µrad are realistic when considering mid-term and long-term drifts and cover largely the amplitude of vibrations.

Further details can be found at section 10 and in https://confluence.cells.es/x/MwCzDg

Simulations showed that the uncertainty for the spot position in the vertical plane is larger than in the horizontal plane, and in both cases much larger than the estimated spot size - and therefore, unacceptable (Figure 14). Regarding the spot size, it becomes apparent that with the estimated positional errors of the optics elements, the actual incidence angles on the mirrors change enough to defocus the beam, even if the ellipses were perfectly stable. This ultimately leads to unacceptable vertical and horizontal spot sizes at the sample plane, as shown in Figure 15.

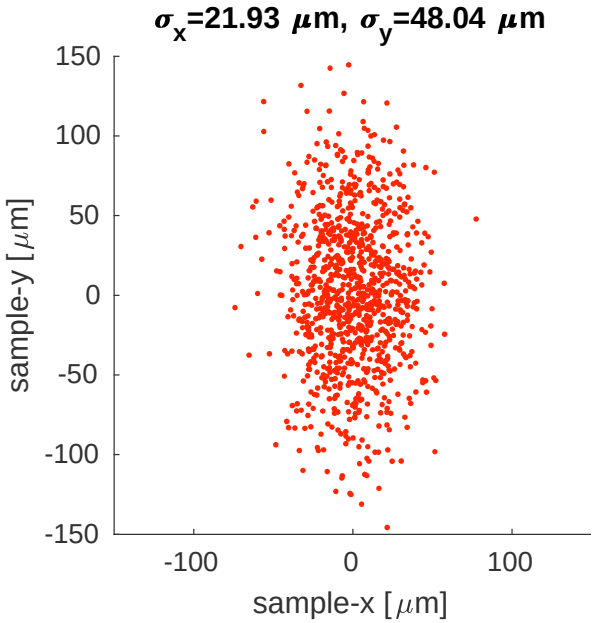

Figure 14. Uncertainty of the beam spot position on the sample plane as given by the uncertainty of the physical degrees of freedom of the optical elements of the beamline. Calculated from 1000 realizations of noise.

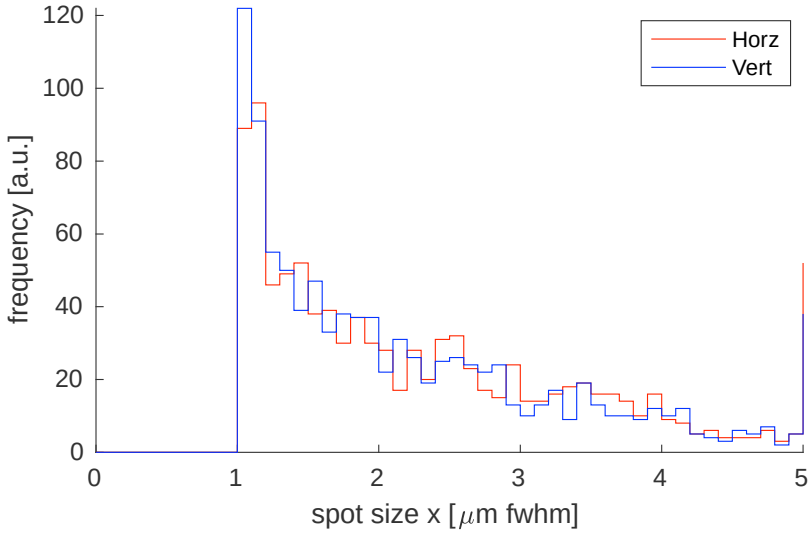

Figure 15. Histogram of the spot size, assuming perfectly stable ellipses, but misalignment of the optical elements. Calculated from 1000 raytracing simulations with stochastic positioning errors of the relevant optical elements.

These simulations highlight the need for a system to monitor the precise position of the optical elements, to be able to infer and correct the size and position of the beam at the sample plane.

5.9 Beam size tailoring

The portion of the beam interacting with any matter other than the sample crystal may only contribute to the background of the diffraction image and reduce the signal-to-noise ratio.

Adjusting the beam size to that of the sample minimises the noise originated by background scattering (i.e. regions of sample support and mother liquid surrounding the crystals which are also illuminated by the beam). This operation can have a significant impact on diffraction data quality, especially in the case of microcrystals, for which the smaller diffraction volume makes the diffraction intensities weaker than those of conventional larger crystals [26].

As described above, beam size at nominal sample position (KB focus) is of 3.1 × 0.7 μm^2 (H × V, FWHM), at 12.661 keV. Such dimensions, however, can be modified in various ways to enlarge or further reduce them, to adapt them to user's needs.

The horizontal beam dimension can be further trimmed to 1 μm by closing the horizontal secondary source slits at the HPM focus (Figure 16b). No provision is made to further reduce the beam in the vertical direction.

To increase the beam size, two different (and complementary) strategies are considered: unbending the mirrors to defocus the beam and displacing the sample along the beam axis out of the beam focus.

Unbending the VFM and/or HFM mirrors to defocus the beam (Figure 16c) is a standard operation in other MX beamlines. However, the high demagnification factor of the KB mirrors in XAIRA can make it less reproducible, and is strongly dependent of the correct alignment of the beamline.

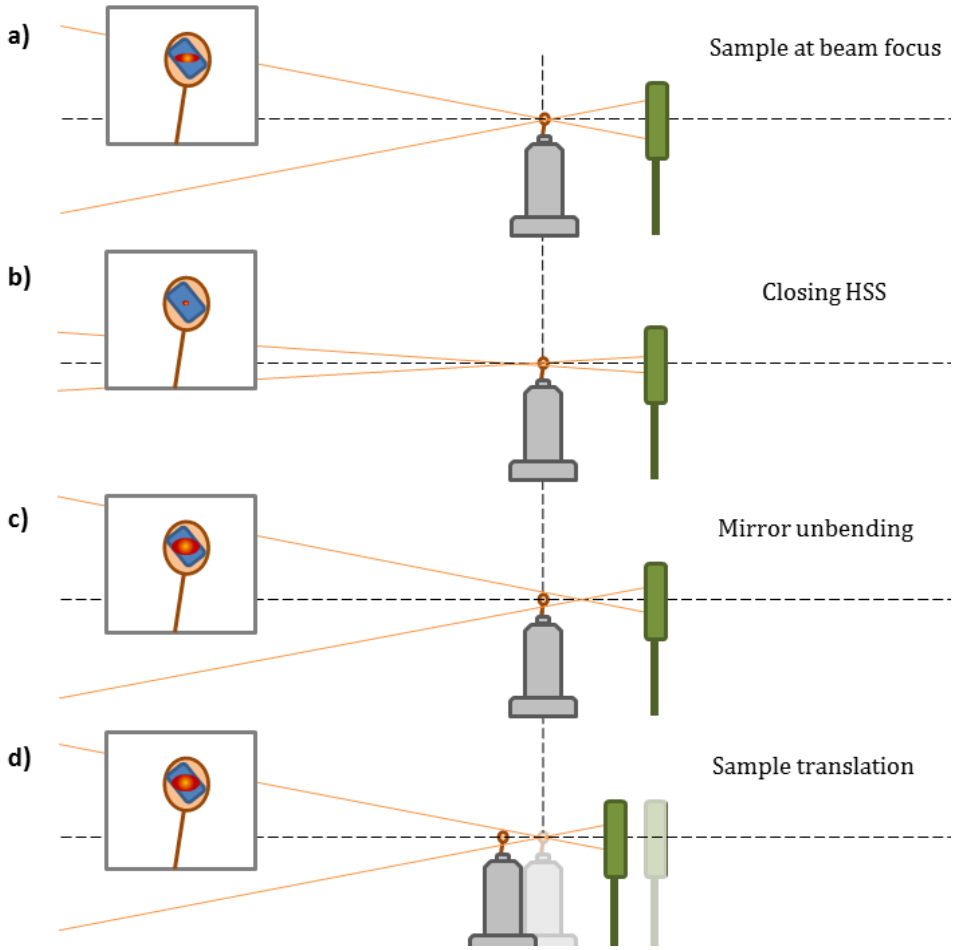

Figure 16. Beam tailoring strategies. a) In the default condition, the sample is aligned with the KB focal point. **b)** Closing the HSS slits, placed at the focus of the first horizontally focusing mirror, reduces the horizontal dimension of the source. **c)** Relaxing the bending of the KB mirrors it is possible to displace the focal point to a new position downstream of the sample. This results in a larger beam at the nominal sample position (vertical dashed line). **d)** Additionally, the sample itself can be translated along the beam axis, out of the focal point, so that it is illuminated by a larger beam.

In contrast, defining the size of the beam at the illuminated sample region by moving the sample along the beam axis (Figure 16d) is a simple operation. The use of predefined positions allows a fast (& controlled) change of beam size. The main limitation of this strategy, though, is that the space restrictions around the sample position limit the stroke of the diffractometer longitudinal translation. Additionally, sample also needs to be kept within the cryostream laminar flow at all times. Thus, this offset from focal point will be limited to ~4 mm, yielding a maximum beam size of 15 x 1.6 μm^2. A larger defocus distance would be possible in the case that the pointing direction of the cryostream could be moved along the beam axis.

	0 mm	1 mm	2 mm	3 mm	4 mm	8 mm
H (µm, FWHM)	3.1	4.7	7.8	11.2	14.7	29.0
V (µm, FWHM)	0.7	0.8	1.0	1.3	1.6	3.0

Table 4. Beam dimensions at different distances from the KB focal point

These two strategies can be combined to achieve the desired beam size at sample.

5.10 Beam monitoring

Several elements have been introduced in the beamline design in order to monitor relevant beam parameters, such as size, shape, position or flux. A list of the proposed elements and their use for beam characterisation is shown in Table 5.

	Element Position	Beam position	Beam size	Beam shape	Flux
FSM 0	Upstream mono		√	√	
FSM 1	Downstream HSS	(√)	√	√	
FSM 2	Upstream KB	(√)	√	√	
FSM 3	Downstream KB	(√)	√	√	
FSM 4	Post sample	(√)	√	√	
YAG on pin	Sample position	(√)	(√)	(√)	
XBPM system	Whole beamline	√			√
Wire on pin	Sample position	(√)	√	(√)	
Diode 1	Downstream KB				√
Diode 2	Post sample				√

Table 5. Proposed beam monitoring elements, their position and their readout. Ticks indicate when a particular beam parameter can be evaluated by el considered element. Ticks between parentheses indicate that element is not optimized to determine the parameter. Legend: FSM, Fluorescent Screen Monitor; YAG, Yttrium Aluminium Garnet scintillator screen; XBPM, X-ray Beam Position Monitor.

6 End station overview

X-ray beam path

As shown in Figure 17, beam arriving to the Experimental hutch will pass through a set of beam cleanup apertures and hit the fluorescent screen or the attenuator foils if inserted, before reaching the KB mirrors. Downstream the last optical element, the HFM mirror, beam will pass through another beam monitoring unit, the fast shutter, a second set of apertures and the second XBPM detector, before exiting the vacuum section through the diamond window. Once in the Helium chamber, the beam will pass through the drilled optical components of the on-axis microscope, through the collimator if inserted, and reach the sample position. Downstream the sample, the direct beam will be stopped by an insertable beamstop. Alternatively, it can be allowed to continue until the post-sample beam monitoring unit, located just upstream of the detector.

In case the Helium chamber is operating in helium atmosphere, the X-ray beam will propagate solely in vacuum and in air up to the detector. The controlled atmosphere along the beam path will allow a better control of the ambient conditions and will reduce the effect of the air humidity, which has been proven to be critical in the reliability of the automated sample system in XALOC.

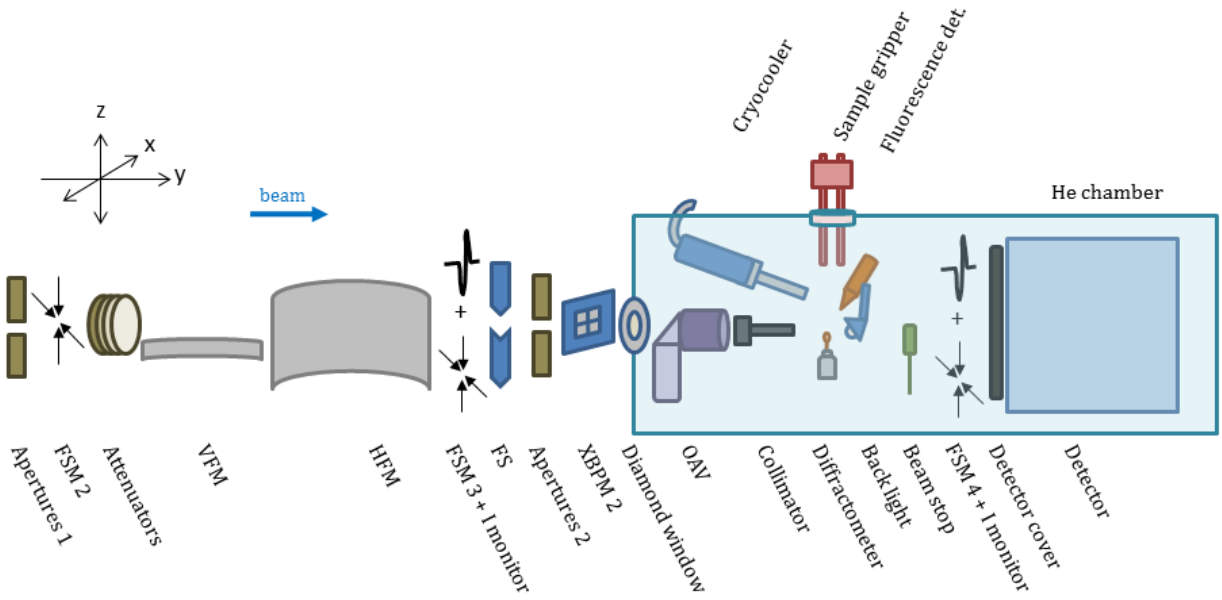

Figure 17. Schematic view of the proposed End Station elements. Beam travels along the y axis. Elements aligned to the beam, from left to right: aperture slits; fluorescence screen; attenuators; vertical focusing mirror; horizontal focusing mirror; fluorescence screen/intensity monitor; fast shutter; aperture slits; beam positioning monitor; diamond window; on-axis viewing system; capillary collimator with scatter guard; sample holder; beam stop; fluorescence screen/intensity monitor; direct electron detector, with cover. Other elements in the ES are: cryostream, sample changer, fluorescence detector; backlight; Helium chamber.

7 Proposed technical solutions

7.1 Helium chamber

Chamber layout

A chamber of 600 x 780 x 1100 mm^3 will be installed to cover the sample environment, including from the beam conditioning elements to the detector.

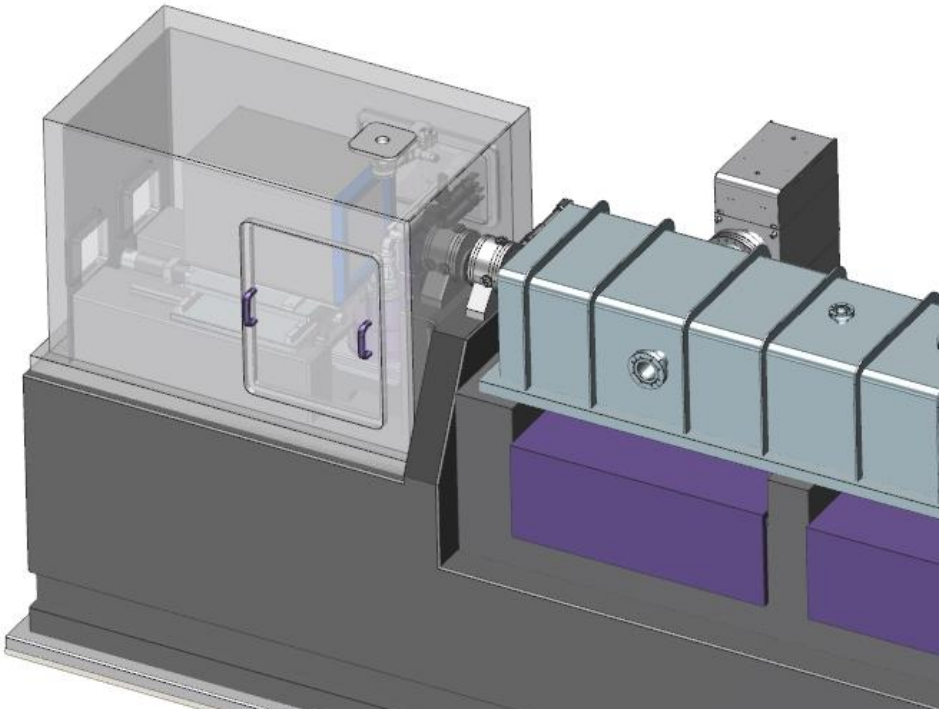

Figure 18. The helium chamber will contain the atmosphere around the sample environment.

The chamber will rest on the granite and will include several openings (Figure 19):

- The beam entry point will be fitted with a PVC bellow to isolate the beam from any vibrations of the chamber. The chamber seal around the beam flight tube will be located between the two flanges containing the beam conditioning elements.

- Vacuum-tight feedthroughs will be installed for the cabling and supplies required for the instruments contained in the chamber.

- Removable panels will allow access to the diffractometer and the sample environment. The inbound side panel will hold the entry of the cryostream nozzle, which will be fitted with PVC bellows to isolate the chamber from cryostream-derived vibrations.

- A pneumatic UHV gate valve will be fitted on the chamber top panel, to allow access of the sample changer gripper. This valve, used to prevent contamination of the helium atmosphere with air, will work in a similar way to similar gate valves fitted in other helium chambers, such as the one in BL1A at Photon Factory [25] or in the ESB-MX instrument at SwissFEL [28]. The sample changer valve is located at 305 mm from the sample, to make it compatible with the grippers typically used in most MX beamlines.

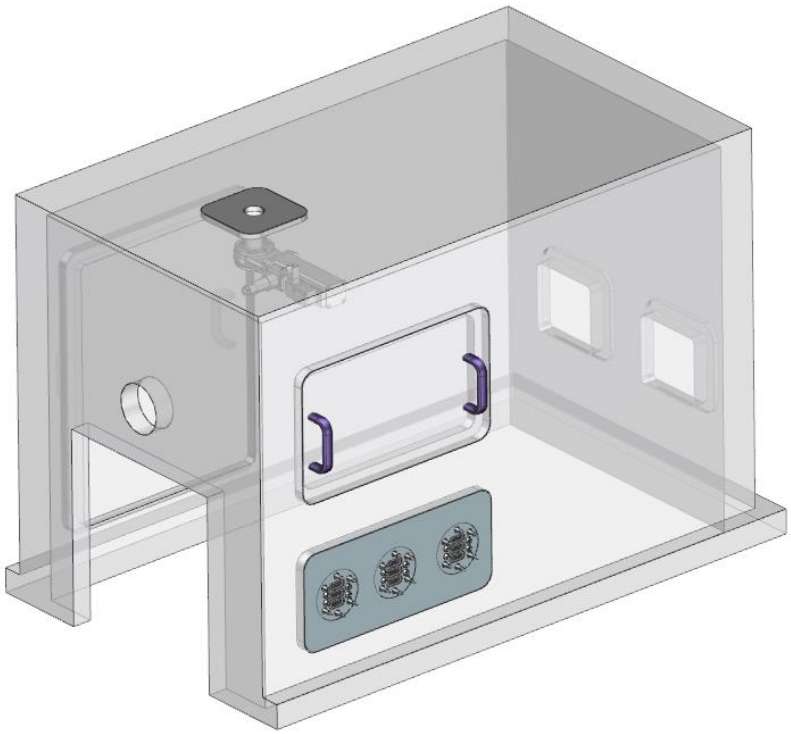

Figure 19. Layout of the helium chamber, showing the removable panels and the openings. These openings will be fitted with vacuum-tight feedthroughs or flanges, and in some cases sealed with PVC bellows

Cryostream as He source

Samples will be maintained under cryogenic temperatures by means of a laminar stream of cooled gas. This continuous gas flow will be used as helium gas input for the chamber. Since the beamline can also be used with an air atmosphere (and still under cryogenic conditions), a cryostream system will be chosen that is able to work with both helium and nitrogen gases. This way, only one cooling system needs to be installed in the helium chamber, thus allowing a faster change between in-air and in-helium conditions.

The cryostream nozzle will be positioned on the horizontal plane (xy plane), with a 10-15º tilt respect to the beam axis, in order to avoid interference of the cryostream nozzle with the sample diffraction cone.

The chosen cryostream instrument has the nozzle separated from the refrigerator column by a flexible line, which facilitates the decoupling of mechanical vibration from the helium chamber. The refrigerator column will be positioned as far as possible from the chamber and will be fitted with means for passive suppression of vibrations. The refrigerator, in turn, is also connected to a closed loop compressor, which will be placed outside the hutch.

Helium cycle

Helium gas blown into the chamber by the cryostream and leaked from the goniometer will be directed through a recovery circuit to the ALBA Helium liquefaction plant, located close to the XAIRA EH.

The liquefaction plant will able to purify and reliquefy the chamber output gas, thus greatly reducing the operational costs and environmental footprint, provided this output helium gas has a purity of at least 98%.

To this end, the chamber design is optimized to reduce leaks and will be fitted with vacuum-tight feedthroughs, viton-sealed flanges and a gate valve to protect the sample robot entry site (see above). The output purity for this chamber will need to be evaluated during the prototyping phase, but similar chamber designs, such as that in BL1A beamline at Photon Factory, are able to achieve and maintain a helium atmosphere with over 98% purity (as reported in [25] and in personal communication by N. Matsugaki).

Detailed operational costs can be found in section 12 (Appendix III)

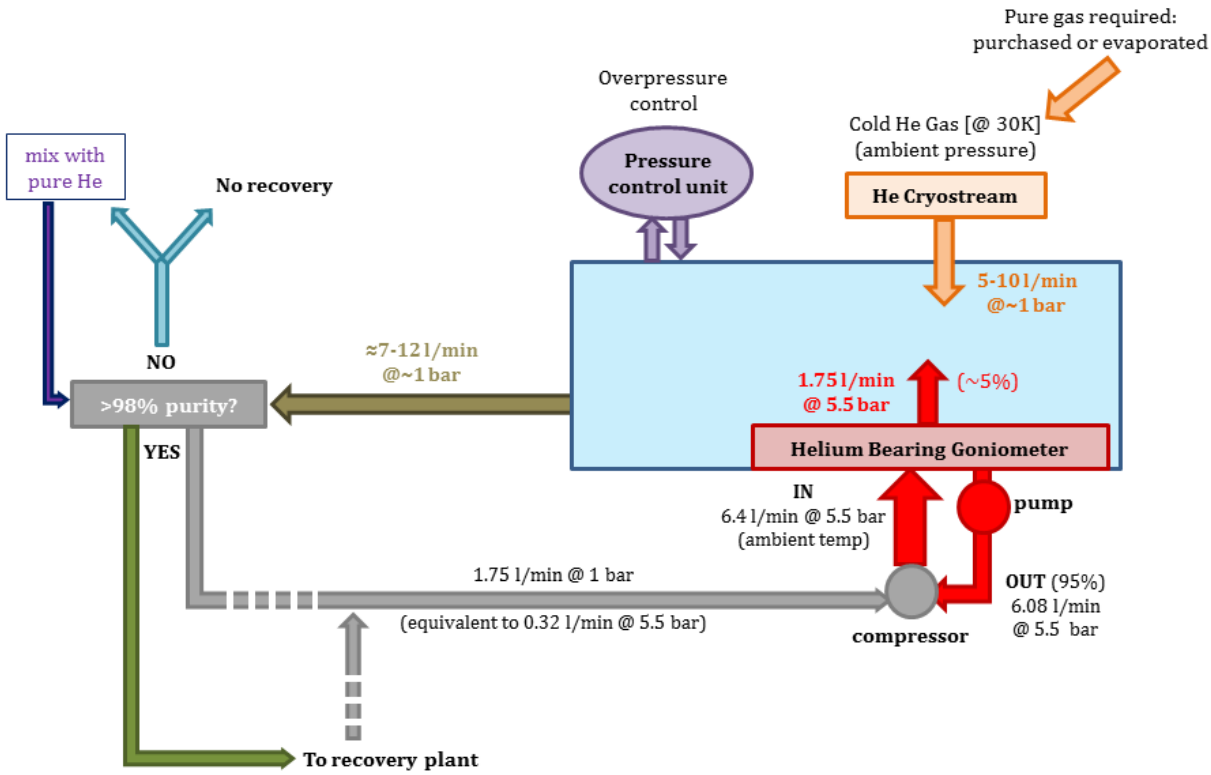

Figure 20. Helium gas circuit through the XAIRA ES chamber.

The helium bearing goniometer requires a compressor to restore the 5.5 bar of the input flow. To minimise the impact on the positional stability of the End Station elements, this compressor will be located outside the EH and installed on damping pads and other means of passive suppression of vibrations.

7.2 Diffractometer

Helium-bearing goniometer

The expected size of the samples examined at XAIRA is in the micrometer range. Thus, the beamline diffractometer will need to achieve sphere of confusion smaller than 100 nm. Such sphere of confusion cannot be achieved when using a mechanical bearing rotor, so this type of rotary stages is not considered for XAIRA goniometer.

A much more precise alternative, an air-bearing rotary stage, is preferred. However, this type of rotors uses a pressurised flow of air, which would be released in the helium chamber, thus resulting incompatible with the establishment of a helium atmosphere in the sample environment. To bypass this incompatibility, a helium-bearing goniometer will be used in XAIRA.

The proposed solution is based on a Helium Bearing and a DC Brushless Torque motor (direct drive). One possibility for the helium bearing rotor is a design with a foreseen sphere of confusion of 70 nm or less. This goniometer would use 35 l/min of helium gas at 5.5 bar, but would also be able to work with air (at the same pressure).

PERFORMANCE	**Sphere of Confusion (SoC)**	≤ 100 nm	
	Maximum Speed	360 deg/s	60 rpm
	Angular Repeatability	≤ 0.1 mdeg	
	Angular Resolution	0.04 mdeg/step	25600 steps/deg
LOADS	**Maximum Axial Load**	9kg	90N
	Maximum Torque	1.4 Nm	

Table 6. Requirements for the XAIRA goniometer.

Stages

Based on the strict requirements on positional resolution, speed and strokes of the different axes (see section 11.12), two different types of linear motion stages will be used:

- For the linear motions of the spindle axis (pale blue stages in Figure 21 scheme), stepper motor-driven and cross-roller bearing guided motion stages will be chosen.

- For the sample-centring motions (goniometer head; cyan stages in Figure 21 scheme), piezo-driven guides will be used.

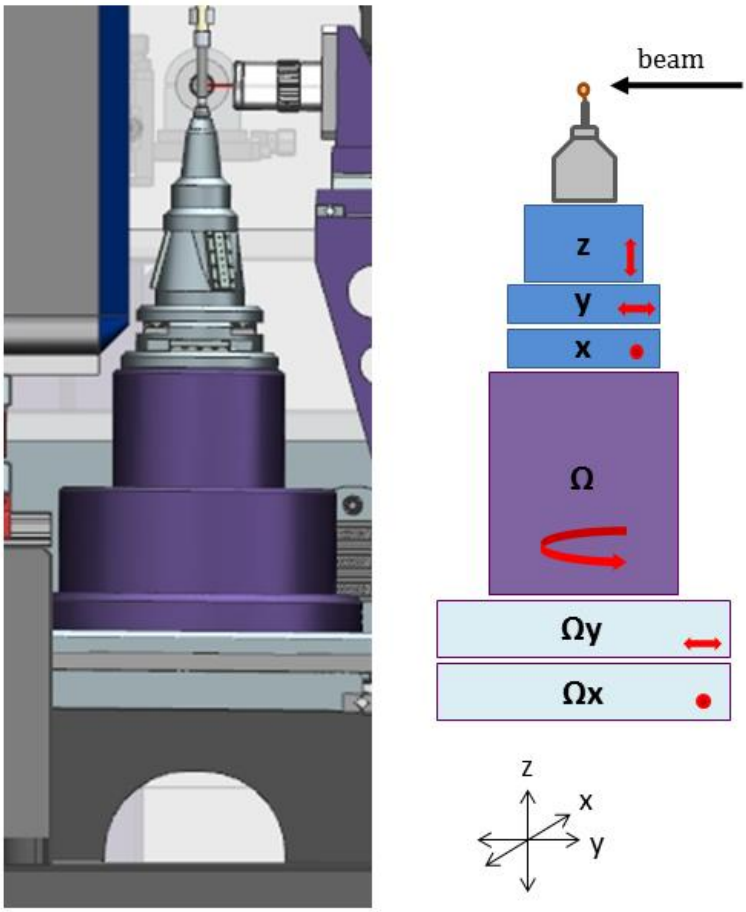

Figure 21. Proposed stages for XAIRA diffractometer. Omega transversal and longitudinal stages (pale blue) will allow alignment of the spindle axis of the goniometer (purple) with the beam. Sample centering stages (cyan) on goniometer head will be used to align the sample to the beam.

Sphere of Confusion correction

The goniometer is estimated to perform with a SoC better than 70 nm. However, it is expected that this figure will increase when it is combined with the errors arising from the linear stages above and below the goniometer.

Therefore, the system must be compatible with a possible correction of the SoC by using the XY stages with sample-centring piezo-driven stages (similarly to what is done in FMX beamline at NSLS-II [29]).

The error budget of the diffractometer will be presented in the corresponding Preliminary Design Report of this part of the project.

Serial crystallography stages

An alternative sample centring stage will be used for *fast* scans, intended to collect non-oscillation data from SX chips (Figure 22). This is to be installed on top of the goniometer or above it, on a support resting directly on the granite, and will be similar to that described in

[3], based on three linear translation piezo-driven guides, each with ~50 mm of travel. Such setup can achieve speeds of 20 mm/s while maintaining resolutions of ~1 nm.

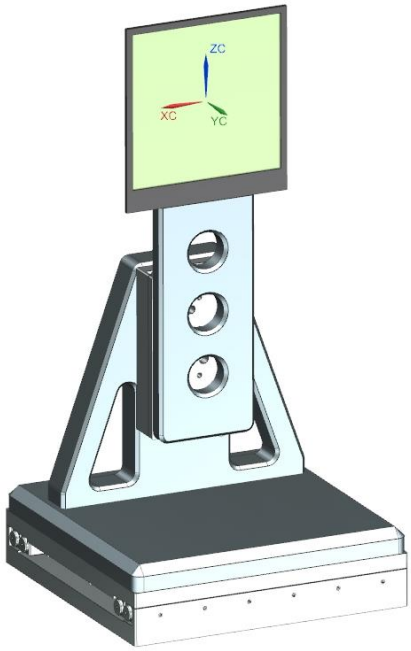

Figure 22. Stages for fixed-target serial crystallography fast data collection.

7.3 On-axis microscope and sample illumination

The on-axis microscope specifications are given in section 5.3. The design, as shown in Figure 23, is based on 2 exchangeable microscope objectives, one with a high numerical aperture (capable of providing an optical image with a high resolution) and the other with a small numerical aperture (able to provide a large field of view). These objectives are aligned with the photon beam axis by means of an objective changer plate.

A beam splitter and a 45 degree mirror is used to split the optical image to a branched lens system, with one high magnification (2.5×) lens tube and a low magnification (0.4×) one, each connected to a CCD/CMOS camera.

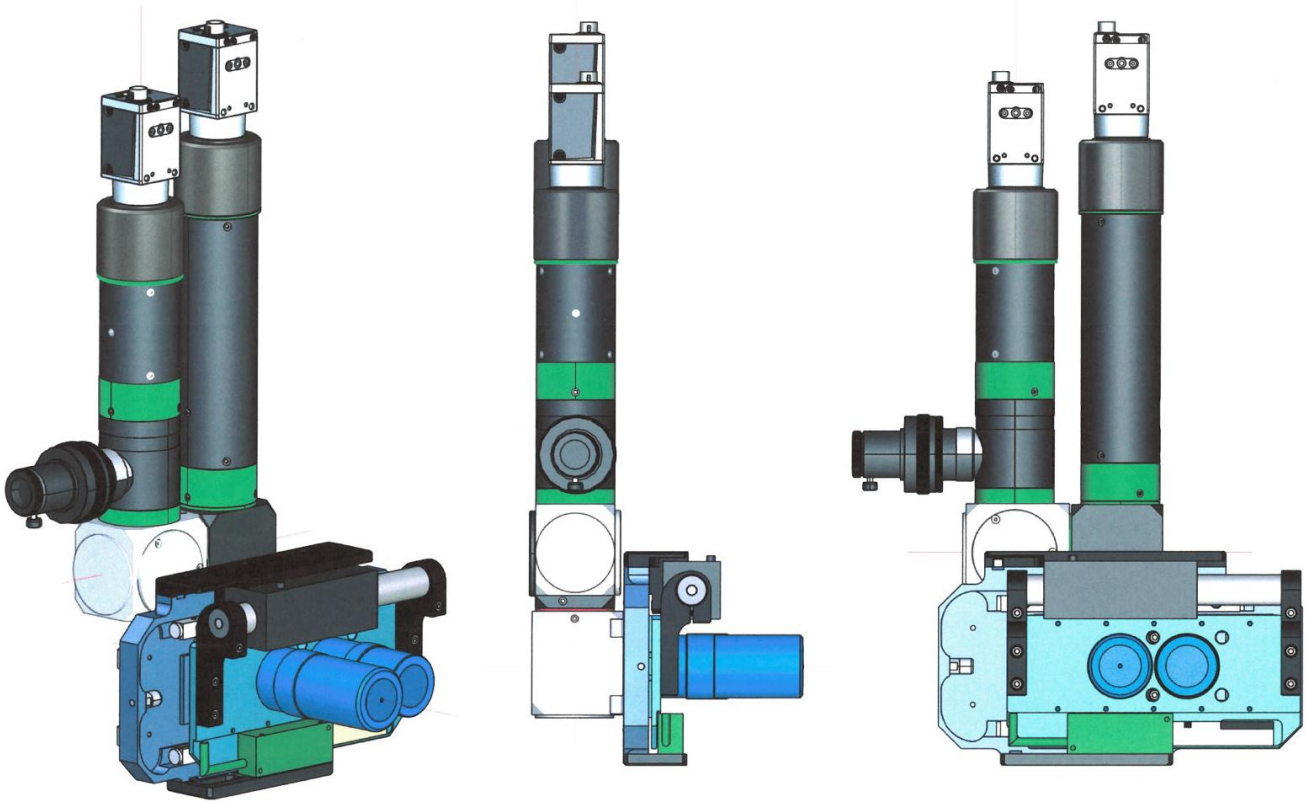

Figure 23. Layout of the proposed OAV system

The combination of the two objectives and the two lens systems yields 4 views or "zoom levels" covering a large range of magnifications (Table 7), from a large field of view of over 3 × 3 mm^2 to a sub-micron resolution view.

Lens system	Microscope objective	Total magnification	FoV (H × V, mm^2)	Max theoretical resolution (µm)
Low Mag branch (0.4×)	5×	2×	4.4 × 3.3	> 2
High Mag branch (2.5×)	5×	12.5×	0.7 × 0.5	2
Low Mag branch (0.4×)	50×	20×	0.44 × 0.33	> 0.65
High Mag branch (2.5×)	50×	125×	0.07 × 0.05	0.65

Table 7. Estimated specifications for the proposed system with 2-branches and 2-objectives. Values calculated for white light illumination.

The use of objectives with the same parfocal distance allows switching between objectives without need to adjust the distance between the OAV system and the sample.

As the microscope objective is coaxial with the photon beam, a 1 mm central channel must be drilled penetrating the centre of each lens of the objective. A molybdenum tube is fitted in this channel to protect the glass from the X-ray beam and to reduce the scattering. This modification inevitably reduces the performance of the objective and makes it much more expensive, so it could be applied only to the high magnification objective (50×); since the low magnification imaging is mainly used for sample alignment steps, which are done in absence of X-ray beam illumination of the sample, the central channel can be spare for this objective.

Alternatively, a commercial solution could also be used. Similar systems are currently offered, using a single objective connected to a branched lens tube. The performance of such systems is not as good in terms of magnification (its theoretical maximum resolution is almost two-fold lower; Table 8), but it poses a much smaller risk as would require little or no development from ALBA.

Lens system	Microscope objective	Total magnification	FoV (H × V, mm^2)	Max theoretical resolution (µm)
Low Mag branch (0.4×)	20×	5×	2.4 × 1.9	> 1.2
High Mag branch (2.5×)	20×	30×	0.4 × 0.2	1.2

Table 8. Estimated specifications for the commercially available OAV system. Values calculated for white light illumination.

Sample illumination

The sample will be illuminated from upstream and downstream, with a fixed and a retractable LED lamp systems, respectively.

Front light could be coaxial illumination, applied through the OAV system, or be based on a couple of diodes/illumination ring installed around the microscope objective.

Back light will be composed of a diode as light source, mounted on a tube with a lens to focus the light on the sample (~1.5 mm spot size). This will be installed normal to the beam path, and a 45º mirror will be used to direct the light to the sample.

Use of blue light illumination and a monochromatic camera for the high magnification branch is also considered. This could allow theoretical maximum resolutions of down to 0.4 µm.

7.4 Detector

Lower energy threshold

The recommended lower energy thresholds for current hybrid pixel-array detectors is ~3 keV, thus also limiting the usable energy range ≥6 keV. However, some detectors allow to further lower the energy threshold down to 2.3 keV, effectively pushing the lower energy limit for the detector to 4.5 keV. Figure 24 shows the effect of using such lower threshold on the reduction of pixel dead area when working with beam energies below 5.5 keV.

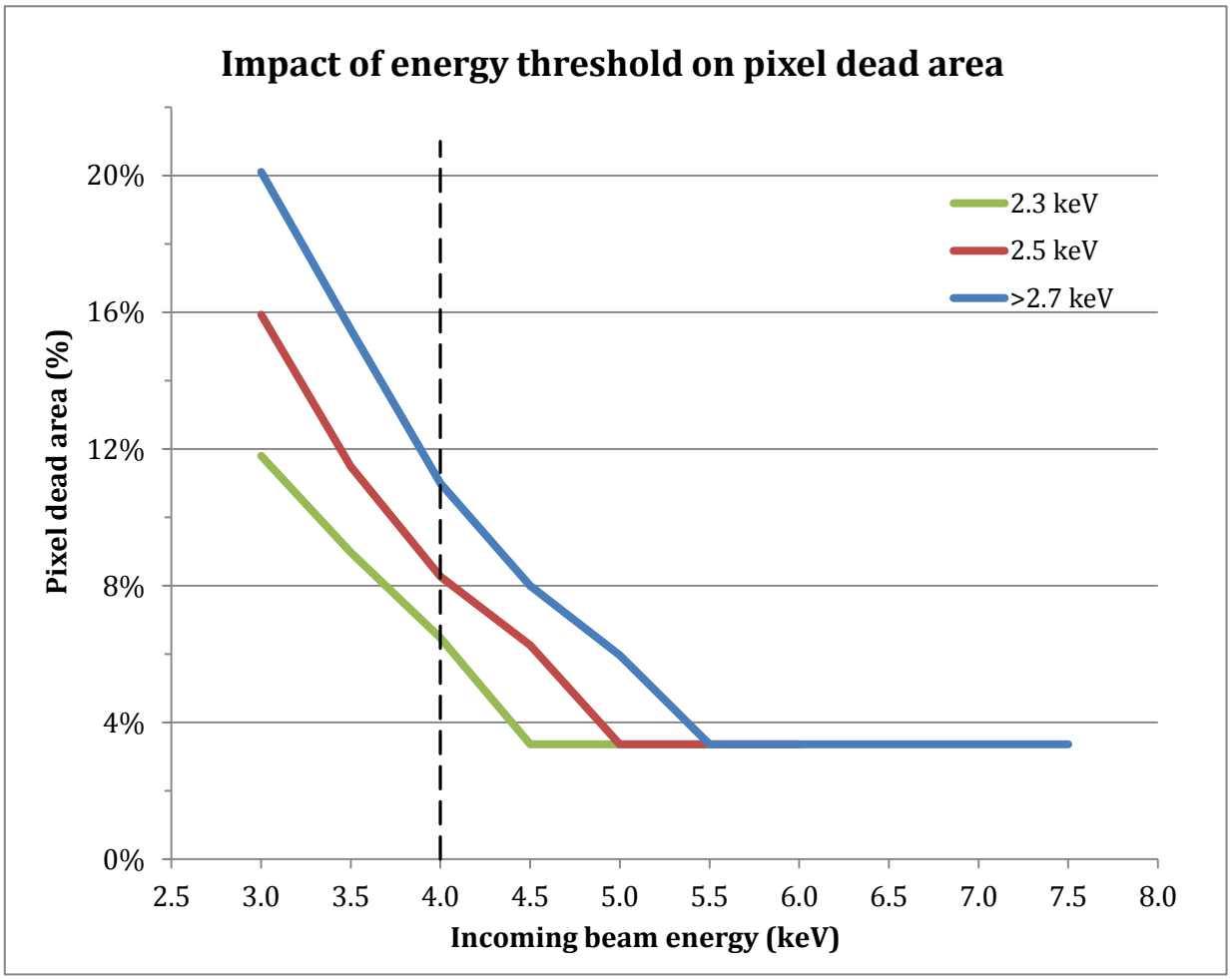

Figure 24. Effective area on an photon counting detector pixel at different beam energies, in function of the defined energy threshold. The lower limit of the foreseen energy range for XAIRA (4.0 keV) is indicated with a dashed line.

Maximum frame rates

The advent of hybrid photon counting X-ray detectors has pathed the way for the establishment of shutterless ultrafine φ-slicing data collection as the current standard in MX beamlines [35], in which large data sets (>1000 frames) are collected in less than 1 minute.

Pushed by the XFEL developments, current detectors are now capable of frame rates high enough to be used in time-resolved experiments, that is, investigating dynamic processes on fast time scales (in the range of milliseconds to seconds), even with synchrotron sources [36].

There is, though, a limitation on the maximum frame rate that can be used for an MX experiment: a certain amount of photons need to be registered in each frame, in order for the indexing software to be able to process it successfully. The limits are considered to be either an average of 1 photon/pixel/frame (J. Holton 2017, ccp4b mailing list) or a minimum of 10^9 photons/frame (B. Doak, 2018, personal communication). Table 9 highlights the maximum practical frame rates that could be used with the envisaged XAIRA flux. According to calculations shown in Table 9, the flux obtained when using the channel-cut monochromator will only allow operating the detector at ~100 Hz, while higher frame rates (up to ~1000 Hz) could be performed using the multilayer monochromator. Thus, equipping the beamline with a detector capable of exposure times in the order of few milliseconds would in principle make time-resolved experiments feasible at XAIRA.

					CCM v		ML v	
Delivered flux	(ph/s)	**1.00E+10**	**1.00E+11**	**1.00E+12**	**3.50E+12**	**1.00E+13**	**3.50E+13**	**1.00E+14**
Flux @ sample	(ph/s)	8.00E+09	8.00E+10	8.00E+11	2.80E+12	8.00E+12	2.80E+13	8.00E+13
Scattered "flux"	(ph/s)	4.80E+08	4.80E+09	4.80E+10	1.68E+11	4.80E+11	1.68E+12	4.80E+12
@ 12.5 Hz	(ph/fr)	3.84E+07	3.84E+08	3.84E+09	1.34E+10	3.84E+10	1.34E+11	3.84E+11
@ 100 Hz	(ph/fr)	4.80E+06	4.80E+07	4.80E+08	1.68E+09	4.80E+09	1.68E+10	4.80E+10
@ 130 Hz	(ph/fr)	3.69E+06	3.69E+07	3.69E+08	1.29E+09	3.69E+09	1.29E+10	3.69E+10
@ 230Hz	(ph/fr)	2.09E+06	2.09E+07	2.09E+08	7.30E+08	2.09E+09	7.30E+09	2.09E+10
@ 400 Hz	(ph/fr)	1.20E+06	1.20E+07	1.20E+08	4.20E+08	1.20E+09	4.20E+09	1.20E+10
@ 500 Hz	(ph/fr)	9.60E+05	9.60E+06	9.60E+07	3.36E+08	9.60E+08	3.36E+09	9.60E+09
@ 550 Hz	(ph/fr)	8.73E+05	8.73E+06	8.73E+07	3.05E+08	8.73E+08	3.05E+09	8.73E+09
@ 750 Hz	(ph/fr)	6.40E+05	6.40E+06	6.40E+07	2.24E+08	6.40E+08	2.24E+09	6.40E+09
@ 1130 Hz	(ph/fr)	4.25E+05	4.25E+06	4.25E+07	1.49E+08	4.25E+08	1.49E+09	4.25E+09
@ 2000 Hz	(ph/fr)	2.40E+05	2.40E+06	2.40E+07	8.40E+07	2.40E+08	8.40E+08	2.40E+09

Table 9. Maximum usable frame rates. For a particular delivered flux (first row), the photons reaching the sample every second (second row) and being diffracted (third row) were calculated. Based on that, the number of photons recorded in each frame is shown for several frame rates. For a frame to be successfully indexable it has to contain at least ~10^9 photons (Bruce Doak 2018, personal communication). Scenarios falling below the ~10^9 ph/fr threshold are highlighted in red. The expected photon fluxes obtained when using the Si(111) channel cut monochromator (CCM) and the Mo/B_4C multilayer monochromator (ML) are indicated.

The table assumes that 80% of the delivered photons arrive to the sample crystal (after absorption due to after XBPM, vacuum window, sample environment, sample holder, ...). Coherent scattering represents only ~8% (@15keV) or ~4.5% (@10keV) of the interactions with the sample (given a crystal of sizes in the micrometer range). An average value of 6% (corresponding to ~12 keV) was considered for the calculations in this table.

Required customised modifications

Depending on the detector chosen for XAIRA, some modifications might be required on the standard model to allow a better integration in the designed End Station:

1) The plastic frame holding the Mylar foil may need to be modified, reducing its depth, to gain some room and prevent clashes with the diffractometer when setting the sample-to-detector distance to the minimum limit (defined as 70 mm in section 5.7).

2) In principle, a detector suitable for vacuum environment should also be able to operate within a helium atmosphere. The only limitation that might need to be taken into account in that sense is that the power supply is not compatible with the helium atmosphere and should be placed outside the chamber.

3) Upon special request, detectors might be calibrated to cover a lower range of energies, so that the lower energy threshold can be set to 2.3 keV (instead of the standard 2.7 - 3.0 keV). This would allow data collection at energies as low as 4.6 keV while still setting an energy threshold at 50% of the incoming beam. Moreover, in practice, collecting at 4.0 keV with a 2.3 keV threshold (i.e. 58% of incoming beam energy), would involve only an additional 3% reduction of the pixel effective area (Figure 24).

7.5 XBPM-based beam-alignment strategy

Error budget simulations (section 10, Appendix I) stablish that the uncertainties in the beam spot size and position on the sample plane derived from uncertainty of the physical degrees of freedom of the beamline optical elements can be reduced by estimating spot position and spot focusing with the feedback from two XBPM detectors.

However, to bring these errors into acceptable levels (i.e. smaller than the actual beam size), the XBPMs have to be combined together with interferometers, which can determine the pitch and position errors of the VFM and HFM mirrors and of the XBPM themselves.

Precise estimation of the beam position will then allow undertaking the necessary corrective actions in case of misalignment (i.e. move the sample, or realign the optics).

XBPM positions

The positions for the two XBPM detectors are defined in Table 10:

	post HSS	**pre OAV**	**sample**
Position (reference)	400 mm downstream from HSS	200 mm upstream from sample	-
Distance from source (mm)	22733	34133	34333
Beam size (H × V, μm²)	398 × 464	720 × 72	3 × 1
Beam excursion (μm)	1100	172	59

Table 10. Beam parameters at XBPM positions. Beam excursion refers to the change of the beam height in the whole energy range 4-14 keV due to the channel-cut monochromator.

Further studies are required to assess if the first XBPM, which is furthest from the sample, could be waived without affecting the overall precision of the referencing system.

Use of interferometers

A total of 10 interferometers will be used for the beam alignment system.

- To account for the beam deviations caused by the non-optimized positioning of the mirrors, a set of 3 interferometers will be installed in both the VFM and HFM mirrors, normal to the mirror surface. Readout from these interferometers will allow determination of pitch and position errors of each mirror. This information could not be obtained using the encoder readings.

- 2 more interferometers are required for each XBPM detector, to determine with precision their horizontal and vertical positions.

A further interferometer monitoring the horizontal positioning of the Horizontal Secondary Source Slit might also be needed. Further studies are required and will be discussed in the PDR stage of the project.

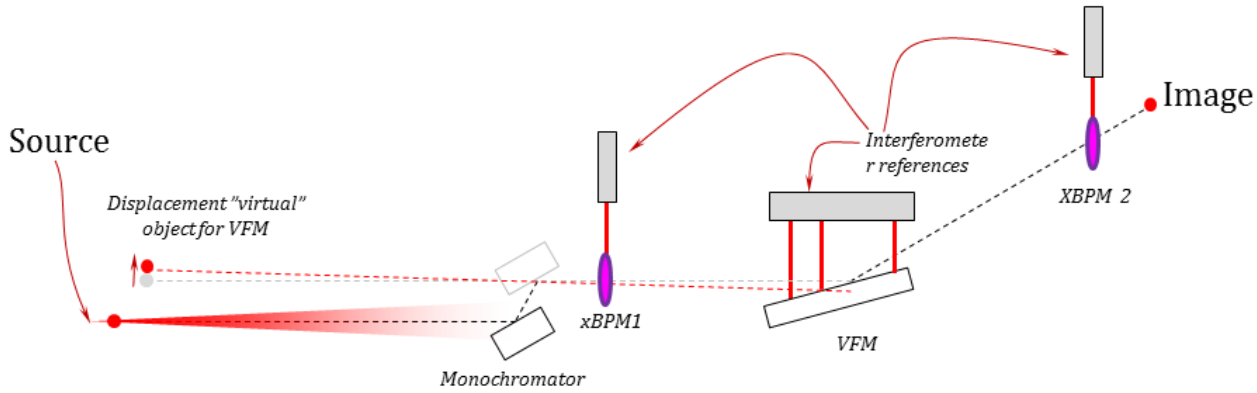

Figure 25. Use of interferometers for beam alignment strategy. Side view scheme of the XAIRA optics, indicating the XBPMs (pink ellipsoids) and interferometers (red lines) used in the vertical plane. An analogue set up would be used for the HFM in the horizontal plane.

Beam position monitors

Several 4-quadrant beam position monitors are under consideration, including commercially available diamond detectors and ALBA-designed silicon-based diodes.

Sample alignment

Samples brought by users to the beamline to be analysed using the diffractometer will be mounted pins glued to standard magnetic bases. The precise position of each sample with respect to the magnetic base can vary enormously (i.e. in an area of ~1.5 mm diameter) between individual samples, even between samples from the same user. Therefore, alignment of the sample with the beam axis cannot be done taking as a reference the position of the sample stages nor the sample pin base.

Referencing of the sample position respect to the beam spot position has thus to be mediated by the OAV system image: the beam position on the sample plane will be determined on the OAV image, and this will be used as reference to position the sample on the beam spot. Fidusialisation of the highest resolution configuration of the OAV (i.e. the high resolution microscope objective) will thus be required. This could be achieved with the use of 2 (additional) interferometers.

7.6 Beamstop

To protect the detector from the direct beam, not scattered and transmitted through the sample, an encapsulating beamstop will be used.

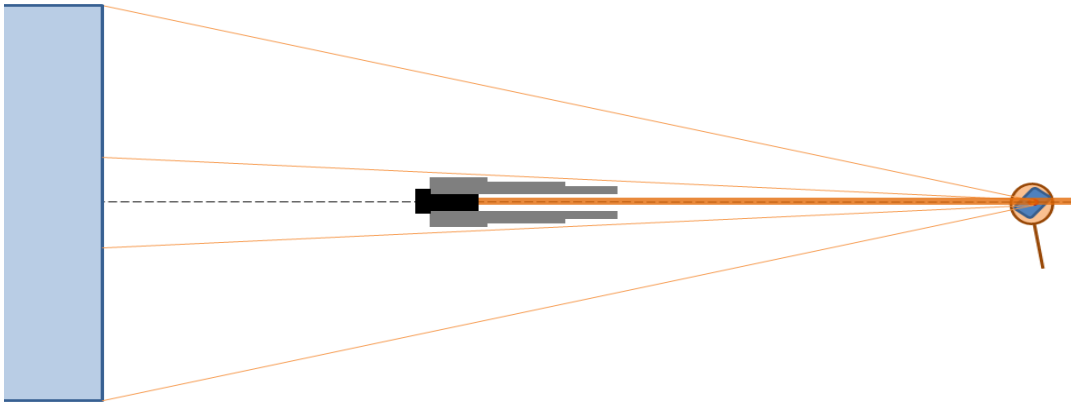

Figure 26. Scheme of beamstop capillary encapsulating the direct beam.

In this element, the direct beam is fully enclosed by a metal capillary (as described in [37] and summarised in Figure 26), designed so that the beam is blocked with a solid absorber the end of the capillary while X-ray photons scattered by air within the capillary are absorbed by the capillary walls (and thus do not contribute to the detector background noise).

To reduce the shadowed part of the Ewald sphere in the diffraction patterns, the beamstop will be supported vertically, collinear to the oscillation axis (omega). The support of the beamstop will be held from above, and will also hold the collimator.

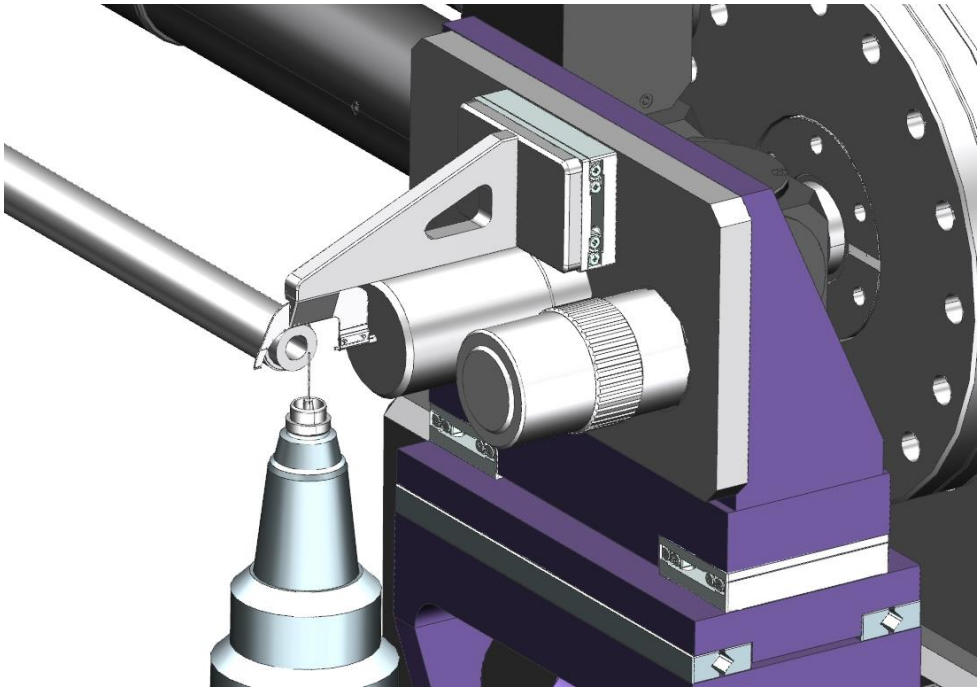

Figure 27. Integration of the beamstop and the collimator.

7.7 Beam conditioning elements

A series of elements will also be installed at the End Station to adapt the characteristics of the X-ray beam to the actual sample and type of experiment.

Apertures

Two sets of apertures will be used to cleanup the beam from stray light and help define the divergence of the beam. Both sets will be composed by two pairs of moveable silicon carbide slits defining a horizontal and a vertical gap. One set will be located upstream the KB vessel, at the beam entry to the EH; the second set will be downstream the KB, close to the diamond window.

Attenuators

To control the intensity of the monochromatic beam, a set of foils of different materials and thicknesses is used; each of these foils can be inserted independently into the beam path, so that they can be combined. For XAIRA, 8 independent foils will be used (yielding 256 possible combinations). The combination of foils required to achieve a given beam transmission will be previously calculated and defined in a table, to be used as input for the control of this element.

The attenuators will be positioned just upstream the KB vessel, to save room between the mirrors and the sample position.

Fast shutter

To block the X-ray beam when it needs to be prevented from reaching the sample environment, a piezo system-based fast shutter will be installed downstream the KB vessel. This position was chosen so that the beam coming out of the KB mirrors could be characterised using the intensity diode and the fluorescent screen (FSM3) without irradiating the sample. The fast shutter will work as normally open (i.e., the element remains open for the beam to pass when no current is applied).

Several commercial options have been identified that have slit edges with openings compatible with the size of the beam envelope at the position of this element, which is of ~1.0 × 0.3 mm^2 (H × V).

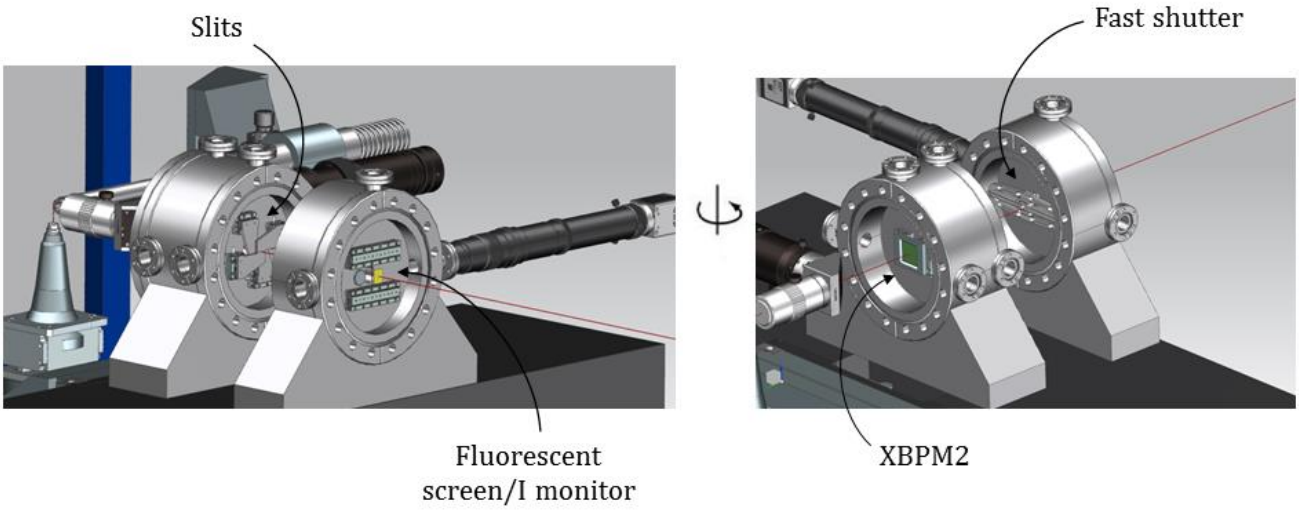

Figure 28. Integration of beam conditioning and monitoring elements located between the KB vessel and the diamond vacuum window. Following the beam path direction, there is a fluorescent screen with an intensity monitor; a fast shutter; apertures; and a XBPM detector.

Diamond window

A circular diamond window will maintain the vacuum-helium interface. This window will have a thickness 5 µm and a free aperture diameter of 2 mm, large enough to allow the beam envelope (~0.6 × 0.2 mm^2 at this position) to pass fully unblocked, without need for any movement of this element.

Collimator

To clean up any scattered radiation generated when the beam interacts with the diamond window or the downstream atmosphere atoms, a collimator will be placed just upstream the sample position. The collimator is composed by a ~10 mm long and narrow metallic tube with a constriction at the downstream end and a thicker back-scatter guard on the upstream end. Given a beam size of ~70 × 7 μm^2 (H × V, with beam focused at sample) at the upstream end of the tube and ~36 x 4 μm^2 at the downstream end, an internal diameter of ~150 µm at the downstream end constriction would be required. The scatter guard will need to be as wide in diameter as required to block any beam scattered from the collimator downstream end that could reach the detector. A pool of several manually-interchangeable collimators with different internal diameters can be envisaged to better adapt to the needs of experiments with specific requirements such as large defocus.

8 Electronics and controls

8.1 Motion control

8.2 Goniometer motion control

The goniometer of the ω axis is the only motor moving during oscillation method diffraction experiments. As the samples and the beam are in the 1 μm size range, the motion characteristics, in particular speed and position control are of paramount importance.

The proposed scheme of the low-level motion control is sketched in Figure 29. This scheme is similar to that used in other beamlines with similar characteristics and fulfills the different requirements from the foreseen data collection strategies.

The motion control must be compatible with a maximum sampling speed of 10 MHz. This is required to collect data at 360 deg/s, at a detector frame rate of 500Hz and closing the loop 50 cycles per image. Note that the uniform speed of the goniometer is required in the oscillation method, and thus the position has to be monitored and corrected many cycles per image.

The rotation must be synchronized with many other motions and elements in the end station:

- The centering stages on top of the ω axis for helical data collections
- The same centering stages for the synchronous correction of the sphere of confusion of the ω axis. The synchronous correction of the centering stages should be done at around 10 Hz.
- The trigger of the detector and the fast shutter.

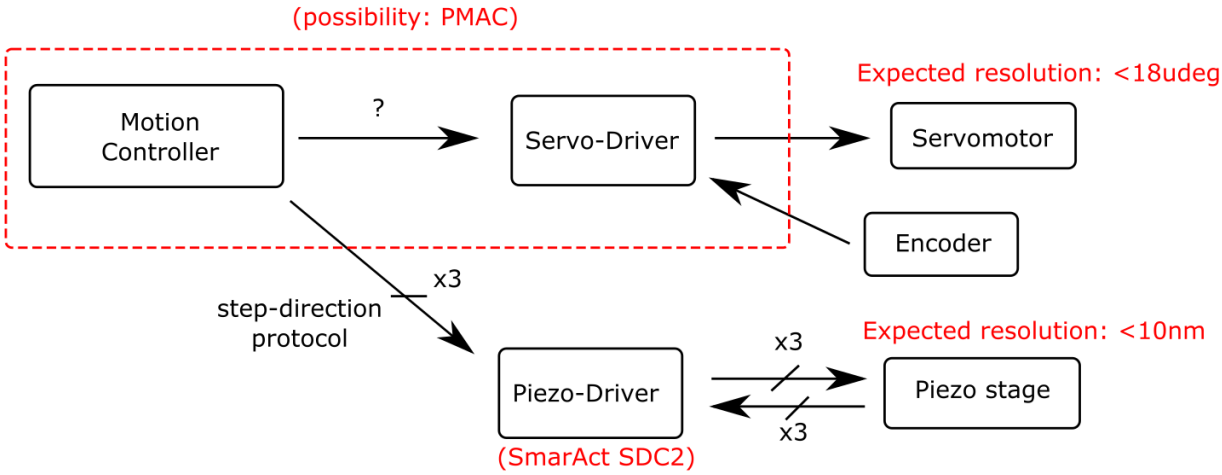

Figure 29. A possible scheme for the motion control of the goniometer.

9 Possible upgrades

The upgrades presented below are not included in the current project of the XAIRA beamline. The list is not exhaustive and is merely illustrative of the future upgrades that the beamline might undergo after start of operation.

9.1 Phase contrast sample imaging

Phase-contrast X-ray imaging has been recently implemented in some MX beamlines (e.g. P14 beamline at PETRA III, I04 beamline at Diamond Light Source) for full-field visualization of the crystals mounts. This imaging method requires additional elements in the optics system to be defocus the beam at the sample position to illuminate the whole area of interest (at least 0.5 × 0.5 mm^2) to avoid rastering or image stitching. Ideally this additional optics should be placed in the beam path without having to adjust the optical elements required for the experiments. Two optical systems can in principle fulfill this requirement

Transfocators

Insertable transfocators consisting in series of compound refractive lenses (CRLs) can in principle defocus the beam without changing the beam path. However, the large beam expansion required (from 1 μm to ~500 μm) implies the use of several hundred lenses, either whether the lenses are located before or after the KB mirrors. The use of transfocators is therefore prevented due to geometrical constraints and the limited transmission of the beam at the long wavelengths.

Mirror defocusing system

Two reflecting mirrors placed after the horizontal secondary source slits (in the optical hutch) can be used to change the object point of the KB mirrors and produce a defocused beam at sample position. Here we illustrate this approach with a system which yields a wider beam at sample position. We note that the illustrated system is not optimized and the values should be further studied before implementation.

The example system includes two mirrors, the vertical defocusing mirror (VDM) and the horizontal defocusing mirror (HDM), as sketched in Figure 30. The parameters of both mirrors are listed in Table 11.

The mirror system can be placed and removed from the beam path vertically, so that the same movement can cope with the height changes due to the monochromator upon the energy. When the defocusing mirrors are inserted in the path, the beam moves vertically by ~1 mm. This variation in height can be coped by the length of the vertical mirror of the KB system downstream. The length of the mirrors is reduced by the high incidence angle, as shown in the footprints of the beam (Figure 31).

However, the resulting spot size at sample position of 70 × 86 μm^2 (H × V, FWHM, Figure 32) is not large enough to cover a whole sample mount, and stitching would be required to have the image of the whole sample holder. More studies would be necessary to assess the applicability of this method in XAIRA, including other mirror configurations.

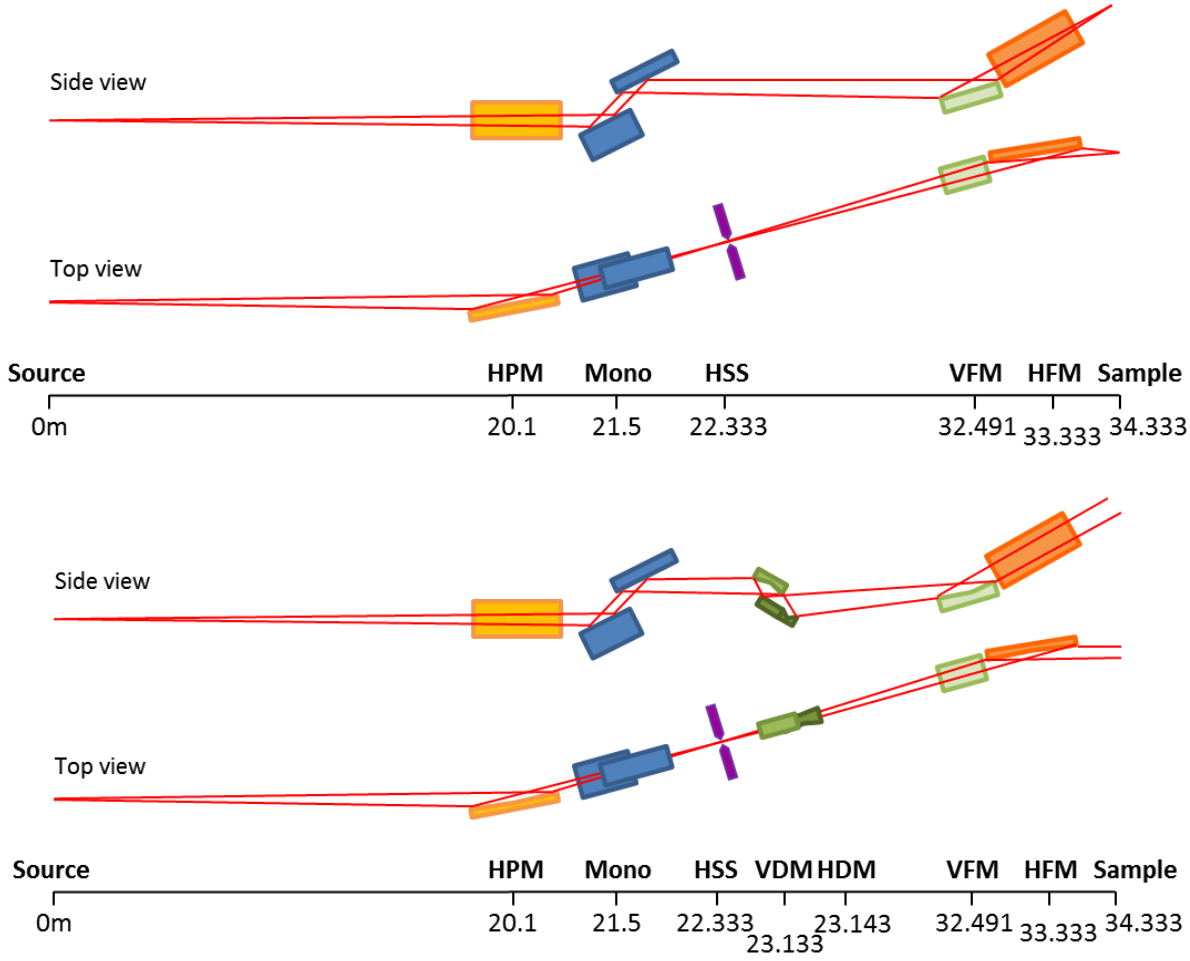

Figure 30. Scheme of the XAIRA optics (top) and the XAIRA optics with the mirror defocusing system with the vertical defocusing mirror, VDM, and the horizontal focusing mirror, HDM (bottom).

	Vertical defocusing mirror (VDM)	**Horizontal defocusing mirror (HDM)**
Focusing	Meridional	Sagittal
Radius (merid/sagit)	1829 m	13 mm
Total optical length	120 mm	120 mm
Spot at sample	86 μm	70 μm
Spot 300mm after sample	88 μm	311 μm
Coating	Ir	Ir
Incidence angle	6.5 mrad	
Vertical deflection	1.3 mm	

Table 11. Values of the main parameters of the VDM and the HDM mirrors. The values indicated are illustrative and are not optimized.

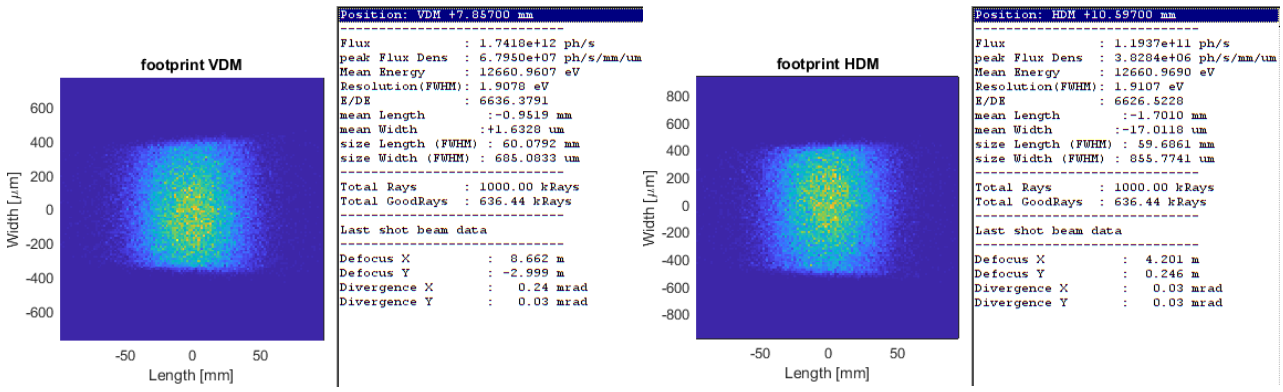

Figure 31. Beam footprints at the VDM and the HDM mirrors.

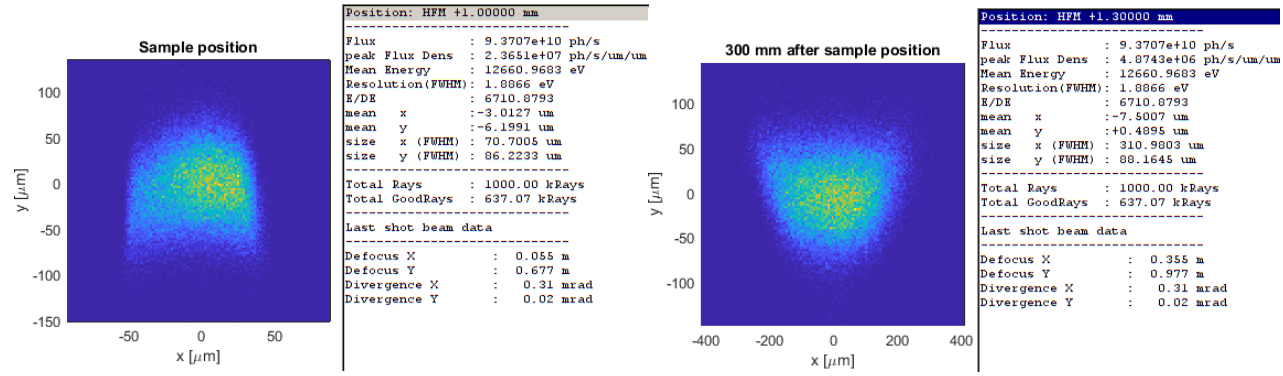

Figure 32. Beam spot at sample position and 300 mm after sample position.

9.2 Time-resolved X-ray crystallography

Microcrystals reduced volume facilitates their use in time-resolved structural studies, as they allow a uniform initiation of enzymatic reactions along the whole crystal volume in a fast time lapse. Together with the foreseen capabilities of XAIRA beamline, time-resolved studies could be performed to obtain structural data in biologically-relevant reaction time-scales, which are on the order of milliseconds to seconds or even minutes.

For this, two (complementary) strategies could be implemented with minor modifications on the current design:

- Femtosecond pump-laser source

Installation of a fs-laser source, operating at a frequency of 1 kHz, is feasible with minor hardware modifications. This will allow sample excitation with wavelengths in the range of

300 to 800 nm, which can be used to either directly initiate a biochemical reaction or trigger the cleavage of a photocaged substrate.

Excitation of protein crystals mounted on a SSX chip with a focused laser beam, paths the way for shutterless hit-and-return (HARE) data collection [38]. The benefit of such strategy is that it does not require the use of a pulsed X-ray beam, but rather takes advantage of the high speed of the translation stages and the fast electronic shutter of the detector (in the µs range or better) to circumvent the lack of a fast X-ray shutter. Using this method, reaction intermediate structures have been captured with time-points ranging from 30 ms to 2 s.

- Piezo-driven droplet injector nozzle for in situ mixing

A piezo-driven droplet injector nozzle will be installed, which is able to deliver picoliter-sized droplets onto protein crystals mounted on a SSX chip. Given the small sizes of both the microcrystals and the liquid drop, mixing occurs in the range of µs to ms, and any ligands contained in the droplet can readily access the molecules in the crystal.

Data collection is then be performed by serial crystallography, following the LAMA strategy (*Liquid Application Method for time-resolved Analyses*), as recently developed at P14 beamline at the PETRA III synchrotron [39], in which protein structures are determined at different times after mixing. Using this method, reaction intermediate structures have been captured with 15 ms time-points.

9.3 Diverse sample presentation formats for Serial crystallography

Given the rise of serial crystallography techniques, XAIRA End Station should be prepared to accommodate the required equipment for other sample delivery methods (Figure 2), on top of the fixed-target chips already included in this CDR.

In particular, a crystal extractor system [40], able to deliver microcrystals in native crystallization solutions, could be compatible with the helium enclosure and could be fitted in the ES without major upgrades.

Other options to be considered for future installation are an ultrasonic acoustic levitator for droplet ejection [41]–[43] and a conveyor belt [42].

10 Appendix I: Beam stability feedback at XAIRA

In this appendix we study the strategy to stabilize the beam at the sample position of the XAIRA beamline, providing the feedback of the two xBPMs considered for the beam.

The optical layout of the beamline is given in the following sketch:

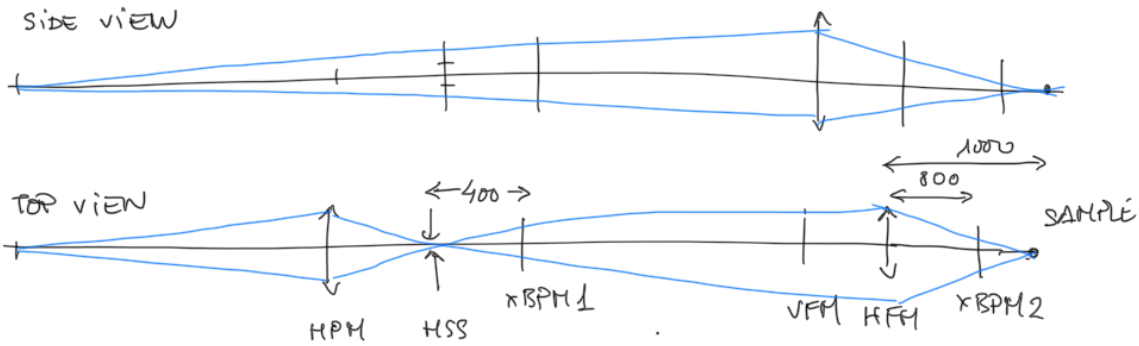

10.1 Error response matrix

The study starts by determining how all the possible degrees of freedom of all the optical elements of the beamline, affect the position of the x-ray beam at the sample plane and at the BPMs. This is done by ray-tracing, using a script on ART [1]. The study is limited to linear dependences, and has been computed by scanning misalignments in a small range (20 µm, 20 µrad) around the nominal position for each degree of freedom.

The results are given in matrix form, as follows:

$$\begin{bmatrix} \Delta x_{sam} \\ \Delta zx_{sam} \\ \Delta x_{bpm1} \\ \Delta x_{bpm2} \\ \Delta y_{sam} \\ \Delta zy_{sam} \\ \Delta y_{bpm1} \\ \Delta y_{bpm2} \end{bmatrix} = \mathbf{M}_{OE} \begin{bmatrix} \Delta Pitch \\ \Delta Roll \\ \Delta Yaw \\ \Delta Z \\ \Delta Y \\ \Delta X \end{bmatrix}_{OE}$$

The variables correspond to the x, y positions at the sample plane, and at the xBPMs. The variables Δzx_{sam} and Δzy_{sam}account for defocusing, and correspond to the distance to the vertical or horizontal focus from the sample position.

$\mathbf{M}_{OE}$ has been calculated for the different optical elements (OE). The resulting matrices are given in the following tables.

$\mathbf{M}_{HPM}$						
	PITCH	*ROLL*	*YAW*	*Z*	*Y*	*X*
Δx_{sam}	0.02	0.00	0.00	0.00	0.00	0.01
Δzx_{sam}	-5.90	-0.01	-0.02	-0.11	0.06	-1.32
Δx_{bpm1}	-1.76	-0.02	-0.01	-0.02	0.02	-0.58
Δx_{bpm2}	1.74	-0.02	-0.01	-0.06	-0.01	0.45
Δy_{sam}	0.00	0.01	0.00	0.00	0.00	0.00
$\Delta \mathrm{z}y_{sam}$	-1.19	-2.39	-0.08	0.05	0.18	-0.43
Δy_{bpm1}	0.01	0.04	0.00	-0.01	0.00	0.00
Δy_{bpm2}	0.01	0.01	0.00	0.00	0.00	0.00

$\mathbf{M}_{X1}$						
	PITCH	*ROLL*	*YAW*	*Z*	*Y*	*X*
Δx_{sam}	0.00	0.00	0.00	0.00	0.00	0.00
Δzx_{sam}	0.00	0.39	-0.06	0.06	-0.07	-0.02
Δx_{bpm1}	-0.02	0.03	-0.01	0.00	0.00	0.01
Δx_{bpm2}	-0.04	-0.12	0.06	-0.05	-0.01	-0.03
Δy_{sam}	-2.44	0.00	0.00	0.02	-0.11	0.00
$\Delta \mathrm{z}y_{sam}$	565.6	-0.49	0.30	-4.41	25.76	0.19
Δy_{bpm1}	-8.21	0.01	0.01	0.31	-1.93	0.01
Δy_{bpm2}	-2.91	0.00	0.00	-0.02	0.11	0.00

$\mathbf{M}_{X2}$						
	PITCH	*ROLL*	*YAW*	*Z*	*Y*	*X*
Δx_{sam}	0.00	0.00	0.00	0.00	0.00	0.00
$\Delta z x_{sam}$	0.02	-0.35	-0.02	0.08	0.03	0.07
Δx_{bpm1}	0.02	-0.04	0.02	0.00	0.01	0.01
Δx_{bpm2}	-0.04	0.15	-0.10	0.03	-0.03	-0.06
Δy_{sam}	-2.44	0.00	0.00	0.02	0.11	0.00
$\Delta \mathrm{z} y_{sam}$	566.5	-0.07	-0.12	-3.98	-25.2	-0.15
Δy_{bpm1}	-0.90	0.01	0.00	0.30	1.94	-0.01
Δy_{bpm2}	-4.05	0.00	0.00	-0.02	-0.11	0.00

$\mathbf{M}_{VFM}$						
	PITCH	*ROLL*	*YAW*	*Z*	*Y*	*X*
Δx_{sam}	0.00	0.01	0.00	0.00	0.00	0.00
$\Delta z x_{sam}$	0.02	-1.81	0.00	0.00	0.05	0.01
Δx_{bpm1}	0.01	-0.01	0.00	0.00	0.00	-0.02
Δx_{bpm2}	-0.02	0.00	0.03	0.00	0.04	0.03
Δy_{sam}	-3.68	0.00	0.00	-0.01	0.94	0.00
$\Delta \mathrm{z} y_{sam}$	425.5	-0.12	-0.22	-0.96	12.93	-0.02
Δy_{bpm1}	0.00	0.00	-0.01	-0.01	0.01	-0.01
Δy_{bpm2}	-3.28	0.00	0.00	-0.01	1.06	0.00

$\mathbf{M}_{HFM}$						
	PITCH	*ROLL*	*YAW*	*Z*	*Y*	*X*
Δx_{sam}	1.98	0.00	0.00	-0.01	0.00	0.91
$\Delta z x_{sam}$	-218.7	-0.03	0.04	-0.95	0.00	19.84
Δx_{bpm1}	0.00	0.00	0.01	0.02	0.01	0.02
Δx_{bpm2}	1.60	-0.06	0.02	-0.05	-0.01	0.96
Δy_{sam}	0.00	0.01	0.00	0.00	0.00	0.00
$\Delta \mathrm{z} y_{sam}$	-0.30	0.13	0.23	-0.39	0.26	0.02
Δy_{bpm1}	-0.01	0.01	-0.01	0.00	0.02	0.00
Δy_{bpm2}	0.00	0.01	0.00	0.00	0.00	-0.01

The complete response matrix is 8x30.

10.2 Beam stability

In order to estimate the stability of the beam, we introduce random errors to each positioning degree of freedom of the optical elements, and evaluate the response [2]. The amplitude of the errors is given in the following matrix.

$\mathbf{M}_{HFM}$						
OE	σ_{PITCH}	σ_{ROLL}	σ_{YAW}	σ_Z	σ_Y	σ_X
HPM	10 µrad	10 µrad	10 µrad	10 µm	10 µm	10 µm
$X1$	10 µrad	10 µrad	10 µrad	10 µm	10 µm	10 µm
$X2$	10 µrad	10 µrad	10 µrad	10 µm	10 µm	10 µm
VFM	10 µrad	10 µrad	10 µrad	10 µm	10 µm	10 µm
HFM	10 µrad	10 µrad	10 µrad	10 µm	10 µm	10 µm

These errors are quite large if considered the amplitude of vibrations, but they are quite realistic when considering mid-term and long-term drifts. We have considered just random, non-correlated errors. As a result of these errors, both the spot position and the spot size at the sample plane may vary, as shown below (Figures 10.2.1 to 10.2.3).

The following plot shows the variation of the spot at the sample plane, for 1000 realizations of noise. One can see that the uncertainty in the vertical plane is larger than in the horizontal plane, and in both cases much larger than the estimated spot size.

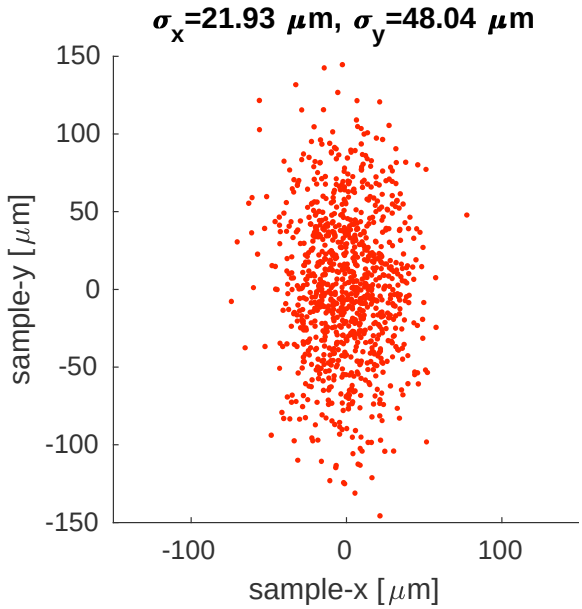

Figure 10.2.1. Uncertainty at the sample position as given by the uncertainty of the physical degrees of freedom of the optical elements of the beamline.

Another result, is that the actual incidence angle on the mirrors changes enough to defocus the beam (even if the ellipses were perfectly stable). The following figures show a histogram of the vertical and horizontal spot size, and the probability to reach a spot size smaller than a given size. The results are poor, and need to be improved.

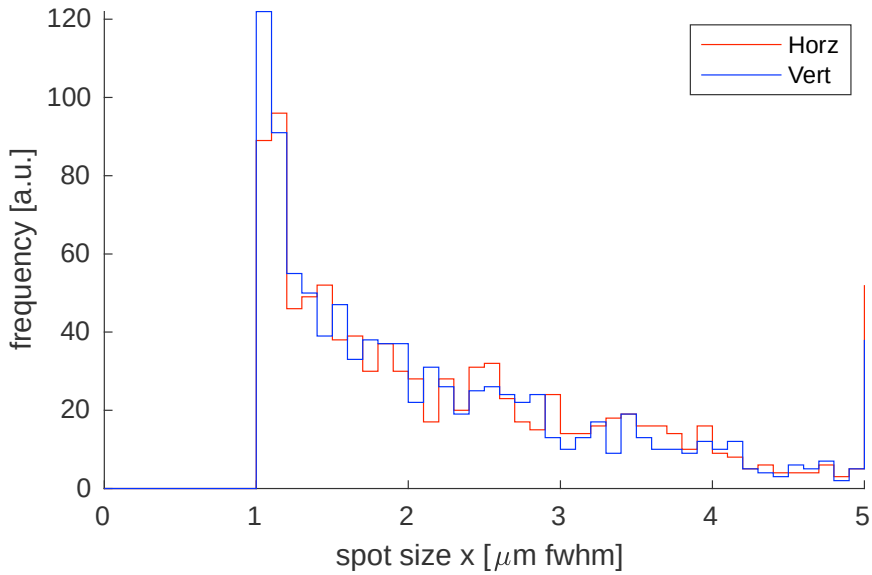

Figure 10.2.2. Histogram of the spot sizes over 1000 stochastic simulations, assuming perfectly stable ellipses and misalignment of the optical elements. The spot size is to be compared to 1 μm, which is the target specification of the focal point.

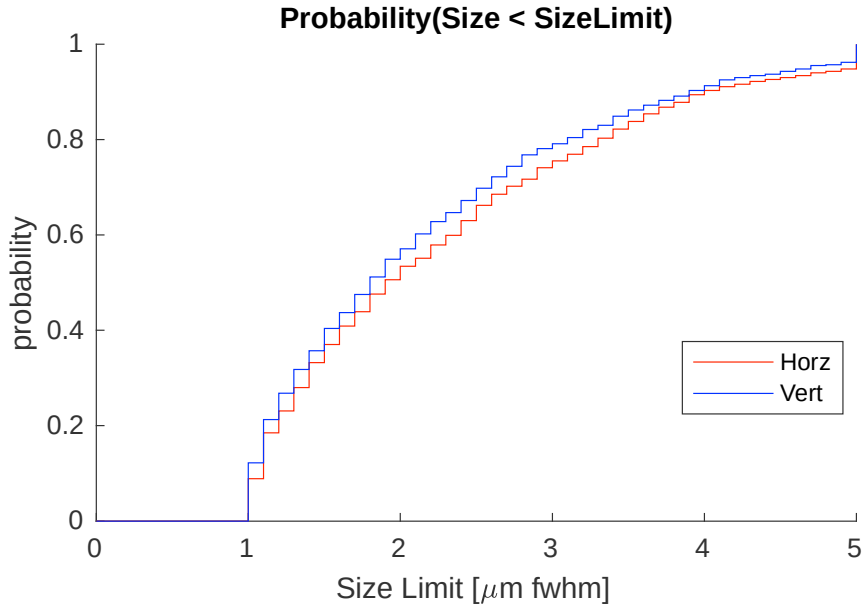

Figure 10.2.3. Probability to obtain a spot size smaller than a given size, as a function of the given size, calculated over misalignment errors of the beamline elements.

10.3 XBPM feedback

The spot position and the spot focusing can be estimated from the readout of the xBPMs. We assume that the *x* position is given by a linear combination of the readout of the xBPMs. To estimate the coefficients, we solve (in the least square sense) the overdetermined system given by the following expression. This is done in script [3]

$$\begin{bmatrix} \Delta x_{sam}[1] \\ \vdots \\ \Delta x_{sam}[N] \end{bmatrix} = \begin{bmatrix} \Delta x_{bpm1}[1] & \Delta x_{bpm2}[1] \\ \vdots & \vdots \\ \Delta x_{bpm1}[N] & \Delta x_{bpm2}[N] \end{bmatrix} \begin{bmatrix} a \\ b \end{bmatrix}$$

Here the indices 1…N correspond to the N realizations of error of the optical elements. Similar expressions are used for the vertical position, and for the defocusing elements.

The coefficients for the obtained fit are given in the following table.

	Independent variable			
Dep. variable	Δx_{bpm1}	Δx_{bpm2}	Δy_{bpm1}	Δx_{bpm2}
Δx_{sam}	1.0997324	1.1354169		
Δzx_{sam}	-87.262654	-90.984213		
Δy_{sam}			0.0057122	0.8060158
Δzy_{sam}			-31.522207	-52.246936

One can see that using the above expressions one can actually estimate the position on sample, and therefore take the necessary corrective action (move the sample, or realign the optics).

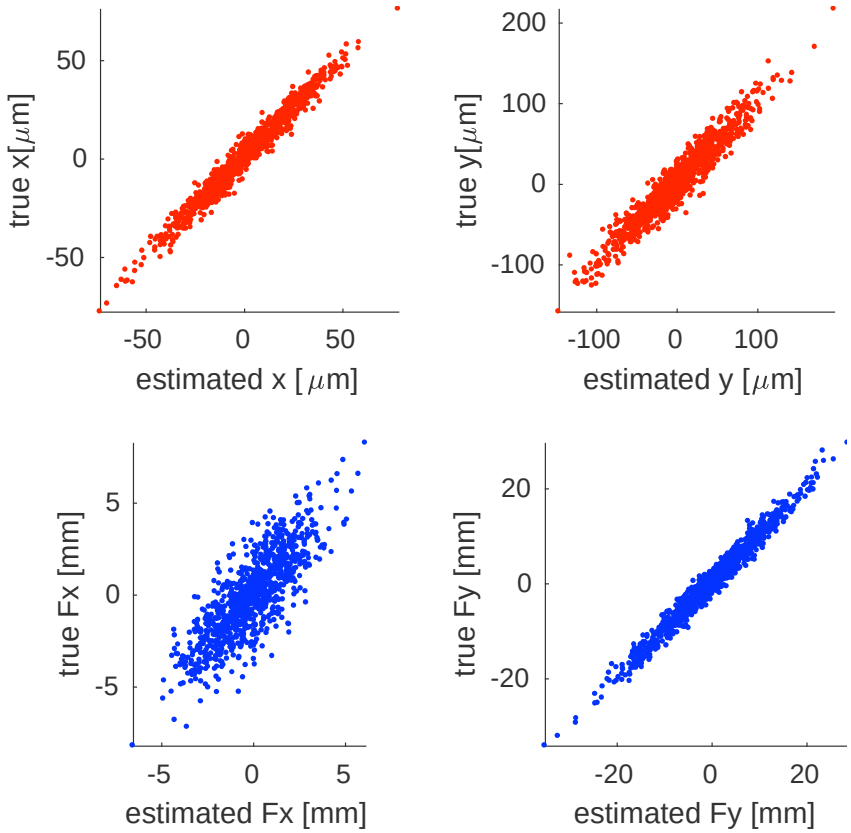

Figure 10.3.1. Scatter plot showing the correlation between the true position of the spot and the position estimated by the xBPMs.

Nevertheless, one can see that the correlation is not perfect, and there is a residual uncertainty on the position, even if the readout of the xBPM was noiseless. The residual errors still lead to uncertainties in position and focus at the sample position larger than the specification values (Figures 10.3.2. and 10.3.3). In conclusion, xBPMs are necessary but are not sufficient to stabilize the beam to the required degree.

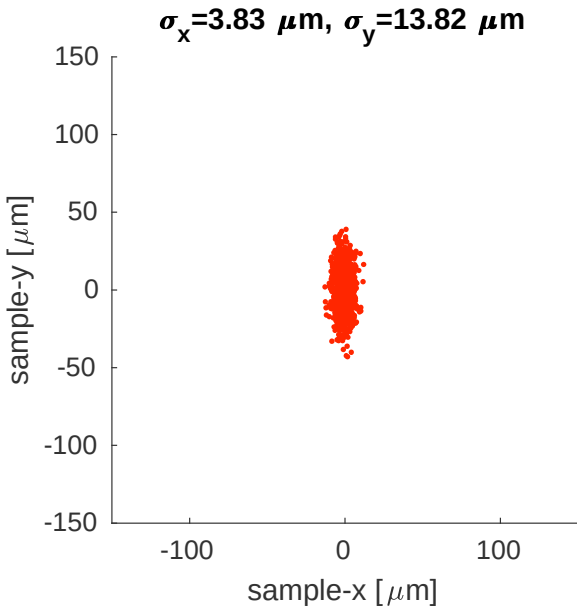

Figure 10.3.2. Residual error in position. A significant improvement is achieved, although the error is still larger than the spot size.

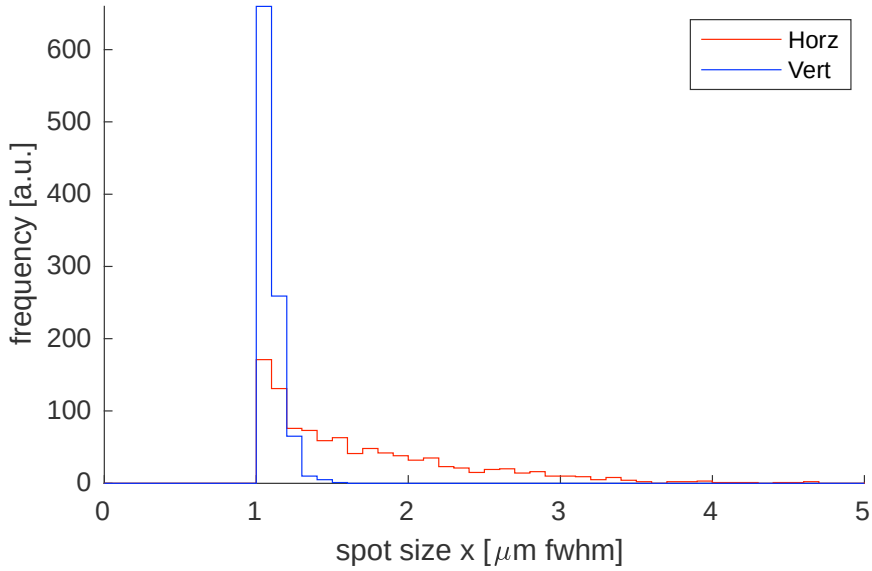

Figure 10.3.3. Histogram of the spot size, assuming perfectly stable ellipses, but residual misalignment errors.

10.4 XBPM and interferometer feedback

Most of the errors are actually provoked by the pitch and position errors of the HFM and VFM. These can be measured directly, by means of interferometers looking directly at the mirror surface. This allows avoiding errors accumulated along the kinematic chain between the encoders and the optical surface, and to avoid errors due to deformations of mechanics [4].

To determine the linear combination of these readouts, we use the same technique as in previous section. The resulting coefficients are given in the following tables:

	Independent variable			
Dep. variable	Δx_{bpm1}	Δx_{bpm2}	ΔP_{HFM}	ΔX_{HFM}
Δx_{sam}	-0.0029735	0.0102462	1.9642390	0.9000420
$\Delta z x_{sam}$	2.2978174	-1.0288738	-217.33535	20.673586

	Independent variable			
Dep. variable	Δx_{bpm1}	Δx_{bpm2}	ΔP_{VFM}	ΔY_{VFM}
Δy_{sam}	0.0907955	0.5822878	-1.7704920	0.3252157
$\Delta z y_{sam}$	-20.987810	-135.31420	-017.90435	156.61489

With that information, the sample position is determined well within the micron, as shown in the residual errors given in the following plot.

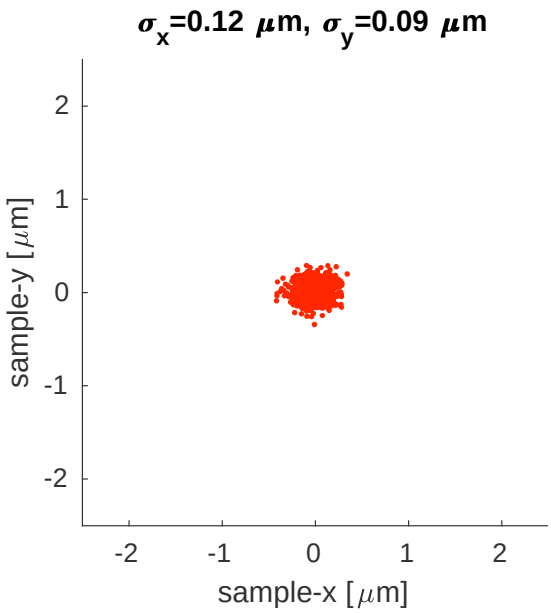

Figure 10.4.1. Residual error in position. A significant improvement is achieved, with the remaining error being smaller than the spot size.

And the focus is also perfectly determined:

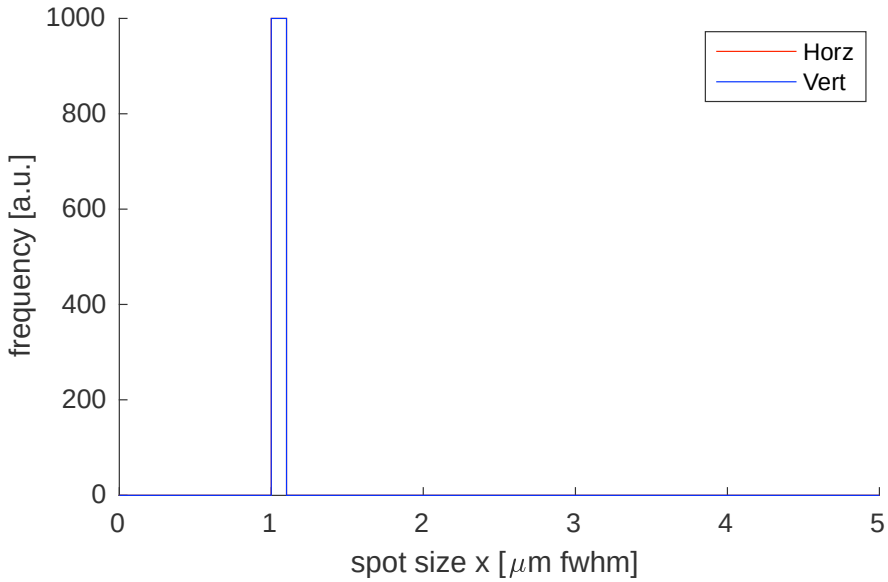

Figure 10.4.2. Histogram of the spot size, assuming perfectly stable ellipses, but residual misalignment errors.

10.5 Error Budget

The analysis does not include at this stage several sources of error that could eventually be accounted:

- Read out errors of the XBPMs
- Positioning of the photon source
- Bending of the mirrors
- Sample positioning
- Fiducialization of the OAV, which may require two more interferometers.
- Short and mid-term stability of the interferometer supports

10.6 Conclusions

The analysis above clearly indicates that the most critical uncertainty comes from the pitch of the mirrors. This can only be achieved by installing precise XBPMs and an interferometer system.

More detailed information to optimize and characterize the positioning system requires the calculation of the different sources of errors to estimate the overall error budget. In particular, the utility of the upstream XBPM must be assessed.

10.7 References

[1] Script *07_Xaira_ART_Misalignments/xairaART_misalignments.m*, results stored at *XairaMatrixModel.xlsx*

[2] script *xaira_MonteCarloErrors_Response.m*

[3] script *xaira_MonteCarloErrors_Feedback_A.m*

[4] script *xaira_MonteCarloErrors_Feedback_B.m*

11 Appendix II: Requirements for actuation and movements of the ES elements

Definition of axes

Axis	Direction	
x	Transversal	Parallel to ground plane, normal to beam axis
y	Longitudinal	Along beam axis
z	Vertical	Normal to ground plane

11.1 Apertures 1

The first element in the EH will be the beam apertures, composed by two pairs of slits that will be used to define the divergence of the beam. Actuation will depend on 4 motors, which will define the gap and offset for both the vertical and horizontal directions.

The size of the beam envelope at the position of these apertures is of ~9.2 × 1.7 mm² (H × V, with beam focused at sample). The apertures should allow total interception of the whole beam, as well as accepting it all even if it is defocused and/or slightly mis-steered.

Apertures	
Actuation	Remotely controlled
Maximum aperture	As specified in Optics CfT
Blade	As specified in Optics CfT
Positioning resolution	As specified in Optics CfT
Positioning accuracy	As specified in Optics CfT
Repeatability	As specified in Optics CfT

11.2 Fluorescence screen monitor 2

To characterise beam shape and position before the KB mirrors, a fluorescent screen monitor will be used. This element is composed by a rectangular Ce-doped YAG screen (20 × 15 mm²) intercepting the beam, with a mirror at 45º to divert the image to an integrated camera to image screen. The whole element will be mounted on a vertical or transversal translation stage, to move it in and out of the beampath. If the beam is badly misaligned and falls out of the screen area, the stage could be used to offset FSM2 (including lens and camera) from the beampath-aligned position, to screen a wider area to locate the beam position. Thus, the stroke of the stage needs to account for a whole width of the screen towards one direction, plus whatever is needed to remove the element from the beampath towards the opposite direction.

Given a beam envelope size of ~9.3 × 1.8 mm² (H × V, with beam focused at sample) and assuming a camera field of view of 18 × 13 mm², it would be preferable to have the element mounted on a transversal stage, in order to extend the range for visualisation of the beam in that direction, in which the margin is smaller.

Transversal translation (x axis)	
Actuation	Remotely controlled
Stroke	+20 mm to “out”
Positioning resolution	0.5 μm
Positioning accuracy	1 μm
Repeatability	1 μm
Speed	n/a

11.3 Attenuators

The size of the beam envelope at the position of this element is of ~9.5 × 1.8 mm² (H × V, with beam focused at sample). The foils should allow total interception of the whole beam. Independent actuation of each foil will be remotely controlled.

When in use, the attenuators will need to be aligned to the beam. Given the sizes of the foils, though, vertical and transversal adjustments of the element will be performed manually, during commissioning. Neither longitudinal translation nor rotations are required for this element.

Vertical and transversal adjustments (x and z axes)	
Vertical and transversal position	Manually adjusted
Actuation	Remotely actuated in/out, independently for each foil

11.4 Vertical and Horizontal Focusing Mirrors

These elements and their movements are described in the beamline Optics documentation.

11.5 Fluorescence screen monitor 3 and Intensity monitor 1

To characterise beam shape, position and flux after the KB mirrors, a fluorescent screen monitor and an intensity monitor will be used. The two elements can be mounted on the same stage, which will allow moving one, the other or none in and out of the beampath.

FSM3 is composed by a circular Ce-doped YAG screen (10 mm diameter) intercepting the beam, with a mirror at 45º to divert the image to an integrated camera to image the screen.

The intensity monitor is a diode (such as, e.g. Hamamatsu S-1223, as successfully used in several beamlines at ALBA).

Similarly to what is defined for FSM2, if the beam is badly misaligned and falls out of the screen area, the motorised stage will be used to offset FSM3 (including lens and camera) from the beampath-aligned position, to screen a wider area to locate the beam position. Thus, the stroke of the stage needs to account for a whole width of the screen, plus whatever is needed to remove both elements (FSM and I diode) from the beampath. This range already includes a position in which the intensity monitor is aligned with the beampath.

Given a beam envelope size of ~1.0 × 0.3 mm² (H × V, with beam focused at sample) and a (circular) visible area of 8 mm diameter, it would be preferable to have the element mounted on a transversal stage, in order to extend the range for visualisation of the beam in that direction, in which the margin is smaller.

Transversal translation (x axis)	
Actuation	Remotely controlled
Stroke	+8 mm to both elements "out"
Positioning resolution	0.5 μm
Positioning accuracy	1 μm
Repeatability	1 μm
Speed	n/a

11.6 Fast shutter

To control the exposure of the sample to the beam, a fast shutter will be installed. This element will be synchronised with the spindle axis ω (around which the sample oscillates during data collection). The synchronisation of the open/close time of the fast shutter with the spindle angle is not so critical when data is collected in shutterless mode (i.e. leaving the shutter open until the end of data collection), a common collection strategy with detectors with very short read-out times, such as hybrid photon counting detectors. In such scenarios, as foreseen for XAIRA, a shutter with closing times better than 5 ms would suffice.

The size of the beam envelope at the position of this element is of ~1.0 × 0.3 mm² (H × V, with beam focused at sample). An opening of 1.5 mm or larger is thus required for the fast shutter.

Ideally, there should be a fast way to bypass this element (in case it breaks down and stays blocking the path, or if larger unfocused beams have to be passed through); this could be accomplished with a hole of ~3 mm diameter in (or close to) the fast shutter mount (an "out" position). This might not be required if the fast shutter works as normally open, allowing for the beam to pass when no current is applied.

The fast shutter will be mounted on a vertical stage, to allow the element to follow the beam excursion (of around 210 μm at this position). If possible and if required, it could also have a stroke large enough to remove the element from the beam path (by aligning a hole on the mount with the beampath).

Fast shutter actuation	
Actuation	Remotely controlled
Open/close time	Ideally <4 ms
Vertical translation (z axis)	
Actuation	Remotely controlled
Stroke	>300 μm (+ stroke needed for "out" position, if possible)
Positioning resolution	1 μm
Positioning accuracy	2 μm
Repeatability	2 μm
Speed	Out in 5 s

11.7 Apertures 2

The beam divergence after the KB mirrors will be defined by using two pairs of slits. Actuation should depend on 4 motors, which will define the gap and offset for both the vertical and transversal directions.

The size of the beam envelope at the position of these apertures is of ~0.8 × 0.3 mm^2 (H × V, with beam focused at sample). The slits should allow total interception of the whole beam, as well as accepting it all even if it is defocused and/or slightly mis-steered.

Apertures	
Actuation	Remotely controlled
Maximum aperture	5 x 5 mm^2
Blade	Knife-edge
Positioning resolution	0.25 µm (gap & offset)
Positioning accuracy	1 µm (gap & offset)
Repeatability	1 µm (gap & offset)
Speed	n/a

11.8 XBPM detector 2

XAIRA beam alignment strategy is based on passing the beam through 2 beam positioning monitors (four-quadrant detectors), which will act as references and define a known path.

The XBPM will be mounted on a vertical stage, to compensate for vertical beam excursion upon energy changes, to scan the whole XBPM active area height and to allow the beam to pass unaffected (by passing it through a ~3 mm diameter hole drilled on the XBPM support, just below to the quadrants).

The size of the beam envelope at the position of this element is of ~720 × 240 μm^2 (H × V, with beam focused at sample).

Vertical translation (z axis)	
Actuation	Remotely controlled
Stroke	Active area ±1.5 mm + distance to hole
Positioning resolution	0.02 µm
Positioning accuracy	similar or better than that of the XBPM (<0.05 µm)
Repeatability	similar or better than that of the XBPM (<0.05 µm)
Speed	Out in 10 s

11.9 Diamond window

The vacuum-helium interface will be maintained by a diamond window. This should be large enough to allow the beam envelope to pass fully unblocked, without need for any movement of this element.

Given a beam envelope size of ~0.6 × 0.2 mm² at this position (H × V, with beam focused at sample), a 2 mm diameter window should suffice.

11.10 Sample visualisation system

The on-axis viewing system (OAV), includes a microscope objective and a prism located in the beam path. The rest of the OAV elements (lens, camera) will be mounted on a tube projected perpendicularly to the beam axis. Both the microscope and the prism will have a ~0.5 mm drill hole to allow for the X-ray beam (of about ~250 × 125 μm² at this position) to cross the OAV unaffected, without losing any flux. Hence, the OAV elements, and their beam path holes, will need to be aligned to the beam axis.

The OAV image will be used to define the sample position (based on the beampath position), thus its stages will require a good resolution (in the order of ~100 nm).

For the longitudinal translation, the OAV will need to move solidarily with the goniometer (which will be moved longitudinally when aligning the sample to an unfocused beam). The resolution of this movement should match 10% of the depth of field of the OAV (estimated to be ~1.6 μm based on a 50X microscope objective specs), in order to have 8-10 steps of the movement within the focal point depth.

Transversal translation (x axis)	
Actuation	Remotely controlled
Stroke	-2 to +2 mm
Positioning resolution	0.1 μm
Positioning accuracy	0. 5 μm
Repeatability	0. 5 μm
Speed	1 mm/s if possible
Longitudinal translation (y axis)	
Actuation	Remotely controlled
Stroke	-4 to +0.1 mm (same as goniometer)
Positioning resolution	0.2 μm or better (ideally 0.1 μm)
Positioning accuracy	0.5 μm or better
Repeatability	0.5 μm or better
Speed	0.5 mm/s
Vertical translation (z axis)	
Actuation	Remotely controlled
Stroke	-2 to +2 mm
Positioning resolution	0.1 μm
Positioning accuracy	0. 5 μm
Repeatability	0. 5 μm
Speed	1 mm/s if possible

The camera will also require an adjustment system to facilitate its alignment with the image. This can be a manual system, as will be only operated during commissioning.

The sample will be illuminated from upstream and downstream. Illumination will be activated remotely. Backlight (downstream) illumination actuation is further detailed in section 11.14.

11.11 Collimator

The collimator will need to be aligned to the beam axis, to allow the beam to pass through it. This requires motorised vertical and transversal translations, with strokes of 4 mm. Yaw and pitch for this element can be manually adjusted and do not need to be motorised.

To avoid clashes when the goniometer is moved longitudinally, the collimator needs to move solidarily with the OAV microscope and the goniometer, with the same stroke and resolution as for these elements.

Transversal translation (x axis)	
Actuation	Remotely controlled
Stroke	-2 to +2 mm (+ retraction?)
Positioning resolution	0.2 µm
Positioning accuracy	0.5 µm
Repeatability	0.5 µm
Speed	1 mm/s if possible
Longitudinal translation (y axis)	
Actuation	Remotely controlled
Stroke	-4 to +0.1 mm (same as goniometer)
Positioning resolution	0.2 µm or better (ideally 0.1 µm)
Positioning accuracy	0.5 µm
Repeatability	0.5 µm
Speed	0.5 mm/s
Vertical translation (z axis)	
Actuation	Remotely controlled
Stroke	-2 to +2 mm (+ retraction?)
Positioning resolution	0.2 µm
Positioning accuracy	0.5 µm
Repeatability	0.5 µm
Speed	1 mm/s if possible
Yaw (along z axis) and pitch (along x axis)	
Actuation	Manually adjusted
Retractile motion	
Actuation	Remotely controlled
Speed	Out in <3 s

Additionally, there should be a longer transversal or vertical movement allowing for the removal of this element.

For data collection at cryogenic temperatures and air atmosphere, and given the proximity to the sample position, collimator might require heating, to prevent ice deposition caused by the cold-stream.

11.12 Diffractometer

The beam size at the sample position is of 3.1 × 0.8 μm² (H × V), with a vertical excursion of 60 μm.

The sample holder will be placed on a vertical axis goniometer, to avoid the effects of gravity sagging and contribute to sample position stability.

During data collection, the sample will be rotated along the ω axis, which lies perpendicular to the beam axis and to the ground. The axis has to be very carefully aligned in the transversal direction to be coplanar with the beam path. The spindle rotation speed has to be adjustable to the experiment needs, ideally with a minimum of 0.1 degree/s or less and a maximum of 1 Hz (360 degrees/s) or more.

This will allow data collection at optimal oscillations for nowadays detectors, defined in [35] as about 1/10 of the mosaicity (approximately 0.02 degrees/frame, which, for frame rates of 100 Hz and 750 Hz, corresponds to 2 and 15 degrees/second, respectively).

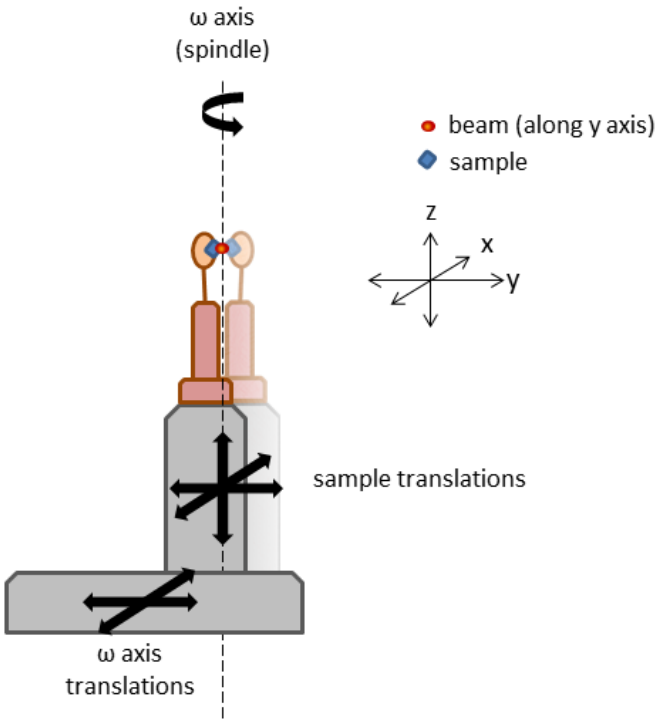

Figure 33. Translations required to adjust the sample position.

The goniometer (ω axis spindle) will require 3 movements:

- A transversal (x) translation will be used to bring the ω axis in plane with the beam axis.
- A longitudinal (y) translation of the ω axis will allow aligning the sample to an unfocused (larger) beam in a fast and reliable way. The stroke of this movement will be from 0 to -4 mm (from the focal point, upstream), together with a ±0.1 mm around the focal point, for adjustment. This translation will also take place solidarily for the OAV and the collimator.
- No vertical (z) translation (this movement will be achieved with the vertical stage mounted on top of the goniometer).

On top of these, 3 additional movements are required for the sample centring stages mounted on the ω axis, these with of shorter strokes but better resolution:

- Transversal and longitudinal translations, for accurate sample alignment with the beam.
- A fast and resolved vertical translation will be used to perform helical data collection and fast raster scans on small areas (x-ray-based sample centring). With a minimum stroke of 10 mm (ideally 20 mm), it will also account for vertical differences in the sample support (e.g. use of capillaries, glass cover slips, …). This stroke will also account for the vertical excursion in the beam position when changing energy (60 µm).

ω axis translations	
Transversal translation (x axis)	
Actuation	Remotely controlled
Stroke	-5 to +5 mm
Positioning resolution	0.1 µm if possible, otherwise less than goniometer runout
Positioning accuracy	0.2 µm if possible
Repeatability	0.2 µm if possible
Speed	0.5 mm/s if possible
Longitudinal translation (y axis)	
Actuation	Remotely controlled
Stroke	-4 to +0.1 mm
Positioning resolution	0.2 µm or better (ideally 0.1 µm)
Positioning accuracy	0.5 µm
Repeatability	0.5 µm
Speed	0.5 mm/s

ω axis rotation (goniometer)	
Actuation	Remotely controlled
Stroke	-360 to +720
Resolution	<0.01 mrad. Ideally, 10^5 steps/deg.
Sphere of confusion	0.1 µm or less
Repeatability	<0.01 mrad
Speed	0.1 deg/s to 180deg/s (ideally up to 360 deg/s)

Sample centring translations	
Perpendicular to ω axis (x and y axes)	
Actuation	Remotely controlled
Stroke	-2 to +2 mm
Positioning resolution	0.01 µm (with microstepping)
Positioning accuracy	0.5 µm
Repeatability	0.5 µm
Speed	1 µm/s to 2.5 mm/s
Vertical translation (z axis)	
Actuation	Remotely controlled
Stroke	-5 to +5 mm
Positioning resolution	0.01 µm (with microstepping)
Positioning accuracy	0.5 µm
Repeatability	0.5 µm
Speed	1 µm/s to 2.5 mm/s

In addition, to allow enough room for the potential use of the beam line for samples with different formats (e.g., serial crystallography ejector jet, …), it would be convenient to have the possibility to (manually) unmount at least the stalk/head of the goniometer (i.e. leaving the spindle motor installed to serve as platform).

11.13 Serial crystallography stages

The requested movements for the SSX stage are:

Transversal and vertical translation (x and z axes)	
Actuation	Remotely controlled
Stroke	50 mm or larger
Positioning resolution	<10 nm if possible
Positioning accuracy	<0.02 µm
Repeatability	<0.02 µm
Speed	As fast as possible (<10 mm/s)
Longitudinal translation (y axis)	
Actuation	Remotely controlled
Stroke	±5 mm
Positioning resolution	<10 nm if possible
Positioning accuracy	<0.02 µm
Repeatability	<0.02 µm
Speed	Fast

11.14 Backlight

The sample visualisation system will include a backlight illumination element. The current design foresees a set of different LED light sources focused on the sample by a lens. When in use, the backlight illumination will be placed downstream the sample, with its focal point aligned to the beampath (thus overlapping with the diffraction cone). Current plans foresee two types of illumination at this position: polychromatic white light and monochromatic short wavelength (blue or UV) light. Changing from one type to the other should also be controlled remotely.

To collect diffraction data, the backlight will need to be retracted to a further location. The backlight should be preferably actuated by motors (this will also make it easier to align it to sample), although this is not a critical requirement and, in case that geometrical constrains lead to possible collisions in some operations, the actuation would then be pneumatically driven so that it can be controlled through EPS.

Independently of the actuation, though, the backlight should also be capable of a remotely-controlled longitudinal translation, so its focal point can be moved to follow the sample when it is moved longitudinally (when sample is placed out of the X-ray beam focus). The stroke of this movement should be comparable to that of the sample (as for the OAV and the collimator).

Retractile motion	
Actuation	Remotely controlled
Stroke	“out” to “beampath”
Positioning resolution	10 µm
Positioning accuracy	20 µm
Repeatability	20 µm
Speed	“In/out” in <5 s, if possible
Longitudinal translation (y axis)	
Actuation	Remotely controlled
Stroke	-6 mm to +2 mm
Positioning resolution	20 µm
Positioning accuracy	50 µm
Repeatability	50 µm
Speed	Ideally, as fast as sample longitudinal translation

11.15 Beamstop

Shortly downstream the sample, the direct (not scattered) beam transmitted through the sample has to be stopped by a so called beamstop, to protect the detector and reduce background noise in the images.

Given a size of the beam envelope at the position of this element is of ~110 × 90 µm² (H × V, with beam focused at sample), the metal capillary should have an inner diameter of at least 0.15 mm.

Alignment of the beamstop to the beam will be done by motorised vertical and transversal translation. To follow the beam position when changing energy, the vertical movement will require a stroke of ±2 mm. Transversal adjustment of the beam stop will require a similar stroke.

A longitudinal movement will also be required for some functionalities, i.e. to reduce the size of the beamstop shadow on screen when very low resolution data is collected, and to maintain a the beampath length as short as possible upon sample longitudinal translations.

To allow the beam to pass further than the beamstop position, to characterise the beam with FSM4 or I diode 2 and to minimise the risk of accidental damage or misalignment of the beamstop in case of manual mounting/manipulation of sample, it would be convenient to include an additional mechanism to retract the beamstop. Alternatively, a longer vertical or transversal stroke could allow the beamstop to travel away from the sample holder. This involves a long stroke, which has to be covered in a short time (<5 s) every time a sample is mounted/unmounted. Hence, additional efforts in the design might be required, as with the ALBA standard stepper motor set up the beamstop retraction would take over 1 minute, which is not acceptable for user operation.

Also, given its proximity to the cryostream flow, whenever data collection is performed at cryogenic temperatures and in air atmosphere, the beamstop might require heating to prevent ice deposition caused by the cold-stream.

Transversal translation (x axis)	
Actuation	Remotely controlled
Stroke	-2 to +2 mm
Positioning resolution	0.1 µm (with microstepping)
Positioning accuracy	0.5 µm in open loop / 0.2 µm in closed loop
Repeatability	0.5 µm in open loop / 0.2 µm in closed loop
Speed	n/a
Longitudinal translation (y axis)	
Actuation	Remotely controlled
Stroke	+10 to +30 mm from sample
Positioning resolution	0.1 µm
Positioning accuracy	0.2 µm
Repeatability	0.2 µm
Speed	5 mm/s
Vertical translation (z axis)	
Actuation	Remotely controlled
Stroke	-2 to +2 mm
Positioning resolution	0.1 µm (with microstepping)
Positioning accuracy	0.5 µm in open loop / 0.2 µm in closed loop
Repeatability	0.5 µm in open loop / 0.2 µm in closed loop
Speed	n/a
Retractile motion	
Actuation	Remotely controlled
Speed	Out in <5 s

11.16 Fluorescence screen monitor 4 and Intensity monitor 2

There will be a diagnostic set downstream the beamstop, which will be used to characterise the shape and flux of the beam close to the sample position. It will be composed of an intensity monitor and a fluorescence screen.

The fluorescent screen (FSM4) will be similar to that of XALOC DISET device placed below the detector, much simpler than the other FSMs used upstream.

The intensity monitor will be a transmissive diode, so that the fluorescence screen can be placed right afterwards, as a single element. Even more, this diagnostic set can also be incorporated on the detector cover (described in section 11.17), if this simplifies the actuation of these elements.

These elements will require a motorised actuation to place them in position, intercepting the beam, and to retract them away when not in use. These elements need to be aligned to the beam; however, given that the size of beam envelope of ~180 × 100 µm² (H × V, with beam

focused at sample) is much smaller than the size of the FSM4 screen and the I diode sensitive area, a small adjustment of the position of these elements using the direction of the motorised translation might be sufficient.

Translation	
Actuation	Remotely controlled
Stroke	"out" to +5 mm from beampath
Positioning resolution	2 μm
Positioning accuracy	5 μm
Repeatability	5 μm
Speed	Full stroke in 5s, if possible

11.17 Detector cover

To protect the detector from any damage from eventual accidents during sample mounting/unmounting operations, it would be convenient to include a protection system for the detector screen. This could be a rolling curtain (as in SLS PXII) or blade that completely covers the screen (as in XALOC), or (less preferably) a plate placed somewhere between the detector and the sample position.

If convenient, this cover could also be used as support for the diagnostic set described in section 11.16.

This plate does not need motorised movements, other than its actuation.

Retractile motion	
Actuation	Remotely controlled
Speed	In/out in 5 s

11.18 Detector

As described in section 5.7, the detector has to be translated longitudinally along the beam path (y axis) and transversally (x axis). Longitudinal positioning will allow data collection at different resolutions, by moving the detector within the range of 70 mm to 250 mm from sample position. The beam axis should hit the detector at the same position irrespective of the detector longitudinal position. This requires the wobble to be less than the pixel size of the detector (typically 50 - 80 μm for current pixel-array detectors).

The detector will be mainly used with the beam axis lying close to the centre of the screen, with a ~5mm vertical offset. At the detector position, beam excursion upon changes in the beam energy will be in the range of 100 to 200 μm (corresponding to 70 mm and 250 mm from sample position, respectively). Given pixel dimensions of 50 - 80 μm, for instance, the beam excursion will change the beam centre position by 2-3 pixels at most, so no correction of the detector vertical position is required to compensate beam vertical excursion. Thus, no remotely controlled vertical translation is required for the detector. Manual adjustment of vertical position could however be convenient for (coarse) alignment.

To extend the high resolution limit of the recorded diffraction, the detector can be moved so that the centre of the sensitive area is not aligned with the beam and one side of the detector is exposed to higher Bragg angles. Given that with a vertical spindle configuration the blind zone will fall along the vertical axis, a movement along the transversal axis would be preferred to this end (and only required in one sense of the axis), provided this is compatible with the He containment and does not compromise the stability of the element. The proposed stroke of such transversal offset would be of 100 mm.

On top of this offset, there may also be some instances when it can be required to completely remove the detector from the beam path (for beam in-depth commissioning or to place other scientific or diagnostic instruments at the beampath, e.g. an eventual phase contrast tomography detector at ~300 mm crystal-to-detector distance [19], [20], see section 9.1). This could be achieved by extending the stroke of the transversal translation described above, to reach a stroke larger than half of the width of the detector screen. Given a detector width of 300 - 400 mm, a stroke of about 250 mm from the beampath would be needed to this purpose. In addition, and for the same reason, there should be ~100 mm of free space on the granite, downstream the detector box and cabling. This will require extending the granite further downstream than what would be strictly required just for the diffraction detector.

No rotation movement is required.

Transversal translation (x axis)	
Actuation	Remotely controlled
Stroke	-30 to +250 mm from beam axis
Positioning resolution	1 µm
Positioning accuracy	2 µm
Repeatability	2 µm
Speed	6 mm/s
Longitudinal translation (y axis)	
Actuation	Remotely controlled
Stroke	+70 to +250 mm from sample
Positioning resolution	Ideally 1 µm (if too slow, then 2 µm)
Positioning accuracy	2 µm
Repeatability	2 µm
Speed	20 mm/s
Vertical translation (z axis)	
Actuation	Manual adjust
Stroke	±10 mm from beam axis
Resolution	5 µm

11.19 Helium chamber

Encapsulating the area around the sample (from the vacuum window downwards, including the detector) a Helium chamber will be installed to contain the He gas atmosphere (at Helium

concentrations ≥98%). The chamber itself will not move, although it will need to allow the movements of the contained elements.

11.20 Cryostream

The cryostream does not need to be aligned with the beam, but the nozzle needs to be positioned close (~6 mm) to sample, in order to effectively maintain the cryogenic temperature. It also needs to be aligned orthogonally to the goniometer axis (that is, parallel to the ground plane), or close to that (<15º tilting), to minimise the induction of temperature gradients on the goniometer head stages that could impact on the sample positioning stability (as described in section 5.6).

Cryostream will also need to be positioned in a way that allows access of the automated sample changer to the sample holder, ideally without changing the distance of the cryostream tip to the sample. A larger movement might be required to allow for mounting of non-standard samples (retraction of the cryostream).

all translations (xyz axis)	
Actuation	Manually adjusted
Stroke	10 mm
Resolution	10 µm in any direction

11.21 Fluorescence detector

Similarly to the cryostat, the fluorescence detector does not need to be aligned with beam, but requires to be positioned close (~5-20 mm) to sample. In this case, though, the fluorescence detector will be positioned away from the sample environment when not in use (during standard beamline operation), and will be moved close to the sample when required.

This retracted position can be defined as far as required, provided that the detector can cover this distance in a relatively short time (~5 seconds).

The fluorescence detector should be preferably actuated through motors. However, in case that geometrical constrains lead to possible collisions in some operations, then the actuation should be pneumatically driven so that this can be controlled through EPS.

Translation	
Actuation	Remotely controlled
Stroke	“out” to 5 mm from sample
Positioning resolution	2 µm
Positioning accuracy	5 µm
Repeatability	5 µm
Speed	Full stroke in 5s, if possible

11.22 Sample Changer

The samples will be mounted onto the sample holder by an automated robotic arm carrying a specialised gripper, which will extract selected pre-mounted crystal samples from a LN_2-filled storage dewar and place them on the goniometer head; upon finalisation of data collection, the system also has to remove the sample and its mount and place it back in its allocated position in the storage dewar.

The automated sample mounting system (including the storage dewar(s)) will be installed on an independent table, separated from the other end-station elements. The gripper will need to be aligned with the sample holder (but not to the beam). The mounting/unmounting procedure will need to be made compatible with the presence of a helium chamber (i.e. by means of a valve).

The definition of mounting/unmounting positions for the robotic arm will be performed through the robot interface, so no additional motors are required to the support of this piece of equipment.

The use of a sample changer equipped with a double gripper, able to unmount a loaded sample and mount the following one in the same trip, thereby greatly reducing the mount/unmount cycle time, is preferred. However, this needs to be compatible with the helium chamber valve.

11.23 Summary of required stages

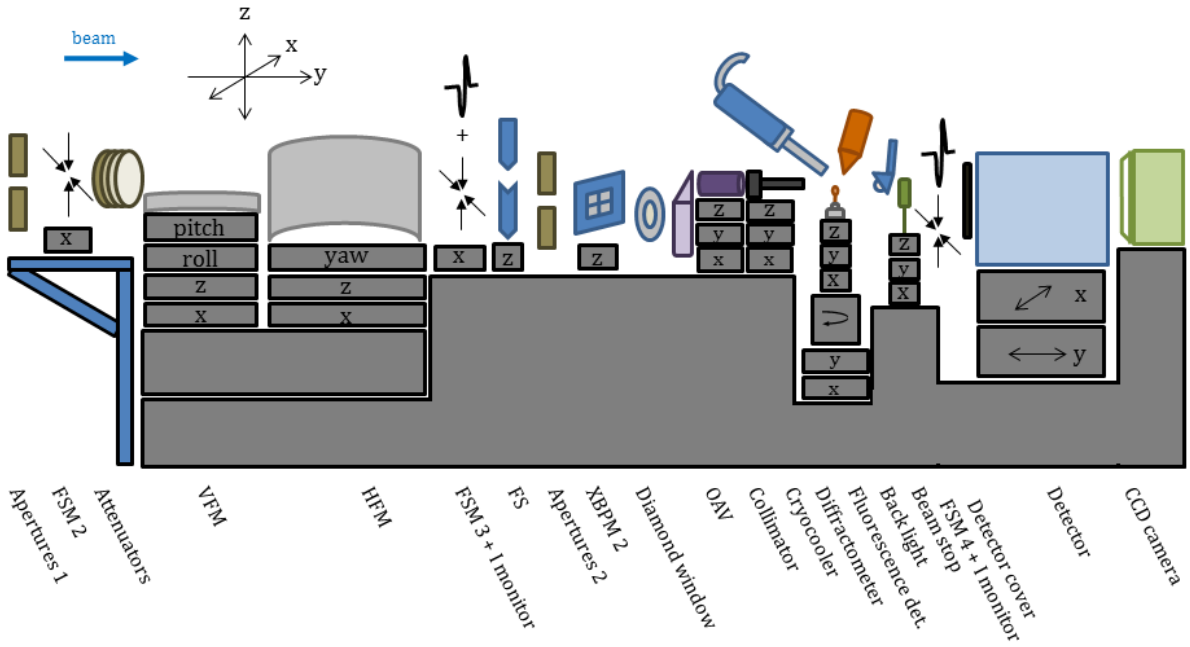

Figure 34. The ES elements from the KB onwards will be grouped on one single block, all installed on the same stage.

Apertures: 4 motors, to define *gap* and *offset*. No translation/rotation of the whole element.

FSM 2: motorised transversal translation.

Attenuators: manual alignment.

FSM 3 & I monitor 1: motorised vertical or transversal translation.

Fast shutter: motorised vertical translation.

XBPM 2: motorised vertical translation.

OAV: motorised vertical, longitudinal and transversal translations.

Collimator: motorised vertical, longitudinal and transversal translations.

Goniometer: omega motorised longitudinal and transversal translations; omega rotation; sample centring motorised vertical, longitudinal and transversal translations.

SSX stages: motorised vertical, longitudinal and transversal translations.

Backlight: motorised in/out actuation, motorised longitudinal translation.

Beamstop: motorised vertical, longitudinal and transversal translations, plus retraction.

FSM 4 + I monitor 2: motorised in/out actuation.

Detector: motorised longitudinal and transversal translation. **Cover:** motorised in/out.

Cryostream: manual adjustment.

Fluorescence detector: motorised in/out actuation.

12 Appendix III: Helium gas operational costs

The operational cost estimates have been calculated based on the following figures:

Cryostream consumption (@ 1 bar):	7 l/min
He-bearing leak rate (@ 1 bar):	1.89 l/min (5% of input + 7% loss factor)
Operation days/year:	250 days
50 l @ 200 bar bottle, to Euro:	116.11 €/bottle
He gas volume @ 200 bar to He @ 1 bar:	186 l (7% loss factor applied)
Expansion factor LHe to He gas:	757
Purchase cost of LHe: 11.23	11.23 €/l
Cost of the LHe production at ALBA:	1.8 €/l (in electricity)
Estimated He recovery efficiency at ALBA	93 %

	Cryostream	Goniometer	Total
Consumption (l/min)	7	1.9	8.9
Number of 50 l He gas bottles (@200 bar) /day	1.1	0.3	1.4
Evaporated LHe liters/day	13.3	3.6	16.9
Evaporated LHe liters/year	3328.9	900.0	4228.9
Assuming 100% chamber input is purchased			
Purchase cost in He gas bottles (k€/day)	0.13	0.03	0.16
Purchase cost in He gas bottles (k€/year)	31.5	8.5	**40.0**
Purchase cost in LHe (k€/year)	37.4	10.1	**47.5**
Assuming 100% chamber output is used for recovery			
Electricity costs for LHe recovery (k€/year)	6.0	1.6	**7.6**
7% leak in recovery (LHe liters/year)	233.0	63.0	296.0
Purchase cost in LHe (k€/year)	2.6	0.7	**3.3**
Purchase cost in He gas bottles (k€/year)	2.2	0.6	**2.8**
Assuming 70% chamber output is used for recovery			
Electricity costs for LHe recovery (k€/year)	4.2	1.1	**5.3**
7% leak in recovery (LHe liters/year)	163.1	44.1	207.2
Purchase cost in LHe (k€/year)	13.0	3.5	**16.5**
Purchase cost in He gas bottles (k€/year)	11.0	3.0	**14.0**

13 References

[1] D. Liebschner, Y. Yamada, N. Matsugaki, M. Senda, and T. Senda, "On the influence of crystal size and wavelength on native SAD phasing," *Acta Crystallogr. Sect. D Struct. Biol.*, vol. 72, no. 6, pp. 728–741, 2016.

[2] I. Martiel, H. M. Müller-Werkmeister, and A. E. Cohen, "Strategies for sample delivery for femtosecond crystallography," *Acta Crystallogr. Sect. D Struct. Biol.*, vol. 75, pp. 160–177, 2019.

[3] D. A. Sherrell *et al.*, "A modular and compact portable mini-endstation for high-precision, high-speed fixed target serial crystallography at FEL and synchrotron sources," *J. Synchrotron Radiat.*, vol. 22, no. 6, pp. 1372–1378, 2015.

[4] P. Roedig *et al.*, "A micro-patterned silicon chip as sample holder for macromolecular crystallography experiments with minimal background scattering," *Sci. Rep.*, vol. 5, no. May, pp. 1–11, 2015.

[5] C. O. Barnes *et al.*, "The crystal structure of dGTPase reveals the molecular basis of dGTP selectivity," *Proc. Natl. Acad. Sci. U. S. A.*, vol. 116, no. 19, pp. 9333–9339, 2019.

[6] N. Coquelle *et al.*, "Raster-scanning serial protein crystallography using micro- and nano-focused synchrotron beams," *Acta Crystallogr. Sect. D Biol. Crystallogr.*, vol. 71, pp. 1184–1196, 2015.

[7] C.-Y. Huang *et al.*, "*In meso in situ* serial X-ray crystallography of soluble and membrane proteins," *Acta Crystallogr. Sect. D Biol. Crystallogr.*, vol. 71, no. 6, pp. 1238–1256, 2015.

[8] A. E. Cohen *et al.*, "Goniometer-based femtosecond crystallography with X-ray free electron lasers," *Proc. Natl. Acad. Sci.*, vol. 111, no. 48, pp. 17122–17127, 2014.

[9] A. Y. Lyubimov *et al.*, "Capture and X-ray diffraction studies of protein microcrystals in a microfluidic trap array," *Acta Crystallogr. Sect. D Biol. Crystallogr.*, vol. 71, no. 4, pp. 928–940, 2015.

[10] T. D. Murray *et al.*, "A high-transparency, micro-patternable chip for X-ray diffraction analysis of microcrystals under native growth conditions," *Acta Crystallogr. Sect. D Biol. Crystallogr.*, vol. 71, pp. 1987–1997, 2015.

[11] Z. Ren *et al.*, "Crystal-on-crystal chips for: In situ serial diffraction at room temperature," *Lab Chip*, vol. 18, no. 15, pp. 2246–2256, 2018.

[12] C. Mueller *et al.*, "Fixed target matrix for femtosecond time-resolved and in situ serial micro-crystallography," *Struct. Dyn.*, vol. 2, no. 5, pp. 1–16, 2015.

[13] D. Lee *et al.*, "Nylon mesh-based sample holder for fixed-target serial femtosecond crystallography," *Sci. Rep.*, no. December 2018, pp. 1–9, 2019.

[14] G. K. Feld *et al.*, "Low-Z polymer sample supports for fixed-target serial femtosecond X-ray crystallography," *J. Appl. Crystallogr.*, vol. 48, no. December 2014, pp. 1072–1079, 2015.

[15] S. Oghbaey *et al.*, “Fixed target combined with spectral mapping: approaching 100% hit rates for serial crystallography,” *Acta Crystallogr. Sect. D Struct. Biol.*, vol. 72, no. 8, pp. 944–955, 2016.

[16] R. B. Doak *et al.*, “Crystallography on a chip - Without the chip: Sheet-on-sheet sandwich,” *Acta Crystallogr. Sect. D Struct. Biol.*, vol. 74, no. May, pp. 1000–1007, 2018.

[17] J. Lieske *et al.*, “On-chip crystallization for serial crystallography experiments and on-chip ligand-binding studies,” *IUCrJ*, vol. 6, pp. 714–728, 2019.

[18] R. De Wijn *et al.*, “A simple and versatile microfluidic device for efficient biomacromolecule crystallization and structural analysis by serial crystallography,” *IUCrJ*, vol. 6, pp. 454–464, 2019.

[19] S. Brockhauser, M. Di Michiel, J. E. McGeehan, A. A. McCarthy, and R. B. G. Ravelli, “X-ray tomographic reconstruction of macromolecular samples,” *J. Appl. Crystallogr.*, vol. 41, no. 6, pp. 1057–1066, 2008.

[20] M. Polikarpov, G. Bourenkov, A. Snigirev, and T. Schneider, “Phase-contrast X-ray Imaging and Microscopy for Crystallographic Applications at EMBL Beamline P14 of PETRA III,” *Microsc. Microanal.*, vol. 24, no. S2, pp. 384–385, 2018.

[21] M. Polikarpov *et al.*, “Visualization of protein crystals by high-energy phase-contrast X-ray imaging research papers,” pp. 947–958, 2019.

[22] J. M. Grimes *et al.*, “Where is crystallography going?,” *Acta Crystallogr. Sect. D Struct. Biol.*, vol. 74, no. 2, pp. 152–166, 2018.

[23] R. Glaeser *et al.*, “Characterization of conditions required for x-ray diffraction experiments with protein microcrystals,” *Biophys. J.*, vol. 78, no. 6, pp. 3178–3185, 2000.

[24] K. Hirata *et al.*, “Achievement of protein micro-crystallography at SPring-8 beamline BL32XU,” *J. Phys. Conf. Ser.*, vol. 425, no. PART 1, pp. 8–12, 2013.

[25] M. Hiraki, N. Matsugaki, Y. Yamada, and T. Senda, “Development of sample exchange robot PAM-HC for beamline BL-1A at the photon factory,” *AIP Conf. Proc.*, vol. 1741, 2016.

[26] G. Evans, D. Axford, and R. L. Owen, “The design of macromolecular crystallography diffraction experiments,” *Acta Crystallogr. Sect. D Biol. Crystallogr.*, vol. 67, no. 4, pp. 261–270, 2011.

[27] J. Trincao *et al.*, “VMXm: a new sub-micron beamline for macromolecular crystallography at Diamond Light Source,” *Acta Crystallogr. Sect. A Found. Adv.*, vol. 71, no. a1, pp. s191–s191, 2016.

[28] B. Pedrini, I. Martiel, E. Panepucci, and C. Pradervand, “SwissFEL ESB-MX instrument for fixed target protein crystallography at SwissFEL: Concept Design Report,” 2016.

[29] M. S. Miller *et al.*, “Getting the most out of your crystals: Data collection at the new high-flux, Microfocus MX beamlines at NSLS-II,” *Molecules*, 2019.

[30] A. Mozzanica *et al.*, “The JUNGFRAU Detector for Applications at Synchrotron Light

Sources and XFELs," *Synchrotron Radiat. News*, vol. 31, no. 6, pp. 16–20, 2018.

[31] S. Redford *et al.*, "Operation and performance of the JUNGFRAU photon detector during first FEL and synchrotron experiments," *J. Instrum.*, vol. 13, no. 11, 2018.

[32] F. Leonarski *et al.*, "Fast and accurate data collection for macromolecular crystallography using the JUNGFRAU detector," *Nat. Methods*, vol. 15, no. 10, pp. 799–804, 2018.

[33] A. Tolstikova *et al.*, "1 kHz fixed-target serial crystallography using a multilayer monochromator and an integrating pixel detector," *IUCrJ*, vol. 6, no. 5, pp. 1–11, 2019.

[34] A. Allahgholi *et al.*, "AGIPD, a high dynamic range fast detector for the European XFEL," *J. Inst.*, vol. 10, no. 01, pp. C01023–C01023, 2015.

[35] A. Casanas *et al.*, "EIGER detector: Application in macromolecular crystallography:," *Acta Crystallogr. Sect. D Struct. Biol.*, vol. 72, no. 9, pp. 1036–1048, 2016.

[36] M. Levantino, B. A. Yorke, D. C. F. Monteiro, M. Cammarata, and A. R. Pearson, "Using synchrotrons and XFELs for time-resolved X-ray crystallography and solution scattering experiments on biomolecules," *Curr. Opin. Struct. Biol.*, vol. 35, pp. 41–48, 2015.

[37] A. Meents *et al.*, "Pink-beam serial crystallography," *Nat. Commun.*, vol. 8, no. 1, 2017.

[38] E. C. Schulz *et al.*, "The hit-and-return system enables efficient time-resolved serial synchrotron crystallography," *Nat. Methods*, vol. 15, no. 11, pp. 901–904, 2018.

[39] P. Mehrabi *et al.*, "Liquid application method for time-resolved analyses by serial synchrotron crystallography," *Nat. Methods*, vol. 16, no. 10, pp. 979–982, 2019.

[40] I. I. Mathews *et al.*, "The Conformational Flexibility of the Acyltransferase from the Disorazole Polyketide Synthase Is Revealed by an X-ray Free-Electron Laser Using a Roomerature Sample Delivery Method for Serial Crystallography," *Biochemistry*, vol. 56, no. 36, pp. 4751–4756, 2017.

[41] C. G. Roessler *et al.*, "Acoustic Injectors for Drop-On-Demand Serial Femtosecond Crystallography," *Structure*, vol. 24, no. 4, pp. 631–640, 2016.

[42] F. D. Fuller *et al.*, "Drop-on-demand sample delivery for studying biocatalysts in action at X-ray free-electron lasers," *Nat. Methods*, vol. 14, no. 4, pp. 443–449, Apr. 2017.

[43] S. Tsujino, A. Shinoda, and T. Tomizaki, "On-demand droplet loading of ultrasonic acoustic levitator and its application for protein crystallography experiments," *Appl. Phys. Lett.*, vol. 114, no. 21, 2019.

[44] K. S. Shanks, "Development of Low-Noise Direct-Conversion X-Ray Area Detectors for Protein Microcrystallography," Cornell University, 2014.

[45] S. Basu *et al.*, "Long-wavelength native-SAD phasing: opportunities and challenges," *IUCrJ*, vol. 6, no. 3, pp. 1–14, 2019.